DEVELOPMENT OF A SONIC SENSOR FOR AIRCRAFT APPLICATIONS

A Dissertation
Presented to
The Academic Faculty

By

Jonathan D. Carroll

In Partial Fulfillment
of the Requirements for the Degree
Doctor of Philosophy in the
School of Aerospace Engineering

Georgia Institute of Technology

December 2021

DEVELOPMENT OF A SONIC SENSOR FOR AIRCRAFT APPLICATIONS

Approved by:

Dr. Krish Ahuja, Advisor
School of Aerospace Engineering
Georgia Institute of Technology

Dr. Lakshmi Sankar, Co-Advisor
School of Aerospace Engineering
Georgia Institute of Technology

Dr. Jechiel Jagoda
School of Aerospace Engineering
Georgia Institute of Technology

Dr. Karim Sabra
School of Mechanical Engineering
Georgia Institute of Technology

Dr. Woodrow Whitlow, Jr.
Special Liaison to Technical Director
National Aerospace Solution LLC

Mr. Randy Lang
Engineering Product Lead
Aerosonic Corporation

Date Approved: December 1, 2021

Sound is pushed by air

How fast will it travel there?

Only time will tell

To the best wife and partner I could have ever imagined, Reilly.

ACKNOWLEDGEMENTS

The author would like to express extreme gratitude to Dr. Krish Ahuja for his patience and guidance throughout this whole process. The author would also like to thank the members of his commitee, Dr. Lakshmi Sankar, Dr. Jechiel Jagoda, Dr. Kabrim Sabra, Dr. Woodrow Whitlow, and Mr. Randy Lang for their support in pursuit of this endeavor.

This work was funded by Aerosonic Corporation under its Aerosonic Fellowship program. The author is grateful to Aerosonic not just for their financial support, but also continued guidance throughout the course of this effort.

Many thanks to the engineers at Georgia Tech Research Institute, Dr. Robert Funk, Darryl Dickey, Dr. Aharon Karon, and Dr. Nick Breen for their support and help troubleshooting facilities. A special thanks to Julia Filloon who assisted in acquiring data used in this work.

Finally, the author would like to thank his family for their continued support and encouragement. The author would especially like to thank his amazing wife, Reilly, who continually encourages me to be the best version of myself.

TABLE OF CONTENTS

LIST OF TABLES

LIST OF FIGURES

LIST OF SYMBOLS

Latin Symbols

$\mathbf{r}$	Vector Distance between Transducer and Point
A	Signal Amplitude
a	Aperture Diameter
c	Speed of Sound
d	Distance
e	Vapor Pressure
f	Frequency
J_1	Bessel Function of the First Kind
k	Wave Number
L	Length or Distance
M	Mach Number
p	Static Pressure
P_0	Reference Acoustic Pressure
P_{Noise}	Noise Acoustic Pressure
P_{Signal}	Signal Acoustic Pressure

q_c	Free-stream Dynamic Pressure
R	Specific Gas Constant
R_{xx}	Auto-correlation Parameter
R_{xy}	Cross-correlation Parameter
T	Static Temperature
t	Time
U	Flow Velocity
V	Signal Velocity

Greek Symbols

α	Angle of Attack
γ	Ratio of Specific Heats
μ	Mach Angle
μ_α	Mean Value of Calculated Angle of Attack
μ_c	Mean Value of Calculated Speed of Sound
μ_U	Mean Value of Calculated Velocity
μ_{T_s}	Mean Value of Calculated Static Temperature
ω	Angular Spacing to Receiver 3
ϕ	Angular Spacing to Receiver 2
ϕ_i	Signal Phase for ith Transducer
ρ	Density

σ_α	Standard Deviation of Calculated Angle of Attack
σ_c	Standard Deviation of Calculated Speed of Sound
σ_U	Standard Deviation of Calculated Velocity
σ_{T_s}	Standard Deviation of Calculated Static Temperature
τ	Time Delay
θ	Angular Spacing to Receiver 4
θ_B	Wave Front Angle of Phased Array
θ_r	Angle between normal of transducer plane and desired point

Subscripts

∞	Freestream Parameter
t	Total Property of Air
TS	Test Section Parameter
1	Parameter from R_1 to R_2
2	Parameter from R_1 to R_3
3	Parameter from R_1 to R_4

Acronyms

ADS	Air Data System
AoA	Angle of Attack
AUSAT	Airborne Ultrasonic Anemometer Thermometer
CFD	Computational Fluid Dynamics

DAq	Data Acquisition System
GTRI	Georgia Tech Research Institute
LWC	Liquid Water Content
MTF	Model Test Facility
RH	Relative Humidity
SNR	Signal-to-Noise Ratio
SPL	Sound Pressure Level
TAT	Total Air Temperature
UA	Ultrasonic Anemometer

SUMMARY

Modern aircraft are equipped with a plethora of sensors to measure aircraft speed, air pressure, angle of attack, and total air temperature, the main flow properties of interest in a typical air data system. The industry method of measuring these flow properties requires multiple sensors per flow property for redundancy considerations. The methods for measuring the flow properties have advanced over the years, but the main methodology has been relatively the same since the inception of flight. It involves use of a collection of probes. The total air temperature is measured by thermocouples, total air pressure is measured by a Pitot probe, and static air pressure is measured by a flush opening of a tube or opening on the aircraft surface connected to a pressure sensor. The static pressure port is a flush-mounted air inlet opening in the side of the fuselage. It is situated in an area with relatively undisturbed airflow. For more accurate readings, some aircraft have two external static pressure ports - one mounted on each side of the fuselage. Likewise, angle of attack is measured by a collection of pressure measuring ports, primarily by using the pressure difference between two orifices. The magnitude of the pressure difference depends on the shape of the nose of the tube and the angular position of the orifices. It is worth mentioning that a Pitot-static probe measures total and static pressures and can be used to compute flow velocity. The Pitot-static probe is most commonly used in applications where only an air speed measurement is desired and is technology that was developed in 1732.

Synergy is the hallmark of the aviation field. Technology that can perform multiple functions have an easier time buying their way onto aircraft. This work examines a different way of combining the measurement of aircraft speed, angle of attack, and air temperature into one synergistic sensor, namely using acoustic propagation through air to determine the flow properties. Sonic anemometry has been around since

the 1950s, but has largely been restricted to ground based (meteorological) and/or low-speed applications (unmanned aerial vehicles, general aviation aircraft, helicopter applications). This technology has not seen practical applications to higher speed flows mainly due to signal-to-noise ratios at the higher speeds. This work aims to lay the ground work to increasing the signal-to-noise ratios and apply sonic anemometry to measure the flow properties at higher subsonic speeds utilizing cross-correlation and a phased array.

CHAPTER 1
INTRODUCTION

The field of aeroacoustics has been an area of constant research over the past six decades. Acoustic waves have some special characteristics that allow for heating, cooling, and even active flow control over airfoil shapes through the use of synthetic jets and other methods. They can also be used to measure properties of the flow over an aircraft, including the free-stream pressure ratio, density ratio, and total temperature. The current measurement techniques to obtain these parameters applied to aircraft require a specific probe. It is desired to apply knowledge of acoustics to develop an aircraft sensor that can measure multiple flow properties with minimal impact to the flow field.

Sonic anemometry, which utilizes acoustic propagation to determine the flow speed, has been around since the 1950s, but has largely been restricted to ground based, low speed applications. Sonic anemometry is an attractive option because of the following:

- There can be minimal flow disturbance
- No moving parts
- No need to calibrate the system as with pressure-based systems

There have been some attempts to increase the integration of sonic anemometry into the aircraft industry, with little success. The current systems are large and heavy, have a significant drag penalty, or are limited in operation to low-speed flows. There have been acoustic air data systems which attempted to use flush mounted receivers, but the accuracy of the air data system was reduced due to flow features which will be discussed in later sections. Adding a sensor that can read total temperature, static temperature, airspeed, and angle of attack will have the added benefit of reducing the number of sensors sticking into the flow, and may result in a reduction in failure mode analysis due to the minimization of the number of sensors on the aircraft.

This work explores the applicability of sonic anemometry to aircraft for high subsonic and sonic speeds. This effort identifies the underlying issues associated with applying sonic anemometry to high-speed flows and provides methods to overcome them. In particular, this work investigates the use of phased array technology to increase the accuracy and applicability at the higher speeds and smaller footprints (lighter and fewer systems). The motivation for this work is given in the next section.

1.1 Motivation

In 1732, Henri Pitot needed a device to measure the flow velocity in a river and developed a simple device to measure the changes in pressure[1], and therefore the water velocity. This is the same device that bears his name and has been instrumental in measuring the speed of aircraft, boats, and/or the flow velocity of liquids and gases for the past few centuries. The simplicity of the Pitot and Pitot-static tube is part of the reason that this method of measuring flow velocity has been the industry standard for wind velocity. The pitot tube is not without issues. Ice ingestion and ice accretion such that the pressure ports become clogged and cause erroneous readings in the cockpit has long plagued the operation of the Pitot probe. A fact which came to the attention of the whole world on June 1, 2009, when Air France Flight 447 fell from the sky from 35,000 ft and crashed into the ocean, killing all 228 people on board. The subsequent crash investigation into this tragic event pointed to a failure in the Pitot-static system as the initial event that triggered the subsequent actions resulting in the loss of the aircraft[2]. The Pitot-tubes were thought to have been iced over due to the atmospheric conditions at which the aircraft was flying. While other more advanced methods of measuring flow speed have been developed, they have mostly been restricted to ground operations (i.e., flow through pipes or in wind tunnels), aircraft applications of this new technology has been limited. As technology advances, the flow speed measurement options that were previously unavailable become viable solutions for aircraft measurement applications. Sonic anemometry is one such solution.

The utilization of acoustic propagation through air may provide some unique features to measure the flow field parameters that are less intrusive and offer an alternative method for measuring the flow velocity. For stationary air, an acoustic wave travels at a relatively constant velocity, assuming the temperature is uniform. The addition of an incident flow velocity can be incorporated into the propagation velocity by simple vector addition, simply put, the acoustic wave is "pushed" by the motion of the air molecules. It is desired to leverage this property of acoustic propagation to develop a method for measuring the flow speed and direction for aircraft applications that is less prone to icing issues, and may offer some additional benefits to the air data system of the aircraft, such as the direct measurement of the Mach number of aircraft, external total and static temperature, total to static pressure ratio, and total to static density ratio.

Including the measurement for the static pressure, the total pressure, and density (both static and total) can be determined through isentropic relationships of air. The pressures, densities and temperatures are instrumental to the operation of the engines, and could provide some increases in the operational efficiency of the engines which would lead to fuel savings and reduced operational costs. Incorporation of speed, angle of attack, and temperature into one sensor unit may also reduce the development costs by reducing the number of failure modes to be tested. The sensor is either working or not, there are no failure modes where the effect of a failed angle-of-attack sensor with a working speed sensor and temperature sensor, or any other combination of working and failed sensors. The scope of this work is given in the following sections.

1.2 Objective

This work lays the ground work for the applicability of a speed sensor for aircraft applications and higher speed flows (high subsonic and above) by developing and testing a methodology to apply sonic means of measuring flow properties at high speeds. As will be discussed in the next chapter, sonic anemometry, or utilizing acoustic propagation to determine the flow velocity, has been used since the 1950s. Although, since its inception, it has been largely confined to ground-based operations. The objective of this work is to:

1. Present validation data and technical approach for a realistic application of sonic measurement of flow properties on low-speed aircraft.

2. Extend sonic methodology to higher speed applications through application of phased array technology

1.3 Contributions to the State-of-the-Art

This work furthers the state-of-the-art in a number of ways.

1. This work derives and verifies a methodology to calculate the flow speed, angle of attack, and air temperature for aircraft applications. There have been many methodologies for sonic anemometry, but this configuration considers the sound source upstream of the receivers, and in a small package so as not to cause more drag and increased weight that the currently commercially available systems suffer from. The methodology has been successfully flight tested by Georgia Tech Research Institute (GTRI) and is currently being considered by Aerosonic for integration into a production prototype package.

2. It is the first application of phased arrays to the ultrasonic anemometer problem. It holds potential for application of the methodology developed here to high

flow speeds where a single speaker/source may not provide the necessary Signal-to-Noise Ratio (SNR). The application of acoustic phased arrays allows for both an increase in Sound Pressure Level (SPL) as well as the capability to direct the sound beam within a certain angular sweep. The beam can then be adjusted in such a way as to direct the point of strongest SPL to the receivers. Although still additional work is needed, this is the first time this technology has been tested for determining the speed of the free-stream air as well as other flow parameters and is a building block for extending the current work to high flow speeds, including supersonic and hypersonic flows.

3. This work shows the required SNR to achieve consistent cross-correlation down to a 0.05 second sampling time to integrate into flight data systems. One of the main drawbacks of cross-correlation is the sample time required to achieve a discernible peak in the cross-correlation. Many systems use times on the order of one second to accurately determine the time delay from cross-correlation. This work shows that sample times on the order of 0.05 seconds are achievable if the SNR if high enough for the cross-correlation to pick out the signal from the uncorrelated noise.

1.4 Thesis Outline

This work is divided into six chapters. The next chapter (Chapter two) examines the historical development of sonic sensors and discusses any applications to aircraft that have been introduced. Chapter three outlines the methodology and theory behind the proposed sonic sensor. Cross-correlation methodologies are used in Chapter four to determine the time of arrival of the source for various signal shapes in a validation of the sensor concept and layout for low speed. In Chapter five, the utilization of the phased array is discussed to extend the sonic sensor to higher speed flows. This is followed by the conclusions and recommendations for future work in Chapter six. For the interested reader, an uncertainty analysis is included in the Appendix.

CHAPTER 2
PREVIOUS RESEARCH AND UNDERSTANDING

2.1 Introduction

Compared to the use of a pitot-tube on an aircraft, sonic anemometry is on the cutting edge of technology, but meteorologists have been using ultrasonic anemometers to determine the flow speed, direction, and turbulence intensity since the 1950s. This technology has been limited to the wind energy and meteorologist fields due to the computing power required to measure the flow properties using acoustic signals. Even though these fields have seen the most application of ultrasonic anemometers, their use has been largely limited due to the high cost of these sensors. With the increase in computing power and reduction of microchip costs and size, there has been an increase in the use of ultrasonic anemometers. Most meteorologists and wind energy engineers still use cup or vane anemometers due to their comparatively low cost. Mechanical and civil engineering disciplines have also used ultrasonic acoustic signals to measure the flow through a pipe or channel [3]. A brief overview of the current state-of-the-art of aircraft sensors to measure the speed, angle of attack, and temperature is given in the next section to familiarize the reader with the current technology on aircraft. This is then followed by a more detailed review of the sonic anemometry in subsequent sections.

2.2 Aircraft Sensors

The majority of modern aircraft require some sort of external sensing to measure important flight parameters, such as speed, angle of attack, and air temperature. Aircraft sensors that measure these parameters are integral to the safe operation of aircraft. One of the most important is the aircraft speed sensor for which the applied measurement techniques are discussed in the next section. This is then followed by a description of the current measurement techniques for the angle of attack and total air temperature. The current work combines these flow property measurements into a single unit allowing for fewer external measurement connections on the aircraft and fewer failure modes to test, which could lead to a weight and cost savings for the aircraft.

2.2.1 Airspeed Sensors

One of the most important parameters the air data system can provide to the pilot is the aircraft speed. The most common air speed sensor is a mechanical based sensor which reads in the total pressure or impact pressure of the air. This is also known as a Pitot tube. As stated earlier, Henri Pitot developed the Pitot tube as a means to measure the speed of the water in rivers and canals and used this system for the first time in 1732 [1]. Sometimes, the Pitot tube is coupled with a static pressure port creating a Pitot-static tube. Using Bernoulli's equation for incompressible flow, the airspeed is then determined by:

$$V = \sqrt{\frac{2\left(p_t - p_s\right)}{\rho}} \tag{2.1}$$

As the speed is increased, the air becomes compressible and the above relationship does not hold. This requires the use of Bernoulli's equation for compressible flow, Equation 2.2, and specially compensated probe designs to determine the flight speed.

$$\frac{V^2}{2} + \left(\frac{\gamma}{\gamma - 1}\right)\frac{p}{\rho} = \left(\frac{\gamma}{\gamma - 1}\right)\frac{p_t}{\rho_t} \tag{2.2}$$

The pitot tube does have its limits when it comes to measuring flight speed. Due to the nature of the total pressure, the pressure sensor has to be able to read relatively high pressures, which reduces the lowest sensitivity that the pressure sensor can measure. Typically, the pressure sensor will read the pressure to within 0.5% of the maximum operating pressure that the sensor can handle. This limitation increases the lowest speed that can be accurately read by the air speed sensor.

In 1983 researchers at Old Dominion University attempted to develop a true airspeed sensor as a replacement for the conventional pitot-static probe. Goglia et al. [4] used the concept of vortex precession or the "vortex whistle." The probe analyzes the frequency response of the vortex whistle to determine the velocity of the flow around the sensor. The frequency response of the probe was found to be linearly proportional to the airspeed. This type of flow measurement device has found limited application on aircraft.

The sonic sensor, described in detail later, offers many advantages over the Pitot probe. First, the sonic sensor has less of an issue with low-speed flight. In fact, for some low-speed applications, the sonic sensor can even allow for the measurement of negative speeds (i.e. going backwards). This is particularly useful in rotorcraft applications. Sonic sensor can be placed on the belly of the fuselage and out of the rotor downwash to measure the flight speed in any direction. The same can not be said for the Pitot probe. Second, the sonic sensor does not have to go through a rigorous calibration. The sonic sensor is based on the geometry of the receivers, therefore the most calibration that might be required is the distance from the source to the acoustic center of the receiver. This can be done under static conditions and does not require the use of an expensive wind tunnel.

2.2.2 Total Air Temperature Sensors

As the aircraft industry moves to more efficient aircraft, a burden is placed on the engine manufacturers to develop more efficient engines. Adjusting engine parameters such that the engine is operating optimally at the highest efficiency for the current flight condition is important. Most of the modern engines are equipped with a Full Authority Digital Engine Control (FADEC) system to control the operation of the engine. This requires knowledge of the properties of the air that is entering the engine, specifically the air temperature and pressure entering the engine nacelle. The current work focuses on the measurement of total temperature, which is essential not only to engine controls, but flight speed, fire control, and bombing calculations [5]. The dependence of engine performance on air temperature can be seen by the early development of a total air temperature sensor by Franz [6] to measure the pressures and temperatures in superchargers to increase performance of the engine. Franz's design incorporated a small diffuser section before the thermocouple in an attempt to decelerate the air adiabatically. It was later shown that the deceleration of the flow was not necessary, which led to smaller and simplified designs for the total air temperature. Most of the total air temperature probes in use today are designs derivatives of designs from 50 years ago. Total air temperature sensors still in use today are shown in Figure 2.1. These temperature sensors feature a duct in which to decelerate the flow adiabatically to accurately measure the total temperature. The boundary layer will impact the total temperature measurement, therefore the duct with the thermocouple in it must be extended outside the boundary layer. The figure shows multiple embodiments of the Total Air Temperature (TAT) sensors.

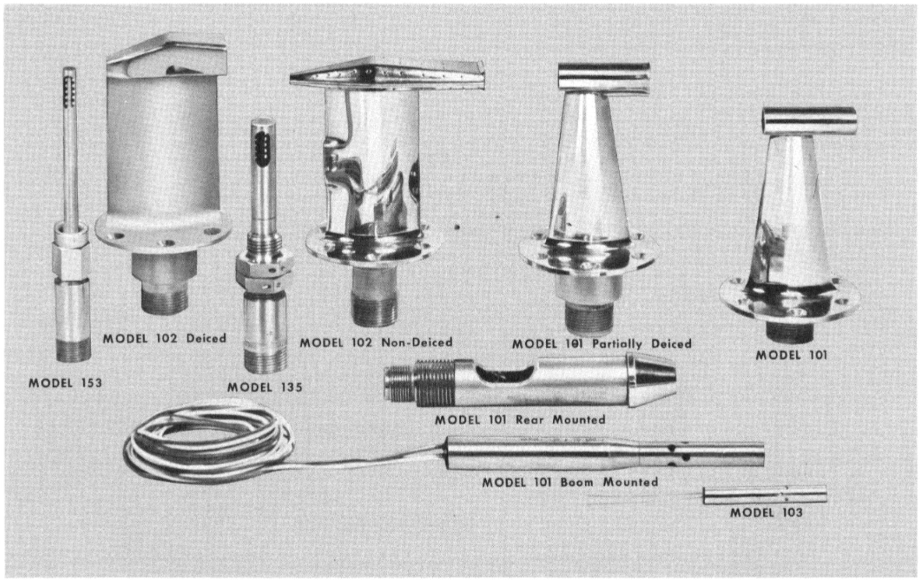

Figure 2.1: Total air temperature sensors[5]

These total temperature probes use a thin sensing element, typically platinum, shielded in a casing of various materials, as shown in Figure 2.2. Thin platinum elements are used because of the resistance properties of the material vary as the temperature changes. Platinum sensing elements can be more accurate than thermocouples, thermometers, etc. and can be used in extreme temperatures (-250 to +600 deg C). When using some sort of sensing material, platinum for most accurate TAT probes, there is a slight time delay due to the time it takes thermal equilibrium to be achieved for the probe and the air.

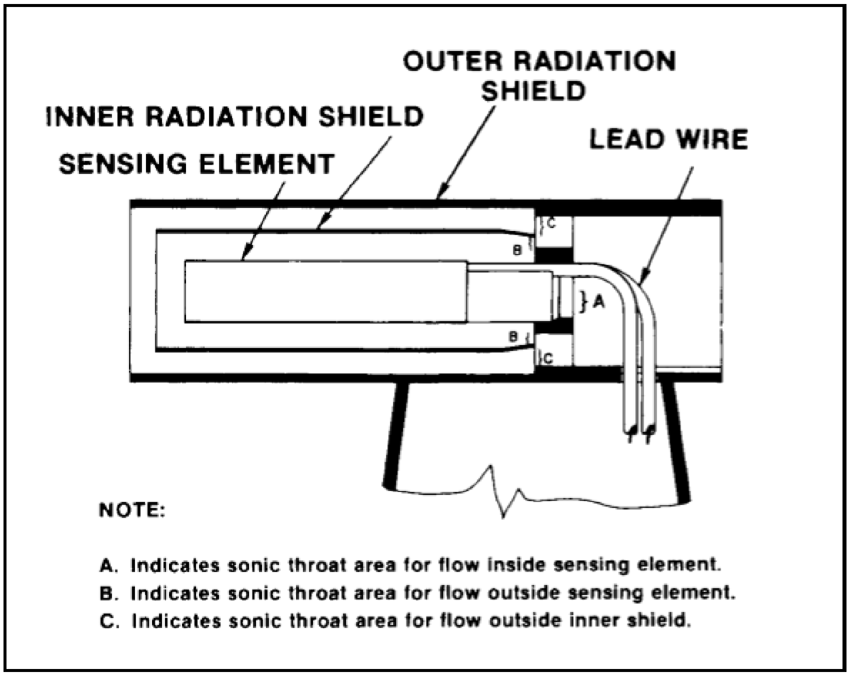

Figure 2.2: Total air temperature probe components[7]

These sensors are subject to a variety of correction factors and errors given in [5]. One item missing from the list in [5] is the variation between two TAT sensors on one aircraft. For example, the TAT at the forward part of the aircraft may read a different value than the TAT sensor at the engine nacelle. In this case, it is difficult to determine the correct TAT, and the engine may not be operating in the optimal settings for that operating condition. The differences could be caused by degradation of the TAT sensing element, incorrect calibration, etc. The actual TAT is then determined using an exact TAT probe. This probe is similar in operation to the typical TATs on the aircraft, but it is much more accurate. The accuracy does not come without a cost, the sensing element deteriorates quickly when in use and must be replaced often, which will put temperature validation at a severe disadvantage should the supply chain be strained or even cut off altogether. Utilizing acoustic characteristics in air, the following benefits can be achieved when measuring TAT over traditional means of total temperature measurement:

- No calibration necessary
- No time required to reach thermal equilibrium

2.2.3 Angle of Attack Sensors

From preliminary and conceptual design stages in aircraft development to the production and operation, the aircraft angle of attack is an important parameter. The angle of attack is defined as the angle between the relative wind vector and the aircraft reference line. This is typically the fuselage longitudinal axis. The angle of attack is paramount when comparing the aircraft performance to wind tunnel test data as well as informing the pilot when the aircraft is close to stalling. Fire suppression control and auto-pilot systems also incorporate the angle of attack measurements. The angle of attack, α, is typically defined as the angle between the aircraft body axis and the aircraft stability axis as shown in Figure 2.3.

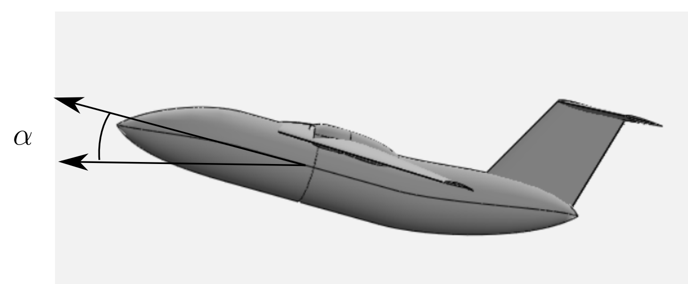

Figure 2.3: Aircraft angle of attack

In the early days of aviation, the pilots did not consider the aircraft angle of attack important enough to be displayed in the cockpit. It was not until 1958 that Svimonoff developed the Advanced Flight Instrument Panel that incorporated a displayed angle of attack for the United States Air Force (USAF) [8]. After initial tests, the pilots thought the angle of attack was only useful in certain flight phases such as final approach and take-off. The initial angle of attack sensors were also heavily influenced by turbulence, which caused a source of uncertainty and error. Once the angle of attack sensors were more independent of external flow conditions, pilots found them more useful and began to incorporate the data during the flight. The incorporation of the angle of attack helped increase the efficiency in which aircraft could take-off and climb out, and increased the fuel efficiency of the flight. By 1963, the advantages of displaying the aircraft angle of attack became apparent and were beginning to be incorporated into the airframe design.

There are a few common types of angle of attack sensors; vane, differential-pressure tube, and null seeking pressure sensor. Vane type sensors are similar to weather vanes, which rotate to align with the direction of the air flow. The angle of attack vane sensors are mass balanced to allow for easy rotation and align the vane with the flow. The amount of rotation then defines the angle of attack of the aircraft. Vane angle of attack sensors can be mounted on the aircraft surface or on booms extending out in front of the aircraft. A vane type angle of attack sensor is shown on the left side of Figure 2.4, while a version of a null seeking angle of attack sensor is shown on the right side.

Figure 2.4: Aerosonic vane angle of attack sensor (left) and null seeking angle of attack sensor (right) [9]

The differential-pressure tube sensor works by detecting a difference in pressure ports on the probe when at an angle of attack. The pressure ports are positioned at equal angular spacing from the longitudinal axis of the probe. The change in the pressure at the orifices is determined by the nose shape of the probe and the orifice positions. An example of a differential pressure angle of attack sensor is given in Figure 2.5. This sensor uses the pressure differential on the forward port and the port on the 45 degree surface to determine the angle of attack.

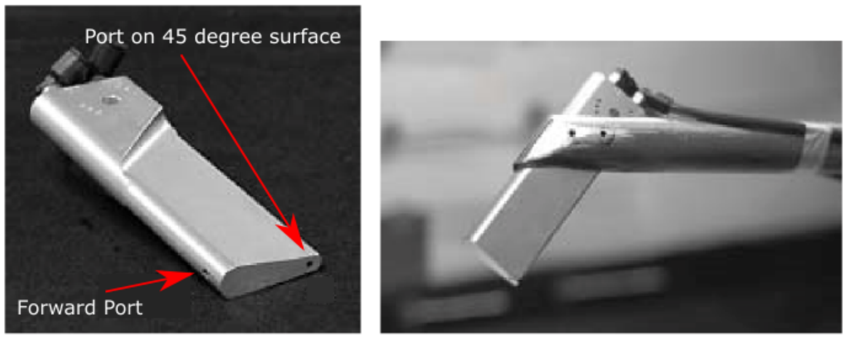

Figure 2.5: Differential pressure angle of attack sensor [10]

Null seeking sensors work similarly to the differential-pressure sensor, except the probe is allowed to rotate such that the pressure read at the two orifices is exactly the same. The angle at which the probe is rotated is then the angle of attack and read off of a potentiometer or mechanically linked to gauges on the instrument panel in the cockpit. This sensor can be more sensitive since it uses a differential pressure sensor which should always be close to zero. This probe is also independent of Mach and Reynolds number. Figure 2.6 shows a null seeking pressure sensor and its components as presented by Gracey [11].

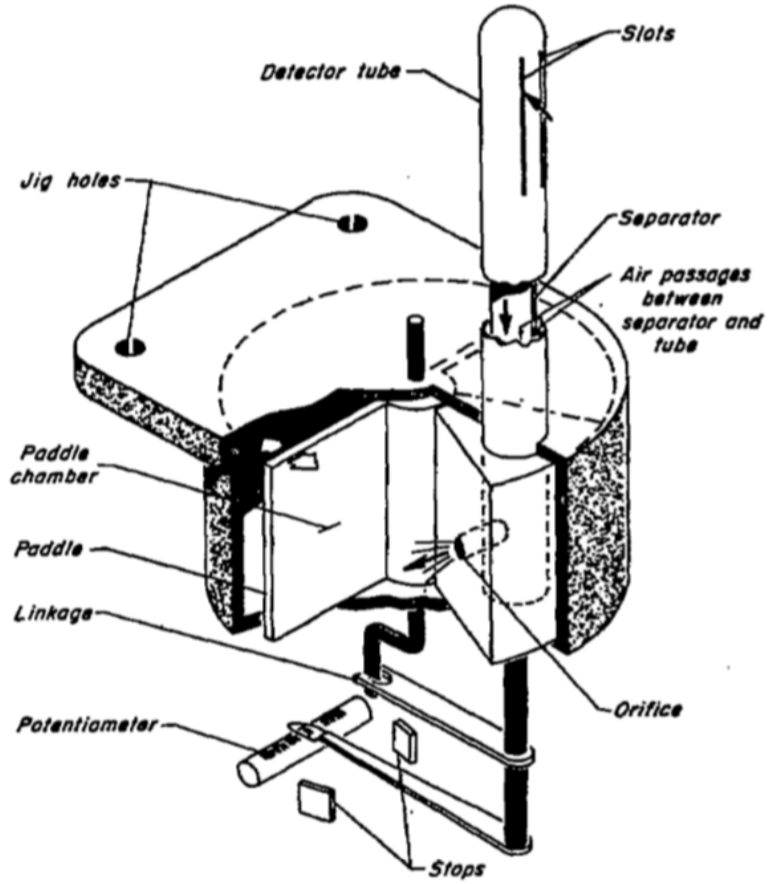

Figure 2.6: Null seeking pressure sensor [11]

All of these sensors have errors associated with them. They all measure local angle of attack, which could be influenced by the aircraft shape. This type of error is also called position error. For the vane-type sensors, there is a slip angle associated with the manufacturing tolerances of the sensor as well as position errors. If the vane sensor is mounted on a boom, the deflection of the boom will also impact the measured angle of attack. These sensors require some sort of calibration as well. It should be noted that any sensor attached to the aircraft will have these errors as well. This is just due to the nature of the flow about the aircraft. The total air temperature measurement techniques are outlined in the next section.

2.2.4 Recent Aircraft Sensor Developments

Flush air data systems are receiving interest as the current systems are limited by angle of attack and have an impact on the radar cross section of the flight vehicle. For example, a new flush air data system (FADS) as described in [12], is meant to replace the nose of the aircraft and measure the angle of attack, angle of sideslip, static pressure, and total pressure from this sensor. Figure 2.7 shows the FADS demonstrator concept [12] installed on the nose of the test article. Twelve static pressure ports are distributed over the probe surface. It is unclear the position of the ports as [12] does not show the position of the static ports. Since this is a pressure based system, it requires extensive calibration to ensure accurate measurement of flow properties.

Figure 2.7: Flush air data system test article [12]

This concept may have icing issues since it is pressure based and on the nose of the aircraft. A layer of ice could form on the nose and cause an error in the calculated angle of attack or sideslip due to the impact of the ice on the flow field and/or blockage of any of the pressure ports. Icing effects were not mentioned by Jost[12] and therefore may cause issues during flight operations. The FADS was able to measure the angle of sideslip (AoS) and angle of attack (AoA) to within one degree, the velocity to within five knots and the static pressure to within three mbar when compared to the conventional air data sensors. Also, system redundancy may cause applications issues with this concept. Typically the aircraft has a single nose, which means the system has one location where it can be installed. Damage to the nose of the aircraft or a glancing blow could cause the damage to the pressure transducers/strain gauges, which could lead to inaccurate readings from the system. Also, most radar systems for aircraft are near the nose, so careful considerations must be placed on material specifications and/or size restrictions should this concept be installed on the nose of aircraft to maintain adequate radar coverage.

Lie [13] attempted to develop an air data system without the use of a pitot-static probe. Lie proposed using the Inertial Measurement Unit (IMU) and GPS data along with aircraft dynamics to estimate the airspeed, angle of attack and angle of sideslip. Lie referred to this type of solution as a "synthetic air data system" since there is no direct measurement of the flow properties. Air speed, angle of attack, and angle of sideslip are all measured with the on-board IMU. This method was applied to data from UAV flight test to verify the accuracy. Overall, the synthetic air data system corresponds well with the data obtained from conventional methods of measurement. It should be noted that the synthetic air data system seemed to only work well under relatively steady conditions. For large variations of AoA and/or AoS, no data was presented for the synthetic ADS so it is unclear how well this methodology matches under dynamic events.

A relatively new concept is using optics to determine the aircraft speed and angle of attack and sideslip angle. These systems project laser energy into the air mass forward of the aircraft and use the back-scattered energy to determine the phase change of the light waves using Rayleigh scattering. At the time of this writing, the optical system is very heavy (∼250 lbs.) and limits the application on aircraft, but it is expected to reduce in weight to about 25 lbs when in production [14]. These optics-based systems are typically mounted in the nose of the aircraft, but could potentially be in the wing if necessary. These system have shown good agreement with the conventional air data systems in low-speed and supersonic flight regimes. Some of these systems can also measure the temperature through the shape of the scattering line [15].

As with the above described flush mounted sensors, icing may present issues for this sensor. The refraction of light through the ice may cause a deviation in the spectrum that is scattered back to the sensor, which could cause errors in the read flow parameters. Also, system redundancies and weight could be an issue. Typically aircraft are required to have redundant systems in the event that one should fail, the aircraft can fly safely. At 25 lbs, per installation, the entire air data system could end up being around 100 lbs for just the sensors. There is also the issue of enough particle seeding the target volume so a sufficient back-scattering can be measured. Some researchers are tackling this problem with other methods of analysis.

It is clear from the previous sections that there are still some improvements to be made to the state-of-the-art for aircraft sensor suites. The current work proposes a sonic sensor solution to measure the angle of attack, speed, and total temperature of a flow field. Sonic and ultrasonic anemometers have the following advantages over conventional mechanical methods of measuring wind speed. They feature:

- No moving parts.
- No time lag to reach thermal equilibrium.
- Minimal flow interference.
- Less risk of icing interference.

- Capability of providing reverse flow parameters

The next section discusses the historical development of sonic anemometers and their limited application on aircraft.

2.3 Historical Background for Ultrasonic Anemometer

Development of sonic anemometers started in the 1950s with Suomi [18], but Carrier and Carlson are credited with developing the first operational sonic anemometer [19]. Suomi's initial intent was to determine the flow properties around a balloon, more specifically the temperature to within 1 degree C that was independent of other physical quantities. The theory behind these early concepts assumes:

1. The acoustic pressure is much less than the ambient static pressure.
2. Medium has constant specific heat ratio, γ.
3. Constant gas composition.

Knowing that the speed of sound is affected by temperature as well as by the moisture in the air and taking this into account, Suomi [18] shows the speed of sound including moisture effects as:

$$c = 20.067\sqrt{T\left(1 + 0.3192\frac{e}{p}\right)} \tag{2.3}$$

in the above equation, the speed of sound is given in meters per second and utilizes the vapor pressure, e, and ambient static pressure, p. Suomi's device used sonic pulses created by piezoelectric crystals going back and forth along a 1 meter path and used the difference in the time it took the pulse to travel along the path to determine the average velocity along the path as shown in Figure 2.8. The piezoelectric crystals act as the source and receiver depending on which direction the pulse is going. The platform and tubes in the middle are the amplification mechanism to create the acoustic pulse from one transducer and measure the response of the other transducer.

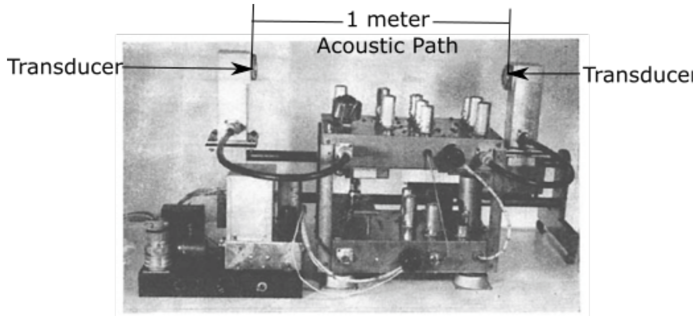

Figure 2.8: Laboratory model of Suomi's sonic thermometer [18]

This concept could be used to measure the atmospheric turbulence, but Suomi ran into difficulties in detecting the leading edges of the pulse, which led to inaccuracies in the measured data. Suomi was able to measure the temperature up to 88,000 ft pressure altitude and suggested it was possible to achieve measurements up to 120,000 ft pressure altitude. Schotland [20] went a different route in an attempt to make a sonic anemometer. Schotland's approach put the sound source opposite the receivers and used phase shift to determine the wind velocity, as shown in Figure 2.9.

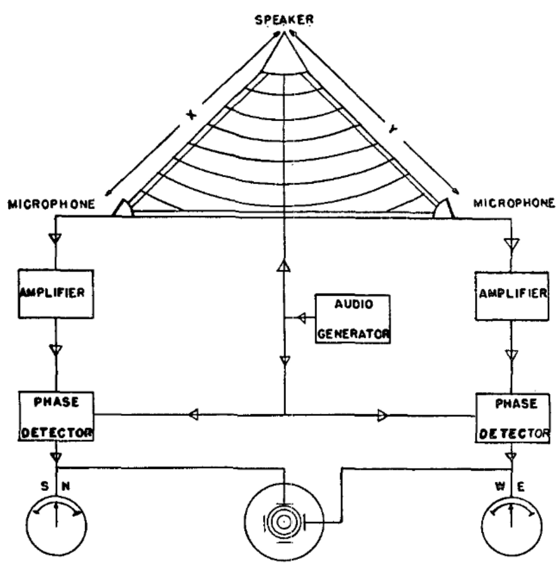

Figure 2.9: Schotland's anemometer [20]

This concept was able to achieve experimental results within 10% of a cup anemometer using three microphones, but suggested that the accuracy could be improved to within 1% with the use of six microphones. This methodology did have some issues with reflections contaminating the signal and causing interference with the wind measurements.

To avoid issues associated with detecting the leading edge of the pulse, some researchers attempted to use continuous wave signals [19, 21]. Coupling the continuous wave source with a comparison of the phase shift over the travel time was more robust and dependable than the pulse measurement technique and was used early on during the development of the sonic anemometer. The continuous wave concept developed issues of its own. This method of wind speed measurement had a problem with drifting of the zero-wind calibration as well as the interference in the measurement of multiple axes if the same frequency was used. This required a different frequency per axis measured to reduce this error source. A desire to simplify the system led researchers back to the pulsed approach to see if a solution could be determined for the initial problems with the early systems. Both methods are valid and were used in multiple designs throughout the 1960s and 1970s [22, 21, 23]. Figure 2.10 shows a three-axis sonic anemometer developed in the 1970s. It can be seen in Figure 2.10 that the measurement of all three-axis characteristics are not in the same measurement volume. The vertical component of velocity is measured below and to the left of the horizontal plane measurements.

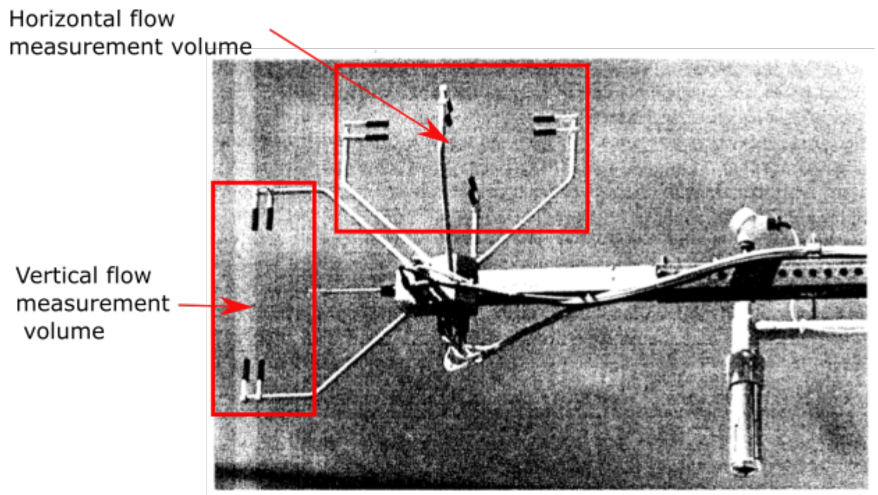

Figure 2.10: Three-axis sonic anemometer [24]

By 1968, the sonic anemometer had been developed enough to be used in large-scale field measurements. The 1968 Kansas experiments featured pulse-type anemometers developed in Japan that were designed to optimize spectral response [25]. The design of ultrasonic anemometers continued to evolve and improve [26]. One of the main drawbacks of the early ultrasonic anemometers was cost. The ultrasonic transducers and receivers were expensive, leading to high acquisition costs, but there are some designs that attempted to reduce costs through design modifications and using less expensive receivers [26]. Advancements in electronics and processing systems also assisted in the reduction of costs of the ultrasonic anemometers. Figure 2.11 shows a modern 3-axis ultrasonic anemometer with performance specifications similar to those given in Table 2.1. The modern 3-axis ultrasonic anemometer now measures all three axes with the same measurement volume. This is done by having the transducers at an angle from the horizontal and vertical planes.

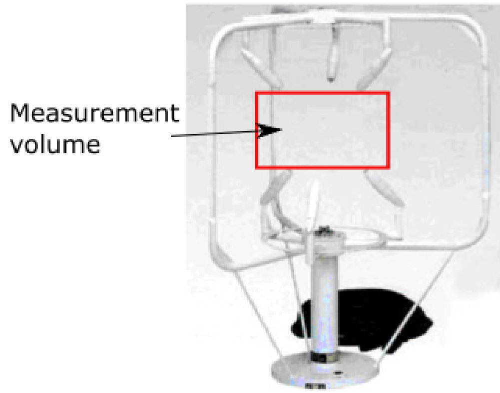

Figure 2.11: Modern ultrasonic anemometer [27]

Table 2.1: Young Model 81000 ultrasonic anemometer characteristics [28]

Parameter	**Value**
Speed Range [m/s]	0-40
Resolution [m/s]	0.01
Accuracy [%]	±1 for 0-30 m/s ±3 for 30-40 m/s
Azimuth Range [deg]	0.0-359.9
Elevation [deg]	±60.0
Angular Resolution [deg]	0.1
Accuracy [deg]	±2 for 0-30 m/s ±5 for 30-40 m/s
Sonic Temperature [deg C]	±50.0
Temperature Resolution [deg C]	0.01
Accuracy [deg]	±2 for 0-30 m/s

The Sonic Temperature mentioned in Table 2.1 is the temperature range calculated by the Young Model 81000 ultrasonic anemometer, and the lowest change in temperature that can be measured by the ultrasonic anemometer.

There has been recent work in different embodiments of the configuration of the ultrasonic anemometer. FT Technologies [29] has developed an acoustic resonance anemometer, shown in Figure 2.12. This concept measures the phase shift of the resonating ultrasonic signal due to the wind passing between the upper and lower plates. The benefit of this type of system is that it is thought to be more robust than the current three dimensional anemometers and maybe less prone to weather and environmental effects, but it should be noted that the acoustic resonance anemometer is only a two dimensional measurement as it is now. A three dimensional sensor could be built, but it is unclear at this time if the same measurement control volume could be used.

Figure 2.12: Acoustic resonance anemometer[29]

The initial intent of these sonic anemometers was to measure the velocity within a flow field. These devices can output various flow properties based on the measured propagation time and signal amplitude. One such flow property is temperature. Kaimal and Gaynor [30] conducted several experiments in using the sonic anemometer to determine the temperature of the flow field. This experimental investigation revealed the potential of the sonic anemometers to measure the flow temperature and noted that the sonic thermometers have a high threshold for noise when compared to the platinum wire counterpart. This study also suggested that the humidity must be corrected for to obtain an accurate result as humid air tends to attenuate the sound source more than dry air.

Using this same effect of source attenuation in humid air, Tekelioglu [31] attempted to use ultrasonic anemometers to measure the liquid water content (LWC) in droplet clouds. The current methods at the time were able to measure LWC for small droplet diameters (<40 μm), but for larger droplet diameters the measurement techniques were inaccurate. This concept uses the amount of attenuation of a signal to determine the amount of LWC in air, since the attenuation corresponds to a certain amount of LWC in air. From Tekelioglu's experimental study, the method seemed to perform well as a proof-of-concept, but there was some room for improvement on the accuracy of the calculated LWC.

The acoustic propagation method can also be used to determine the strength of the circulation and/or vortex inside a sonic path [32, 33]. Reference [32] used the sonic path sensor to determine the circulation about an airfoil in a wind tunnel. The theory for this concept is that the transit time of a sonic pulse traveling clockwise about the area enclosed by the acoustic pulse is different than the transit time of a sonic pulse traveling counter-clockwise, as shown in Figure 2.13.

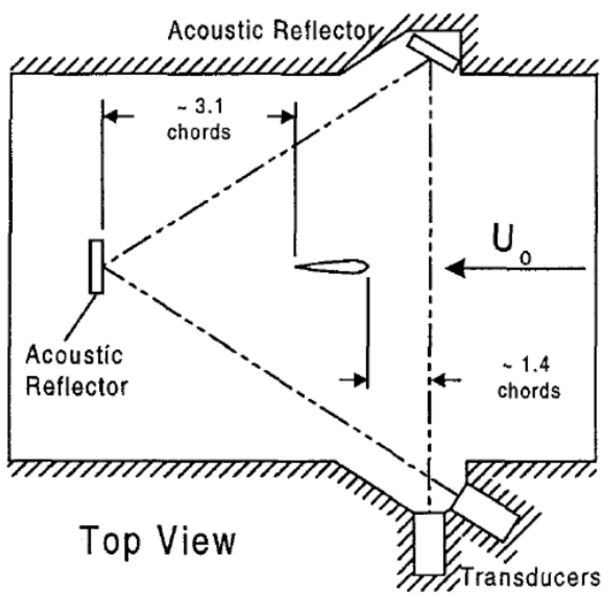

Figure 2.13: Setup to measure circulation [32]

There were some difficulties with the measurements in the tunnel due to the reflections from the tunnel walls, unsteady wakes trailing off of the model, and vortex shedding at stall angle of attack. The dynamic response of the airfoil was also tested using the sonic methodology. Rodenhiser et al. [33] attempted to determine the existence and strength of wing tip vortices near airport runways. Rodenhiser et al. suggest that this is a viable method of measuring vortex strength at the runways and the methodology was able to detect weak vortices, although it is noted that the wind affected the measured vortex strength.

More recently, there has been work by Otero et al. [34] to apply ultrasonic anemometry to jets at high subsonic speeds. Otero et al. were able to get some fairly consistent time of flight data up to Mach 0.83. The test setup showing the acoustic source and receiver outside of the jet flow is shown in Figure 2.14a. The calculated velocity was close to the actual jet velocity, but the results of the analysis seem to produce a velocity below the actual velocity as seen in Figure 2.14b [34]. The Root-Mean-Square (RMS) error of the velocity of -8.79 m/s.

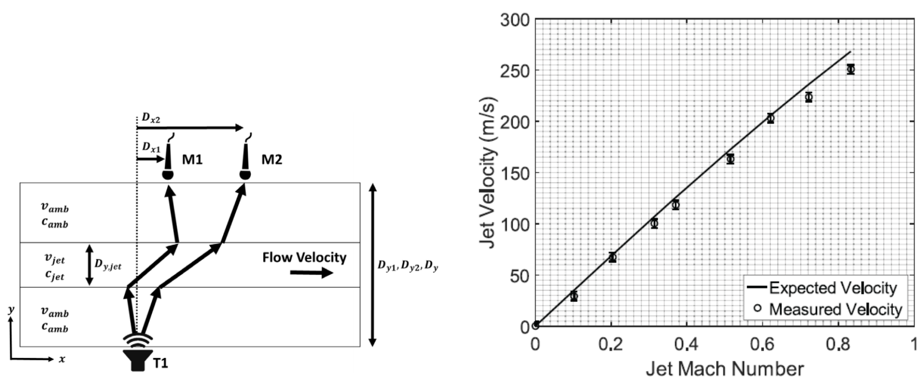

(a) Measurement setup (b) Jet velocity results

Figure 2.14: Jet velocity measurement setup and results [34]

Otero et al. attribute this discrepancy to geometric tolerance issues, but it is unclear whether or not that Otero et al. accounted for the fact that there is a large shear layer on either side of the jet which will have a reduced velocity much like a boundary layer. As shown by Ahuja et al. [35, 36], an extended ray path due to refraction through the shear layer can affect the time it takes for the signal to travel from the source to the receiver considerably depending upon the relative location of the source and the receiver. This could be the source of the error seen as the calculated velocity is less than the velocity in the center of the jet. Otero et al. used a similar technique to characterize the exhaust velocity of a gas turbine [34]. Sonic anemometers are not perfect, and the limitations and deficiencies of the current state of the art are discussed in the next section.

2.4 Sonic Anemometer Issues

During the design development of ultrasonic anemometers, a few deficiencies were exposed. One such issue is known as transducer-shadow effects. Transducer-shadow effects are changes in the acoustic path due to the presence of the transducers. Under certain flow conditions, the transducers generate a region of lower speed flow directly behind the transducer, known as a wake. This lower speed region modifies the acoustic path and changes the time of flight of the signal, which will reduce the accuracy of the sensor. Coppin and Taylor [26] noticed this issue during the testing of their ultrasonic anemometer design. It was noticed that the accuracy of the sensor was reduced over certain angles of attack, but could not directly attribute the reduction in accuracy to transducer-shadow effects because these inaccuracies are always coupled with the flow distortion due to the anemometer structure [37]. It was also determined that the sensor should be designed to reduce these shadow effects, but there are methods for compensating for the shadow effects using simple corrections.

During the initial use of sonic anemometers-thermometers, there was a concern for the influence of the probe itself on the flow field and how that might affect the data read by the sensor. Applied Technologies, Inc. (ATI) [38] developed a probe to reduce the flow distortion effects from the probe structure and transducers. The developed sonic-sensor features minimal structure with the three orthogonal axis separated from each other to reduce wake effects. While this configuration allows for the reduction of interference effects, it does cause the measurements for the wind to be in different control volumes, meaning that each measured velocity component is from a different location, as shown in Figure 2.15.

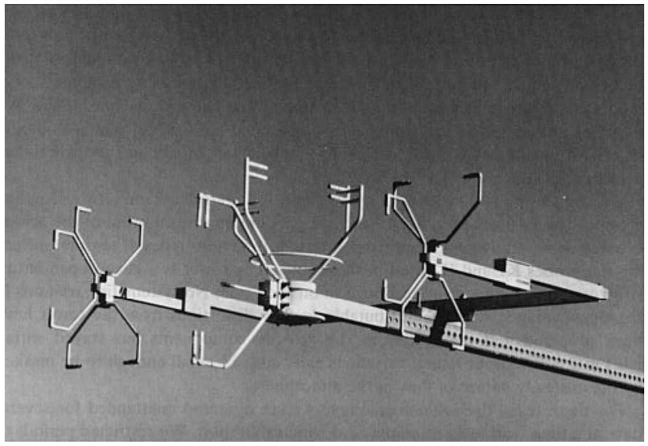

Figure 2.15: Ultrasonic anemometer test setup for minimizing flow distortion [38]

The sonic sensor also applied a simple shadow correction to each of the measured axes. The design seems to reduce the probe-induced flow distortion to negligible levels with a simple shadow correction. While designing to reduce the flow distortion and transducer-shadow effects is preferable, this is not always done practically. Grelle and Lindroth [39] attempted to determine corrections to the read data of the ultrasonic anemometer to account for flow distortion. This distortion effect also limits the design range of the applicable angle of attack for the ultrasonic anemometer and these errors are corrected for in both the horizontal and vertical directions [40]. Other researchers [41, 42, 43, 44] investigated the problem of flow distortion around ultrasonic anemometers and corrections to apply for deviations in angles of attack. Flow distortion is the effect of the sensor support structure on the flow. This is mainly seen in the response of the measurement in the horizontal and vertical planes. In the horizontal plane, the velocity component in one direction should have a cosine response as the angle of the wind is changed, and a sine response for the vertical component of velocity, as shown in Figure 2.16.

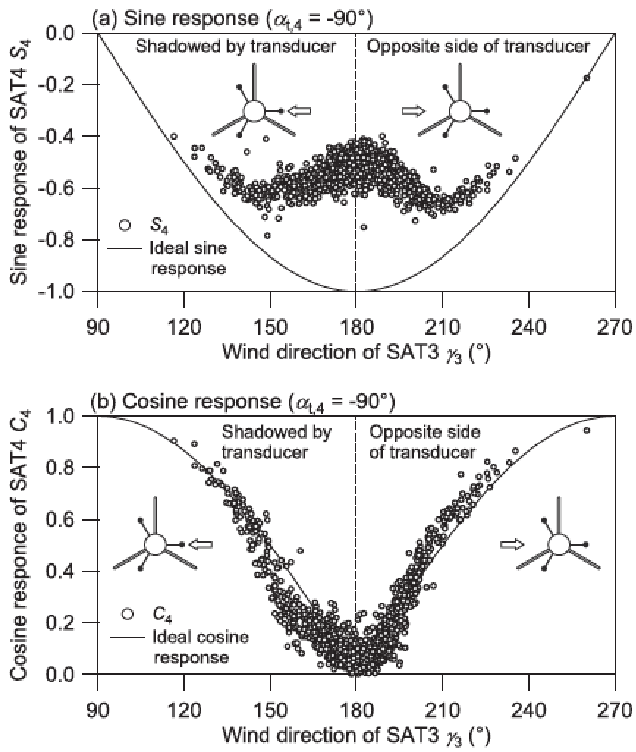

Figure 2.16: Sine and cosine response of flow distortion effects [42]

The sine and cosine effect are "ideal" conditions where the sensor structure has no effect on the incoming flow. In reality, the sensor structure modifies the incoming flow, so the measured flow angle is not the free-stream flow angle. It is difficult to determine the exact effects of flow distortion experimentally because the distortion effects are not independent of the turbulent intensity of the flow [37].

The structure on which the anemometer is mounted, also known as the tower, can also introduce other errors in the measured data for the ultrasonic anemometer. Siebert [45] analyzed the effects of the vibrating tower on the measured data of an ultrasonic anemometer. Siebert noticed some changes in the temperature spectrum that were not in the velocity spectrum. Performing some flow tests while striking the tower structure to induce vibrational modes, it was discovered that the vibrations of the tower caused small changes in the distance between the transceivers, and therefore causing fluctuations in the measured temperature, which were sometimes greater than the “noise” of the system.

The flow distortion effects are also attempted to be filtered out. These filtering effects attempt to weed out unwanted noise and attenuation effects to get more accurate results [46, 47]. Villanueva [48] outlines a method to measure flow parameters from an ultrasonic anemometer using fuzzy data fusion as an alternative to the more conventional methods. Analysis of initial assumptions have also been researched, more specifically the assumption of constant speed of sound [49]. In Friehe’s work[49], it was determined that any errors are due to the assumptions of constant speed of sound by different signal processing techniques. The history of the attempts of extending sonic anemometry to aircraft are discussed in the next section.

2.5 Application of Sonic Anemometry on Aircraft

Application of sonic anemometry on aircraft was attempted in the 1960s, but the low computing power on the aircraft as well as sensor design issues prevented feasible applications on aircraft [50]. During the early 1970s, Maeda proposed an altimeter and a vertical velocimeter based on sonic anemometer theory. This concept utilized the ground as a reflecting plane to determine the vertical speed and altitude using sonics. Maeda [51], suggests that this technology could be used in take-off and landing of aircraft. The work tested the concept on a helicopter, but was only applicable for altitudes less than 30 meters. Figure 2.17 shows a schematic of the concept.

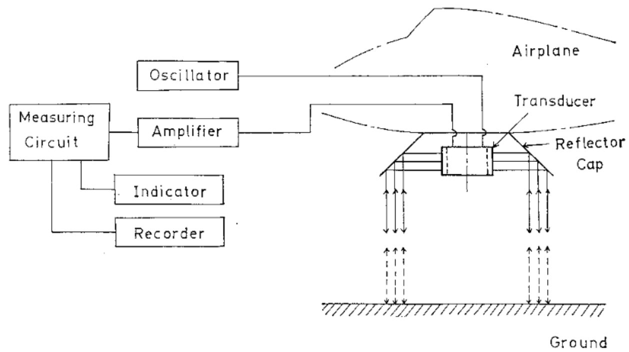

Figure 2.17: Ultrasonic altimeter and vertical velocimeter concept [51]

In 1991 researchers at the University of Paris expressed renewed interest in the use of aeroacoustics to measure the flow properties around aircraft. The early prototypes of their Airborne Ultrasonic Anemometer Thermometer (AUSAT) used triaxial configurations similar to that of the ground-based counterparts, but vibrations and interference problems required the researchers to enclose the sensor in a duct to be unidirectional. The flow in the duct was designed using Computational Fluid Dynamics (CFD) methods to be as close to the free stream as possible. The AUSAT was then flight tested on multiple aircraft, which covered a range of speeds of 80 to 220 kts. One installation on the flight test aircraft is shown in Figure 2.18.

Figure 2.18: AUSAT sensor mounted [50] on a general aviation aircraft

The physical size of the AUSAT is given in Table 2.2.

Table 2.2: AUSAT size dimensions [50]

Parameter	**Value**
Length [m]	0.620
Inner Diameter [m]	0.220
Outer Diameter [m]	0.150
Channel Length [m]	0.212
Weight [kg]	15

The measured data from the AUSAT correlated well with the data measured from other sensors on the flight test aircraft. While there was good correlation, Cruette [50] mentions some components that were not taken into account in the AUSAT, which could further improve the measurements. Also, the AUSAT is large and heavy for deployment on commercial and general aviation aircraft.

In 1996, Loschke et al. [52] filed a patent on a flush air data system that attempted to measure the airspeed and angle of attack using acoustic propagation of the boundary layer noise. This concept utilized cross-correlation of a reference receiver upstream of an array of receivers. The reference receiver would measure the boundary layer noise and apply the cross-correlation to determine how much time it took for the boundary layer noise to travel to the downstream array. There is no data on any flight tests that may have been performed with this system, so no comparison can be made to the accuracy of this method. The method relies on an approximation of the velocity profile near the surface to determine the free-stream velocity since there is a velocity gradient in the boundary layer. The approximation used to determine the flow outside of the boundary layer is just that, an approximation. No matter how good the approximation is, it is based on previously defined data, and will introduce inaccuracies in the calculated flow speed. However, the angle of attack measured through this method may be accurate enough for use in air data systems, provided that the air flow around the body is accounted for in the angle of attack calculations.

Another ultrasonic sensor patent was just granted in February of 2021 to Rosemount Aerospace[53]. The technology outlined in the patent is similar to the Loschke patent and measures the flow in the boundary layer of the aircraft. The Rosemount sensor utilizes a single transducer in the center of a ring of receivers and uses normal ultrasonic anemometer techniques to calculate the flow speed and direction. Like the Loschke patent, the Rosemount sensor is passive in that it uses the sound field generated by the aircraft moving through the atmosphere, but mentions the use of active ultrasonic signal generation.

Yazawa et al. [54] developed a smaller scale ultrasonic anemometer for aircraft in 2001. Yazawa applied a four component ultrasonic anemometer for aircraft applications shown in Figure 2.19. Yazawa's ultrasonic anemometer works on the same principle as the ground-based, meteorological concepts discussed earlier in this chapter. The main difference is the fairing around the transducers and the reduction of the transducer support wake impacting the measurement volume. Figure 2.19 shows these fairings and the position of the transducers in the fairings. The wake of the transducer fairings may impact the measured data at high angles of attack and/or high sideslip angles, and it is unclear how this might be mitigated.

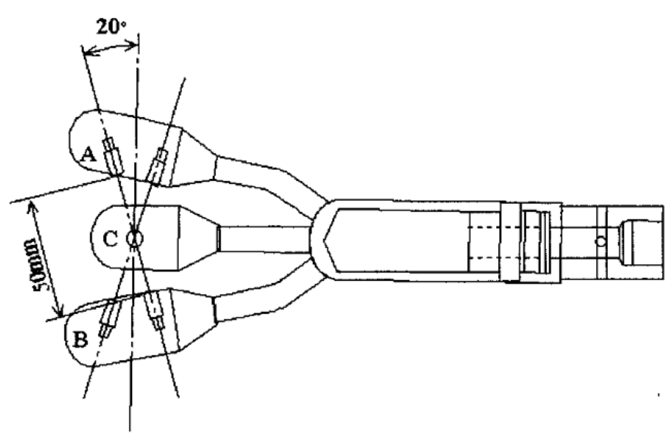

Figure 2.19: Ultrasonic anemometer for helicopter applications [54]

Yazawa's main intent was atmospheric research and did not measure or calculate the temperature using the aircraft ultrasonic anemometer. The ultrasonic anemometer was used to determine the wind velocity from a platform mounted to an aircraft. The aircraft motion was subtracted from the signal to determine the wind velocity. The calculated velocity showed good agreement with data measured from a ground station near the flight test location. Matayoshi et al.[27] then used Yazawa's design in application to helicopter flight. The ultrasonic anemometer design was placed on a boom in front of the helicopter fuselage and far outside of the downwash of the helicopter rotors, as shown in Figure 2.20a. The sensor can also be placed on the lower side of the fuselage to avoid the influence of the rotor downwash. This is shown in Figure 2.20b.

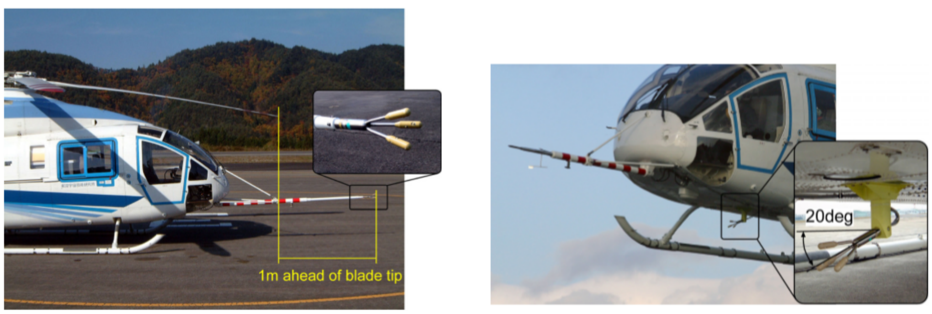

(a) Helicopter boom installation (b) Helicopter fuselage installation

Figure 2.20: Ultrasonic anemometer mounted on helicopter [27]

Matayoshi [27] recorded the max operating velocity as 96 m/s. The velocity limit of this design limits the application of this type of ultrasonic anemometer to low-speed rotorcraft and small aircraft. Matayoshi was mainly interested in velocity components and temperature was not determined from the collected data. Castillo [55] placed a commercial ultrasonic anemometer on the nose of a UAV, as shown in Figure 2.21, to measure the angle of attack, angle of sideslip, and component speeds. The data from the ultrasonic anemometer is compared to data from a GPS/IMU. The ultrasonic data did not line up with the IMU data, but these errors could be due to shadow/flow distortion effects from the way the sensor was installed.

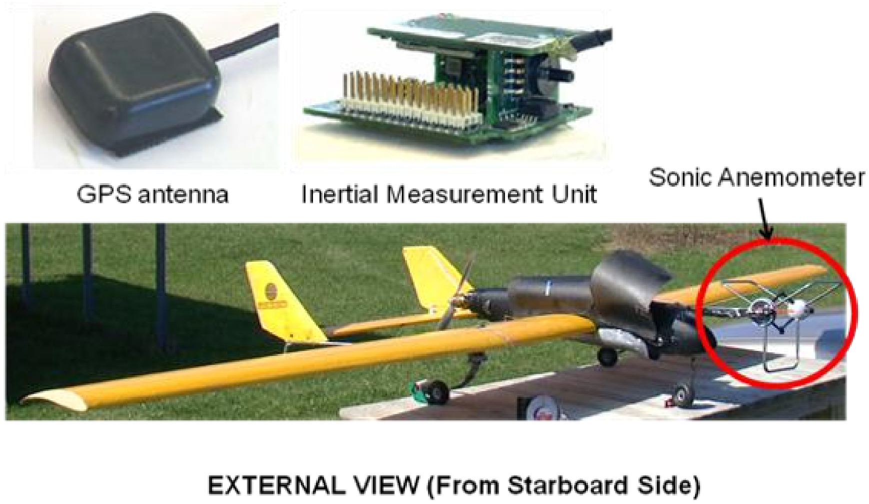

Figure 2.21: Ultrasonic anemometer installed on UAV [55]

From Figure 2.21, it can be seen that there is a large circular support object directly upstream of the sensing volume. This could cause wake interference effects of the flow separating around the support structure. Curtiss-Wright has applied an ultrasonic sensor to helicopters for low-speed applications [56]. This sensor, uses the time of flight of ultrasonic pulses bouncing off a reflecting plate as shown in Figure 2.22. The sensor is placed on the tail of the helicopter to measure relatively clean airflow.

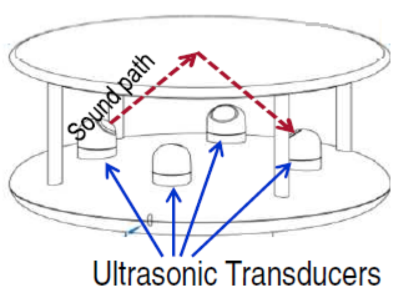

Figure 2.22: Schematic of Curtiss-Wright low-speed ultrasonic anemometer [56]

This concept measures the flow direction and speed, it is not clear the maximum speed that this concept measures. Reference [56] suggests it is only for low-speed applications and a pitot tube is used for speeds greater than 55 kts. The minimum accuracy of this probe is also ±3 kts at the low end and increases to ±4 kts at around 55 kts.

2.6 Research Scope and Summary Comments

From the literature review, it is clear that the current sonic/ultrasonic anemometers measure the flow speed and direction reasonably accurately for low-speed applications. The current work develops a system that can be effectively installed on commercial aircraft to potentially replace and combine the pitot-static tube, angle of attack sensor, and total temperature probe with a single sensing unit. This work aims to lay a foundation for application of sonic sensors for high subsonic Mach numbers at which commercial aircraft operate. The current ultrasonic anemometers are based on the propagation time of the ultrasonic source between three pairs of transceivers. The typical method for determining the time of flight between the transceivers is to look at the time the leading edge of the signal reaches the opposite transceiver. Each pair of transceivers is placed at a known angle around a flow volume to determine the three-dimensional flow components. The current work focuses on a two dimensional problem only for velocity and angle of attack (or angle of sideslip depending on the orientation of the sensor). This will allow for a reduction in the required number of transceivers.

The current work also includes an investigation into the source signal, both frequency and type (burst, chirp, pure tone, and broadband noise). Variation in the frequency of the source signal will impact the SNR. As the flow velocity is increased, the hydrodynamic noise increases as a function of the cube of the velocity. Increasing the source signal frequency into the ultrasonic range (frequencies above 20 kHz) will increase the SNR ratio as the ultrasonic frequencies of the hydrodynamic noise are damped out relatively quickly, which means they have minimal effect on the overall noise spectra and allow the signals detected by the receivers to be filtered such that only the high frequency data is retained. The setup used by Otero et al. [34] has produced results up to Mach 0.83 using an ultrasonic source, but it is fairly good only if the flow direction is already known. As discussed earlier, the errors they see at the higher velocities could be the errors due to the refraction of the sound signal through the shear layer of the jet. Otero's experimental setup featured the ultrasonic transceivers outside the measurement flow field. This reduces the hydrodynamic noise over the transceivers, but will not be applicable for installation on aircraft as the receivers will be immersed in the flow about the aircraft (the receivers will be moving along with the aircraft). The refraction of the acoustic signal will not be as prevalent, but the SNR will be reduced due to the increase of the hydrodynamic noise.

The current work places the receiving elements around an acoustic source. The angular spacing of the acoustic receivers (microphones) will allow the flow speed and direction in the plane of the receivers to be determined. This methodology can also be applied to high-speed flows. As the flow velocity approaches the speed of sound (Mach 1), the acoustic point source signal will have an increasingly difficult time propagating upstream from the point source. Once the flow velocity reaches sonic, the acoustic signal can no longer propagate upstream and can only be pushed downstream by the flow. This limits the location of the receivers depending on the desired maximum velocity and angle of attack range. It should be noted that the only limitation of the method is on the location of the receivers and not the velocity or angle of attack. Having the source and receiving elements all on the same plane will reduce the interference effects due to the assembly support structure. The applied ultrasonic anemometry technology applied to aircraft is rather large and obtrusive when compared to other sensors on aircraft. This can be seen in Figure 2.18 and Figure 2.20 in the AUSAT size as well as the size of the ultrasonic speed sensors on the helicopters. As mentioned earlier, all aircraft must have redundant systems to operate safely. The size and the drag of the current technology as applied to aircraft, makes the barrier to service nearly insurmountable due to the requirement of redundant systems. The current work pays particular attention to ensuring that the sonic sensor is small enough in size so as to reduce or maintain the drag force due to the pitot, angle of attack, and total temperature systems.

As outlined at the outset, the main purpose of my developing the sonic sensor in the present work was to use them on a flight vehicle as a replacement of Pitot probes, as such, the data processing must occur at a rate that is compatible with the air data system/on board computer. Therefore, the rate at which the sonic sensor must process the data is considered during development. After discussions with the engineers at Aerosonic Corporation, a manufacturer of pitot probe-based flow sensors for aircraft and sponsor of this project, the desired rate at which the sensor calculates the velocity and angle of attack is 20 Hz, or once every 0.05 seconds. This will allow the data to be refreshed often enough for the other flight systems (e.g., autopilot, engine controller, etc.) to utilize the calculated data for flight operations. As will be discussed later, the processing methodology to determine the time delay between two signals works better over a longer sampling time. This work includes an investigation into the minimum sample time required to achieve an accurate signal propagation time. While the desired sample time is 0.05 seconds, this is not necessary for all applications of this system. The proposed sensor can be used in applications with relatively steady flow such as, wind tunnels and water tunnels with longer sampling times. Otero et al. [34] was able to achieve good results up to Mach 0.83 using one second for the sample time and sampling at 1.25 Million samples per second over one second of sampling time. This work presents methods for reducing this sample time to be able to tie into the aircraft air data systems.

Filling in the gaps discussed above, is the backbone of this research. The technical approach for determining the flow properties and facilities used in pursuit of the objective of this work is given in the next chapter (Chapter three).

CHAPTER 3
TECHNICAL APPROACH AND FACILITIES

3.1 Ultrasonic Anemometer Theory of Operation

Ultrasonic anemometers work based on the time required for a specific signal to propagate between a transmitter and a receiver. For pulsed-type anemometers, the velocity components of a flow are determined based on the propagation time of two signals sent in opposite directions over a fixed distance. This methodology assumes that the flow velocity, direction, and temperature are constant between the transmitter and receiver. Figure 3.1 shows a rough sketch of the operation of an ultrasonic anemometer. A pulse is emitted from transducer one located in a flow moving from transducer one to transducer two at the speed of U. The propagation speed of the signal between transducer one and transducer two is $c + U$. The pulse emitted from transducer two travels back to transducer one at $c - U$. If the distance, L, between the transducers is known, and the time of propagation is measured, the velocity and speed of sound can be determined with t_1 being the time it takes for the signal to travel between transducer 1 and transducer 2, going with the flow, and t_2 is the time it takes the signal to travel from transducer 2 to transducer 1 against the flow.

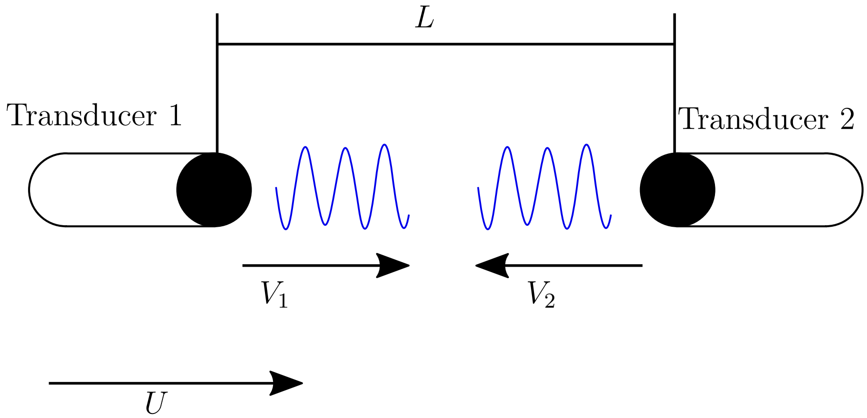

Figure 3.1: Basic ultrasonic flight path between two transducers with the flow direction in line with the transducers

This definition of the problem creates a simple system of equations with two equations and two unknowns:

$$V_1 = \frac{L}{t_1} = c + U \tag{3.1}$$

$$V_2 = \frac{L}{t_2} = c - U \tag{3.2}$$

Solving this system of equations yields the following as the calculated velocity.

$$U = \frac{L}{2}\left(\frac{1}{t_1} - \frac{1}{t_2}\right) \tag{3.3}$$

This simple derivation assumes that the flow is of uniform velocity, U, between the transducers and the speed of sound, c, is constant. There is some hesitation to use the above derivation for non-uniform flow-fields. If the flow velocity in the measurement volume between the transducers is known as a function of distance and time, the theory above will still work because it is just a vector addition of the flow velocity to the speed of sound in the fluid. Consider the case that there is a large wake behind transducer 1 such that the flow velocity over half of the distance between transducer 1 and transducer 2 is one-third of the free stream flow speed. After this point, the flow transitions to the free stream velocity. The values for t_1 and t_2 would be drastically different than for the uniform flow case. The measured flow speed would effectively be an average of the flow in the volume between the transducers which would be lower than the free stream values. The argument can be made that the effects of non-uniform flow can be calibrated out of the system because the flow would consistently behave in that way. Based on the concept for the general theory of operation of a sonic anemometer presented in this section, the theory of the aircraft sonic sensor is given in the next section.

3.1.1 Aircraft Sonic Sensor Theory of Operation

For aircraft and high-speed applications, a different approach for the sonic sensor is considered. As the flow speed is increased, the acoustic signal will take increasing longer time to reach the upstream receiver until the flow reaches sonic speeds. Once the flow speed reaches the speed of sound, the signal can not propagate upstream at all. Consider an acoustic signal emitted equally in all directions from point S and received at R_2, R_3, and R_4. The speed of propagation, V_S, of the acoustic wave is given by:

$$V_S = \frac{L}{t} \tag{3.4}$$

In the absence of flow, an acoustic wave propagates in air at the speed of sound. With the addition of flow with velocity, U, and angle of attack, α, the speed of propagation of the acoustic wave is then the vector sum of the flow velocity and the velocity of propagation in static air. For an acoustic wave emanating from a point sound source propagating in all directions at the speed of sound, at each point on the wave, the wave is traveling with some propagation velocity (speed and direction). If the point sound source and the receiver are fixed in space, there is a certain propagation velocity (speed and direction) that, when added to the flow velocity, will result in the acoustic signal reaching the receiver in the least amount of time. The propagation velocity vector changes with flow velocity, but the magnitude of the propagation velocity vector is the speed of sound of the medium. Figure 3.2 shows a sketch of the velocity vectors used to derive the relationship between c, U, and α for the sonic sensor. Starting with a defined reference line through the source and receiver, R_1, the angular spacing, θ, ϕ, and ω are defined as the angle between the reference line and the receivers R_4, R_2, and R_3, respectively. Similarly, the distance between the source and the receiver, L_1, L_2, and L_3 are defined as the distance from R_1 to R_2, R_1 to R_3, and R_1 to R_4, respectively. All geometric parameters defined in Figure 3.2.

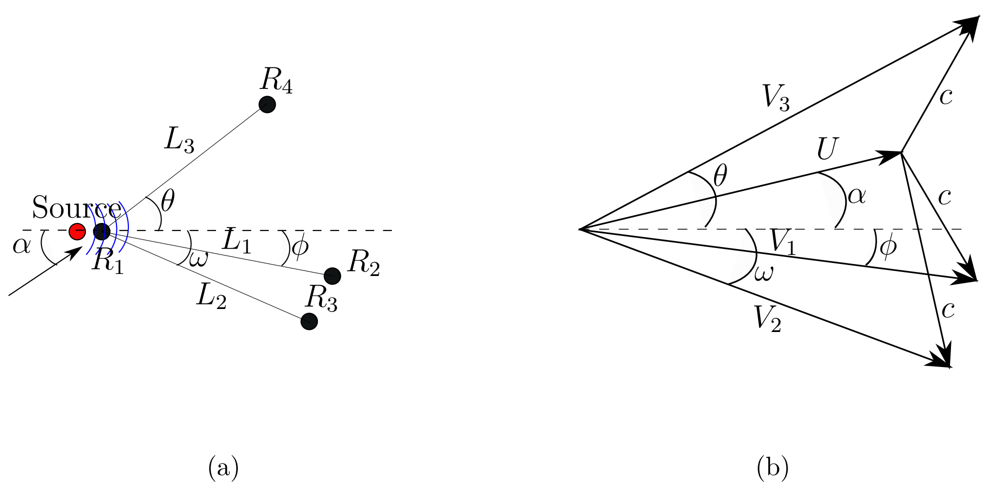

Figure 3.2: (a) Sonic sensor definition sketch and (b) Velocity vectors

Assuming that the speed of sound, c, is constant and using the law of cosines for each velocity triangle, the following equations are obtained:

$$c^2 = V_1^2 + U^2 - 2V_1 U \cos(\phi - \alpha) \tag{3.5}$$

$$c^2 = V_2^2 + U^2 - 2V_2 U \cos(\omega - \alpha) \tag{3.6}$$

$$c^2 = V_3^2 + U^2 - 2V_3 U \cos(\theta - \alpha) \tag{3.7}$$

Note that, this system of equations has three equations and three unknowns, c, U, and α. The velocity vectors, V_i, are given based on the time delay and the distance between the source and the receiver. After some algebraic manipulation, an equation for the flow velocity, U, is given by Equation 3.8.

$$U = \frac{V_2^2 - V_1^2}{2\left(V_2 \cos(\omega - \alpha) - V_1 \cos(\phi - \alpha)\right)} \tag{3.8}$$

After another round of algebraic manipulation and utilization of the following trigonometric relationship, the angle of attack, α, is given in Equation 3.10.

$$\cos(\alpha - \beta) = \cos\alpha \cos\beta + \sin\alpha \sin\beta \tag{3.9}$$

$$\tan\alpha = \frac{\frac{V_3^2 - V_2^2}{V_2^2 - V_1^2}\left(V_2 \cos\omega - V_1 \cos\phi\right) - \left(V_3 \cos\theta - V_2 \cos\omega\right)}{\left(V_3 \sin\theta - V_2 \sin\omega\right) - \frac{V_3^2 - V_2^2}{V_2^2 - V_1^2}\left(V_2 \sin\omega - V_1 \sin\phi\right)} \tag{3.10}$$

With α known, the velocity of the flow can be determined through Equation 3.8 and the speed of sound can be calculated from Equations 3.5, 3.6, or 3.7.

The above equations have a significant meaning, in that they do not set a limitation on the flow speed. If the ultrasonic anemometer case is considered, meaning that the transceivers are aligned with the flow and sending an acoustic signal back and forth, as the flow velocity is increased to near sonic speeds the time of flight of the acoustic signal will become larger and larger for the signal sent upstream. Once the flow velocity is increased to sonic, the time of flight of the upstream path will be infinite as the signal cannot propagate upstream due to the flow velocity. With the current formulation, all the signals are propagating downstream, eliminating the singularities at sonic flow speeds and faster.

For the no-flow conditions, it is assumed that the sound wave front propagates in all directions as a spherical wave. In two dimensions, this is shown in Figure 3.3.

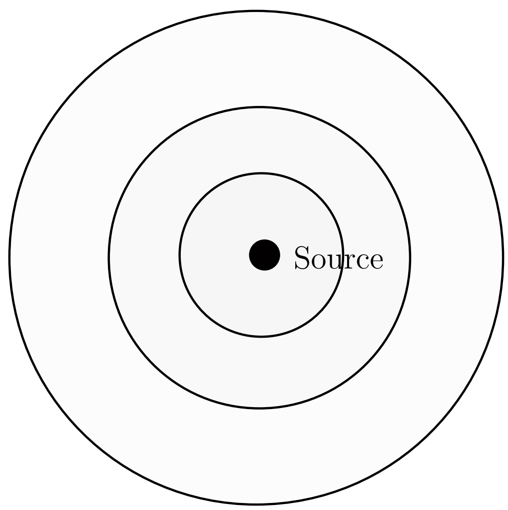

Figure 3.3: Acoustic waves emitted in all directions from a point source immersed in zero flow velocity

With the addition of subsonic flow at speed U_∞, the molecules involved with the transfer of the pressure wave are pushed downstream causing a slight Doppler effect to the pressure wave as shown in Figure 3.4.

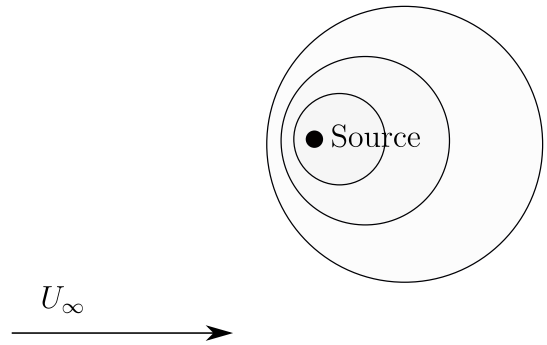

Figure 3.4: Acoustic waves emitted from a point source in subsonic flow

Increasing the flow velocity to sonic speeds, the acoustic wave begins to pile up and is not allowed to propagate further upstream as in the subsonic case. This is shown in Figure 3.5.

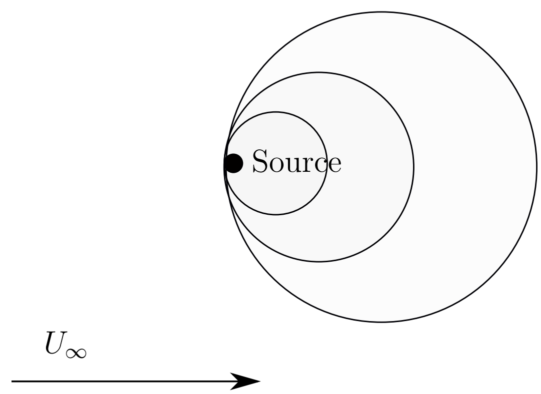

Figure 3.5: Acoustic waves emitted from a point source in sonic flow

Increasing the flow velocity into the supersonic regime, the acoustic wave is pushed back further by the flow and creates a zone of silence forward and around the acoustic source, defined by the Mach angle. Figure 3.6 shows the zone of action behind the Mach angle and zone of silence upstream of the Mach angle for supersonic flows.

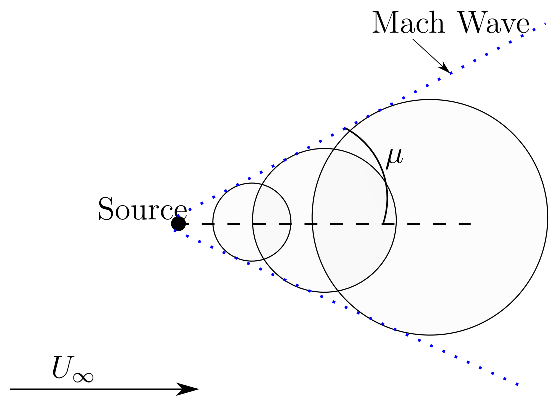

Figure 3.6: Acoustic waves emitted from a point source in supersonic flow

The Mach angle is given by:

$$\mu = \sin^{-1}\left(\frac{1}{M}\right) \tag{3.11}$$

For higher speed applications, the Mach angle must be considered for this type of sensor. If the receiver is in the zone of silence (outside the zone of action defined by the Mach angle), no signal will reach the receiver and will lead to errors in the measured data. Figure 3.7 shows contours for the zone of action as a function of Mach number and provides the maximum angular spacing of the receivers to remain in the zone of action to allow the signal to propagate downstream. This must be considered depending on the maximum speed that the sensor is designed to measure.

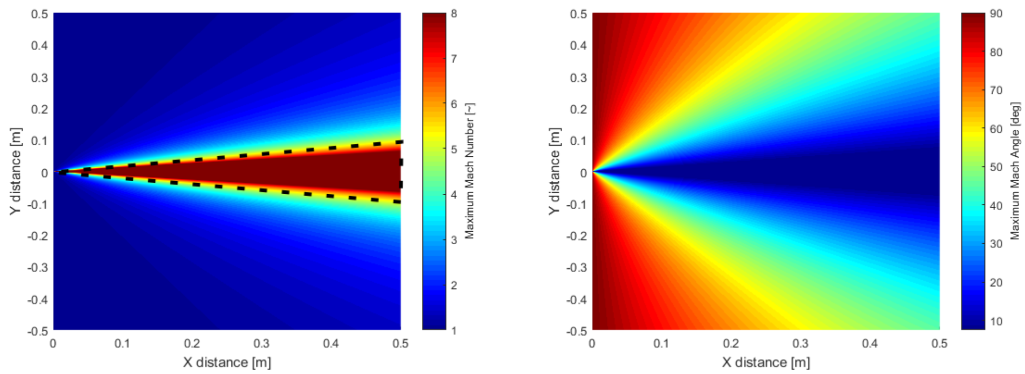

(a) Zone of action for given Mach numbers (b) Maximum angle allowed to place receivers for given Mach numbers

Figure 3.7: Mach limitations on receiver placement

Figure 3.7 helps to define where the receivers must be placed for the maximum desired Mach number to be measured. For example, if the sensor is to measure up to a Mach Number of 5.3, the transducers must be placed inside the dashed cone of Figure 3.7a. The Figure 3.7b shows the Mach angles at the Mach numbers defined in Figure 3.7a. Considering our example Mach number of 5.3, and transferring the dashed cone to Figure 3.7b, the maximum absolute value of the receiver angular spacing from the reference line is approximately 20 degrees. This is just another way of looking at the angular spacing limit as a function of the desired measured Mach number.

Up to this point there has been no assumption for the air other than the speed of sound is constant. This implicitly defines that the air composition is not changing for the short duration of the time of flight of the acoustic signal. The velocity, speed of sound, and angle of attack measurements are purely based on the time required for the acoustic signal to propagate over the distance between the source and the receiver. Making the further assumption that air is a perfect gas, which is a valid assumption for most applications in Earth's atmosphere, the speed of sound can be calculated by:

$$c = \sqrt{\gamma R T} \tag{3.12}$$

For a calorically perfect gas, the ratio of specific heats, γ, is constant. The other term, R, is the Universal Gas Constant, leaving the static temperature, T, as the only unknown. This means that utilizing the acoustic properties of air, the air speed, speed of sound, angle of attack, and static temperature are determined all with the same sensor at the same instant in time. If it is also assumed that the process is adiabatic and reversible, isentropic, the total temperature can be determined by:

$$\frac{T_t}{T} = 1 + \frac{\gamma - 1}{2} M^2 \tag{3.13}$$

The assumption of an isentropic process also allows for the calculation of the pressure and density ratios using the following relationships.

$$\frac{p_t}{p} = \left(\frac{T_t}{T}\right)^{\frac{\gamma}{\gamma-1}} \tag{3.14}$$

$$\frac{\rho_t}{\rho} = \left(\frac{T_t}{T}\right)^{\gamma} \tag{3.15}$$

If either the static pressure or total pressure is measured, the other pressure term can be calculated, and the density values can be determined with the perfect gas law. The test facilities used to experimentally validate the sonic sensor are given in the next section followed by the data acquisition setup and the data analysis methodology.

3.2 Facilities

The facilities at the Georgia Tech Research Institute (GTRI) are used to generate the uniform flowfields required for this work. The initial low-speed tests are performed in

GTRI's Model Test Facility (MTF) and the higher speed tests are performed in GTRI's Small Open-jet Facility. These facilities are described below. Table 3.1 presents the test section size and the maximum Mach number achievable in the respective facilities.

Table 3.1: GTRI test facilities used in experimental testing

Facility	**Test Section Cross Section**	**Maximum Mach Number**
MTF	30 in. x 30 in.	0.15
Small Open-jet Facility	8 in. x 8 in.	0.49

3.2.1 Model Test Facility

Low-speed testing (0<M_∞< 0.1) is performed in the Georgia Tech Research Institute Model Test Facility. This facility, schematic shown in Figure 3.8, is a closed circuit wind tunnel with a test section cross section of 42" by 30" and is capable of reaching speeds up to 120 mph.

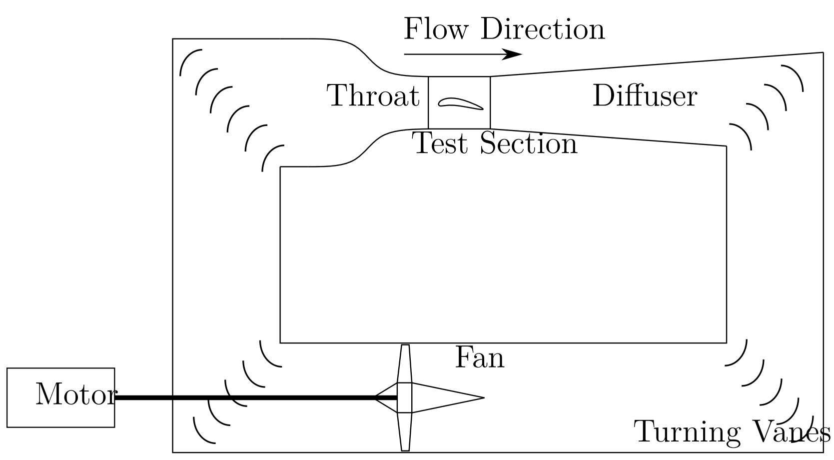

Figure 3.8: Model test facility schematic

For the testing of the sonic sensor, an insert, Figure 3.9, is created for the test section to add a turntable to allow for the testing of the sonic sensor at varying angles of attack.

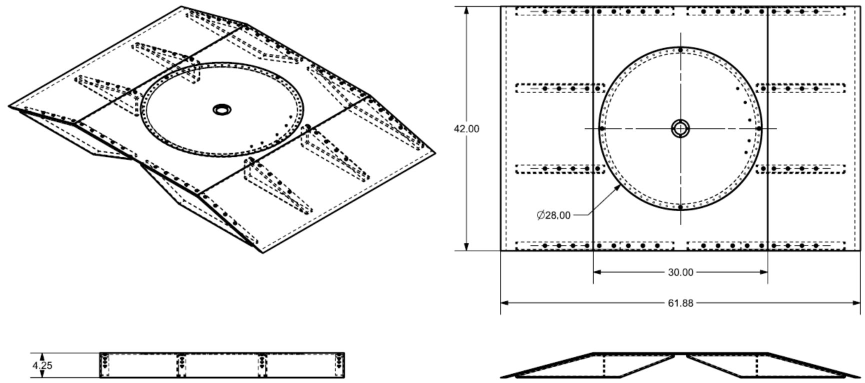

Figure 3.9: Drawing of model test insert

Any flow features that reduce the velocity over the sensing volume (boundary layer, flow separation, etc.) will cause a reduction in the measured velocity therefore, the insert spans the width of the test section to ensure uniform flow over the sensor. Four PCB Surface-mounted Electret microphones are used as the receivers and positioned as shown in Figure 3.10.

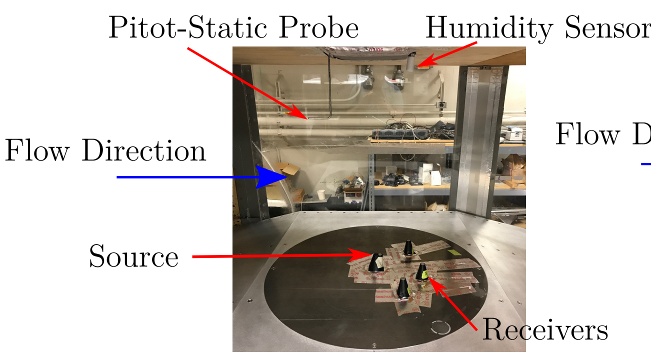

(a) Test Section

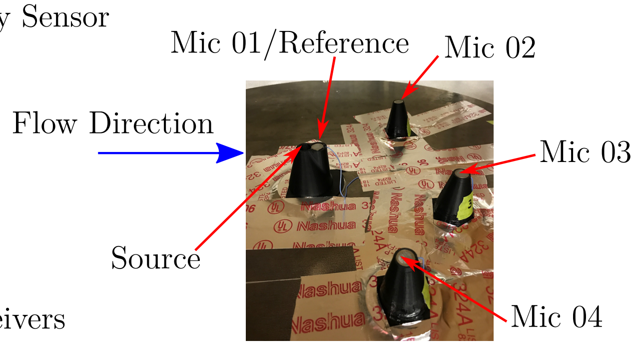

(b) Model Setup

Figure 3.10: Model test facility test setup

The microphones, labeled Mic 01-Mic 04 in Figure 3.10, are offset from the surface to get the diaphragm out of the boundary layer. The boundary layer over the insert is described in the next section.

Boundary Layer Profile over the Sonic Sensor Insert

As the fluid flows over a surface, a region of large velocity gradients is formed in a thin layer close to the body due to frictional forces causing a no-slip condition. This thin layer of large velocity gradients is called the boundary layer. The thickness of the boundary layer grows along the length of the surface. Figure 3.11 shows a representative boundary layer growth along the surface and velocity profile for laminar and turbulent boundary layer. Outside the boundary layer, the velocity is equal to the free stream, U_∞.

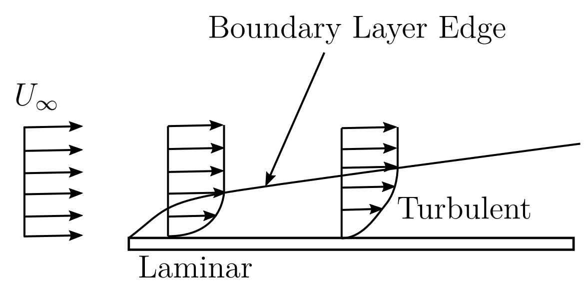

Figure 3.11: Boundary layer definition

If the sound source and receivers are within the boundary layer, near the wall, the measured velocity will be less than the free-stream velocity as the signal propagates near the surface and in the boundary layer. Therefore, the boundary layer over the model must be known to allow for the acoustic signal to travel to the receivers in the free-stream flow. A pressure rake is used to determine the height of the boundary layer in over the wind tunnel insert. The pressure rake is traversed in the streamwise direction to determine the growth of the boundary layer from the leading edge of the insert. Figure 3.12 shows how the boundary layer properties are measured in the wind tunnel.

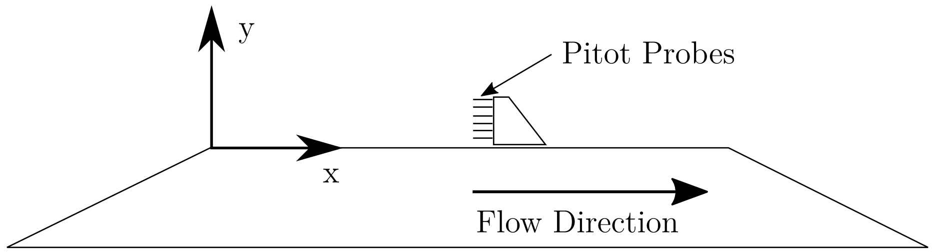

Figure 3.12: Boundary layer rake test definition

Using the boundary layer rake in the MTF, the boundary layer profiles are determined as shown in Figure 3.13. The boundary layer rake is traversed along the flow direction in the test section to determine the boundary layer growth along the insert. The boundary layer growth is shown for 50 ft/s, Figure 3.13a, and 150 ft/s, Figure 3.13b, to determine the support offsets for the microphones and ensure the source and receiver are in uniform flow. For both cases, the boundary layer is below one inch, therefore the supports should be more than this value to have the microphones and source out of the boundary layer.

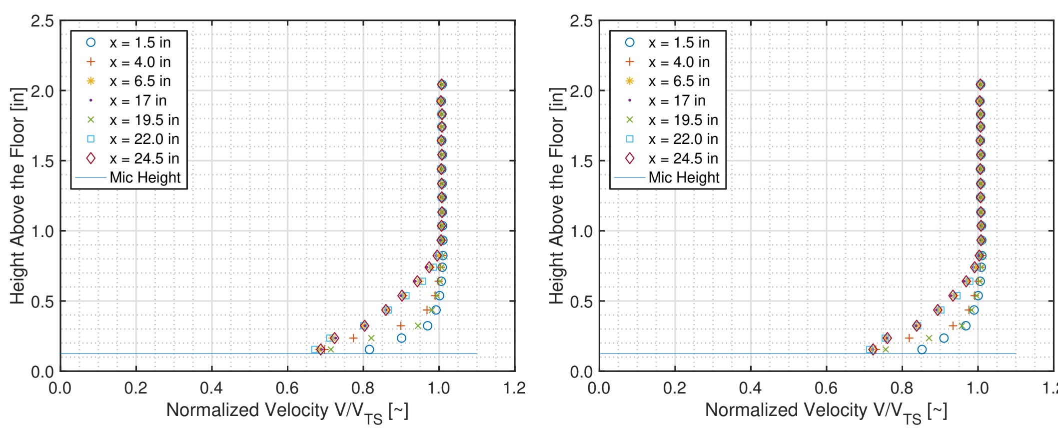

(a) Test section velocity of 50 ft/s

(b) Test section velocity of 150 ft/s

Figure 3.13: Boundary layer profiles over MTF insert

The preceding analysis assumes that the noise due to the boundary layer is incoherent, which is an assumption made by multiple researchers. Unless there is separation in the flow with well-defined instability waves, this assumption is true as the random small-scale turbulence in the boundary layer by its very nature is uncorrelated. The sonic sensor in the present facility is located in the unseparated boundary layer.

3.2.2 Small Open-jet Facility

The small open-jet facility at GTRI is an open-jet wind tunnel with a maximum test section Mach of 0.48 and an eight-inch diameter nozzle at the test section. The wind tunnel is connected to a centrifugal fan to create the necessary back pressure to achieve the desired speed. The centrifugal fan has a variable frequency drive for fine tuning of the velocity. The layout of GTRI's open-jet facility is shown in Figure 3.14.

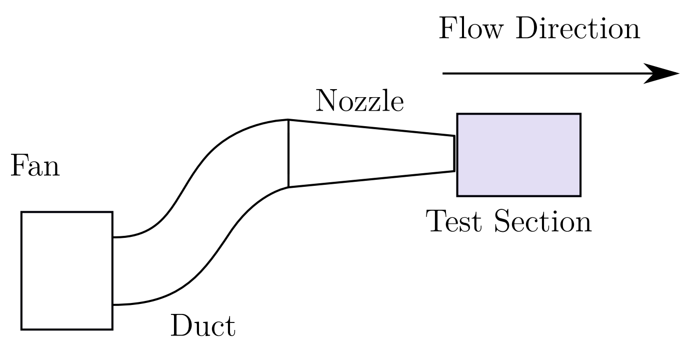

Figure 3.14: Small open-jet facility layout

The data acquisition system and test equipment used in this investigation are described in the following section.

3.3 Data Acquisition, Test Equipment, and Analysis

3.3.1 Low-Speed Testing

Acoustic sources producing a range of acoustic signals are tested at the outset of the program. For these tests, the microphone signal is acquired with a Measurement

Computing USB – 2020 DAq board capable of simultaneous measurements at 10 million samples per second and then transferred to the computer equipped with LabView. The receiver signal is sent through a PCB signal conditioner before continuing to the DAq. A bandpass filter is applied to the data, but the allowed frequency band depends on the frequency content of the signal being sent. The high sample rate is used to capture as much of the frequency content as possible and maintain an accurate estimated time delay.

The acoustic source is generated a few different ways. Initially, the signal is constrained to the audible range of the frequency spectrum to allow for variations in signal types to test. The signal for the audible tests is generated with an Agilent function generator. This is then sent to a BMS compression driver through a Behringer EP2000 amplifier, and attached to an inverse conical horn to create a point source. This creates a powerful point source, but also increases the frequency content in the signal due to the non-linearities at the exit of the point source as shown in Salikuddin et al. [57] This setup reduces the ability to use the electronic signal as the reference for the cross-correlation due to the fact that the non-linearities produce a signal at the exit that is not exactly the same as the original electronic signal. Also, the time of propagation through the inverse conical horn is temperature dependent and may not be calibrated out for a realizable system. This requires the reference signal to be collected right at the point source exit, upstream of the receivers.

3.3.2 Phased Array Testing

As described below in Chapter 5, to increase the signal-to-noise ratio, a point sound source used for low-velocity tests is replaced by an array of sources (referred to here as a “phased array”) that are mounted upstream of the microphones and their phases are adjusted to provide a steerable and more powerful acoustic beam. The phased array is constructed with six Murata ultrasonic transducers in a line. These transducers have a specific operating frequency, and do not have a good frequency response outside of that frequency. The phased array is controlled by a Java software, circuit board, and micro-controller (Arduino) developed by Marzo, et al. [58]. Since the signal is a pure tone, the sampling frequency can be reduced to something above the Nyquist frequency. For this testing, a NI USB-6366 data acquisition board is used with the sampling rate is 500,000 Samples/sec. This is well above the Nyquist frequency for the 40 kHz ultrasonic transducers. Four PCB 130B40 microphones are used for the reference receiver and signal receivers. The microphone grids were removed to increase their performance at higher frequencies. The same PCB signal conditioner used in the low-speed tests is used in these tests to transfer the microphone signal to the data acquisition system. The data for each run is collected over ten seconds.

The next chapter outlines the validation of the technical approach by analyzing the concept at low speeds. The focus of this validation is developing accurate time delay estimation of the signal travelling from the sound source to a given microphone, which is central to accurately determining the unknown flow parameters of the equations developed above. Various source signals were considered for the validation studies; therefore the exact generation of the acoustic source will be discussed in the following chapters.

CHAPTER 4
CONCEPT VALIDATION STUDIES

4.1 Introduction

The accurate determination of the flow properties hinges on the accurate estimation of the time delay of the signal. Without a consistent and accurate time delay estimation, the flow properties become impossible to decipher. There are many methods of time delay estimation, but one of the industry standards is cross-correlation, which is discussed in this chapter. As will be shown later, cross-correlation works better if unique features of a given reference signal can be pinpointed over the background noise. The Signal-to-Noise Ratio (SNR) plays a large part in the accuracy of the time delay as well. The next section provides an overview of cross-correlation technique, which is followed by an exploration of various signal types to generate the most easily discernible time delay. This is followed by a computational analysis of the sonic sensor, and then some experimental validation studies at low speed.

4.2 Cross-Correlation

Cross-correlation is the comparison of two time series data to determine how well the signals match and at what point in time the best match occurs, and has been used for data analysis since its conception in the late 1930s [3]. The scientific community started using statistical methods for a range of applications in mechanical engineering, aerospace engineering, medical science, biochemistry, and biotechnology fields with increased fervor with the advent of the modern computer and the increase in computing power . By the late 1970s and 1980s, cross-correlation methods were used in flow meters, mainly for measuring the flow through pipes for applications in the mechanical and nuclear engineering fields. For jet acoustic applications, Ahuja, et al. [35] had success using cross-correlation techniques to determine the acoustic path through a jet shear layer.

A random process cannot be described mathematically. In the data analysis of random data sets, it is sometimes beneficial to determine the similarity of a known signal and a version of the signal after a time delay, τ. This is typically determined using auto-correlation, which is given by:

$$R_{xx}(\tau) = \lim_{T \to \infty} \frac{1}{T} \int_0^T x(t)x(t+\tau)dt \tag{4.1}$$

Equation 4.1 is essentially the comparison of a random data set with itself after a given time, τ. One way of looking at auto-correlation is to consider a movie for which each frame is unique. If a single frame is taken from the film, and the movie is played over that single frame, as the movie is played, the overlay of the images will make it difficult to see the details of the movie. As the film gets closer to the point where the frame was taken, the details of the image will start to emerge until both images line up perfectly. From that point on, it will be more difficult to view the details of the images for the rest of the movie. The point of perfect alignment is considered to be $\tau = 0$. This is similar to the way the auto-correlation function deals with the similarity of a random process. For a purely random process, e.g. a white noise signal, the auto-correlation will produce a sharp peak at $\tau = 0$ showing the strong similarity at τ and a rapid decline in the correlation function at $\tau > 0$. A periodic data set will produce an auto-correlation with the same period as the input signal. For example, the auto-correlation of a sine wave will produce a sine wave due to the periodic nature of the signal.

Cross-correlation is similar to auto-correlation, but cross-correlation determines the similarity of two separate signals typically at some instance later in time. For white noise, the cross-correlation will produce a peak at $t = \tau$. The cross-correlation is given by:

$$R_{yx}\left(\tau\right) = \lim_{T \to \infty} \frac{1}{T} \int_{0}^{T} x(t)y(t-\tau)dt \tag{4.2}$$

Returning to the film analogy, the cross-correlation will determine location of the frame in the film with the reference point at the start of the movie. For more information on cross-correlation and/or auto-correlation, the reader can refer to [59] or any other text regarding random data analysis and processing.

Time delay estimation using cross-correlation hinges on two main things, SNR and frequency content of the reference signal. The SNR is linked to the magnitude of the peak whereas the frequency content determines the distinctness of the peak at the correct time delay. For example, if a broadband signal (with infinite frequency content) is used as a reference and the signal of interest has a high SNR, the cross-correlation is expected to have a well defined, sharp peak at the time delay as shown in Figure 4.1. Here, a broadband signal is generated and delayed by 0.0001606 seconds (SNR = +28 dB). There is a very sharp peak with a high magnitude at the prescribed time delay demonstrating the capability of the cross-correlation to estimate the time delay between the reference signal and the signal of interest. The parts of the signal that are not correlated are indicated by a normalized correlation coefficient near zero in magnitude.

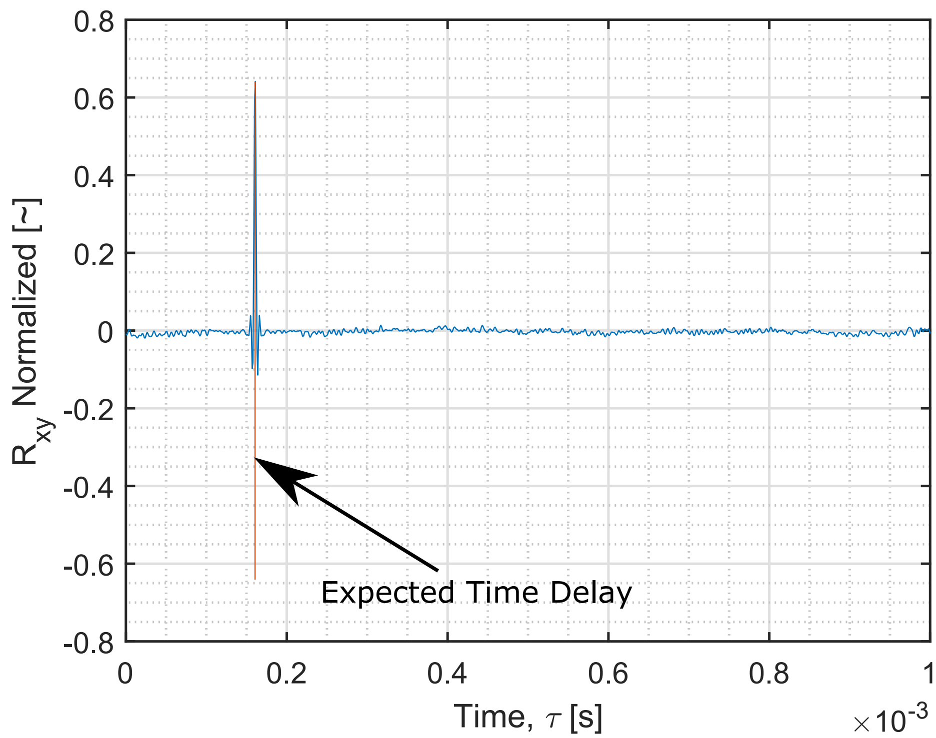

Figure 4.1: Cross-correlation of broadband signal displaying well-defined peak at the prescribed time delay of 0.0001606 seconds.

This is the ideal solution for estimating the time delay. Assuming there is no noise, the broadband signal produces the high magnitude, sharp peak at the time delay, and can be easily selected in a simple algorithm to pull the maximum correlation coefficient from the cross-correlation. The main issue of the using broadband signal for the sonic sensor is the practical application. The compression driver (speaker) has a set limit on the amount of electrical energy that can be converted to acoustic energy. For the broadband signal, this total energy is smeared over the entire frequency spectrum resulting in a lower output over all the frequencies. Depending on the amount of expected background noise, the broadband signal may be masked by the noise rendering the cross-correlation ineffective at determining the time delay. If the background noise masks the signal the cross-correlation would result in a correlation coefficient near zero for the entire sample time. It is basically trying to correlate uncorrelated noise which would produce a useless result for estimating time delay. If all the converted energy of compression driver is directed into one frequency (i.e. a single tone) the SNR would increase and produce a useful correlation result. Filtering and other signal processing techniques could be used to further increase the SNR and achieve an acceptable SNR for estimating time delay. Figure 4.2 shows the normalized cross-correlation as a function of the time delay for a 40 kHz tone with the same prescribed time delay as the broadband signal, 0.0001606 seconds. The consequence of the tone signal is immediately apparent with the lack of definition of a single distinct peak. There are multiple peaks with the same or similar magnitude rendering the selection of the correct time delay nearly impossible without some general knowledge of the approximate time delay to aid in the selection of the correct peak.

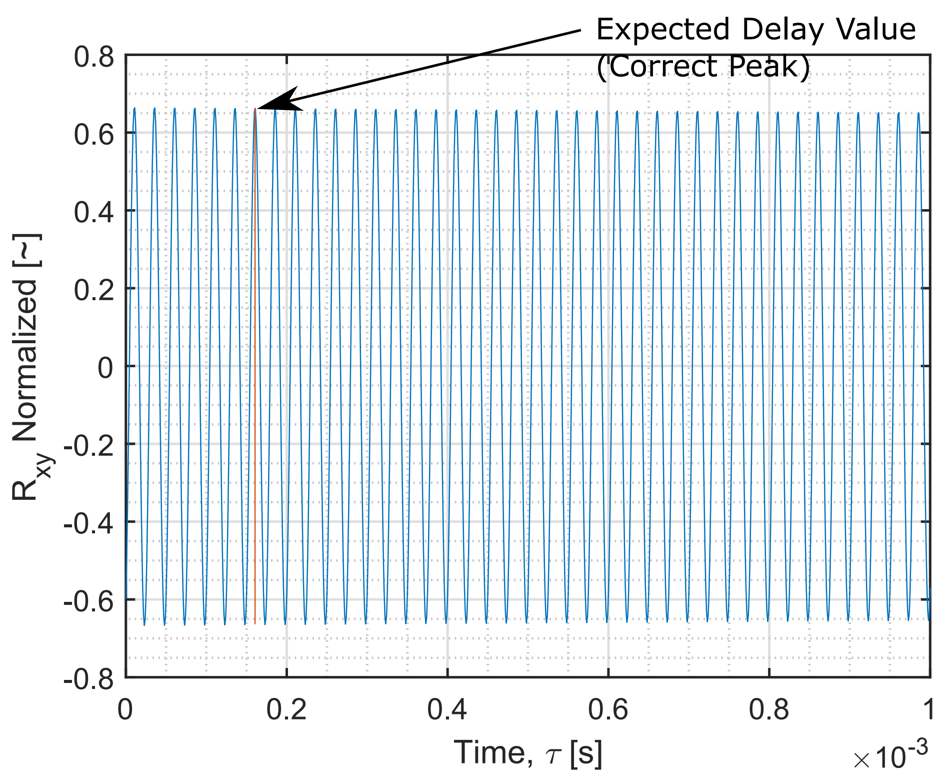

Figure 4.2: Cross-correlation of 40 kHz signal displaying the periodic nature in the result for a tone increasing the difficulty of selecting the correct time delay

While this demonstrates the maximum SNR available from a specific speaker, the frequency content or uniqueness of the signal suffers. A simple, yet effective way to increase the frequency content while maintaining the ability to maximize the output of the speaker is to use a burst as the reference signal. Four cycles of a 40 kHz signal is sent at 50 Hz to generate the burst signal. The duration of the gaps between successive bursts can be randomized to make a more desirable signal for correlation purposes, but that is not the focus of this work. As with the previous signals, the prescribed time delay is 0.0001606 seconds and the normalized cross-correlation as a function of the time delay is shown in Figure 4.3. The burst produces a strong peak at the correct time delay, but due to the cyclical nature of the tone, there are still some oscillations in the cross correlation that could cause some issues for a low SNR.

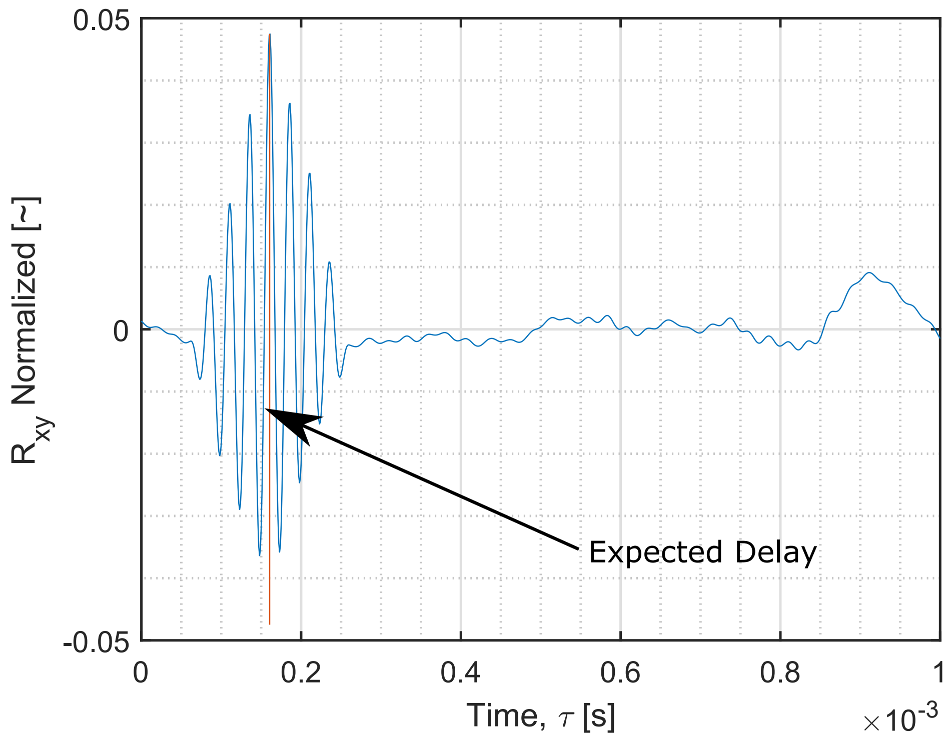

Figure 4.3: Cross-correlation of 40 kHz signal displaying the periodic nature in the result for a tone increasing the difficulty of selecting the correct time delay

Increasing the frequency content further, an ever increasing change in the frequency of the signal, or chirp, is analyzed as the reference signal. The chirp has a high frequency content and it allows the compression driver to put all the power into a single frequency for a short period of time, which would increase the SNR. The chirp analyzed starts at three kHz and increases to 48 kHz over 1 ms, which is in turn sent at every 0.02 seconds. The chirp signal is defined as:

$$x(t) = A \sin\left(2\pi t f(t)\right) \tag{4.3}$$

Here, A is defined as the amplitude, t is the time, and $f(t)$ is the frequency as a function of time. The chirp allows for a well defined peak for the cross-correlation similar to the broadband noise signal, but reduces some of the ambiguity in the peak location from the tone and burst signal as shown in Figure 4.4. This signal allows for the best of both worlds between the broadband signal and a tone. The signal has enough frequency content to produce a definitive peak at the correct time delay, but will also allow for the speaker to output a louder signal than the broadband signal, provided the chirp is within the frequency range of the speaker.

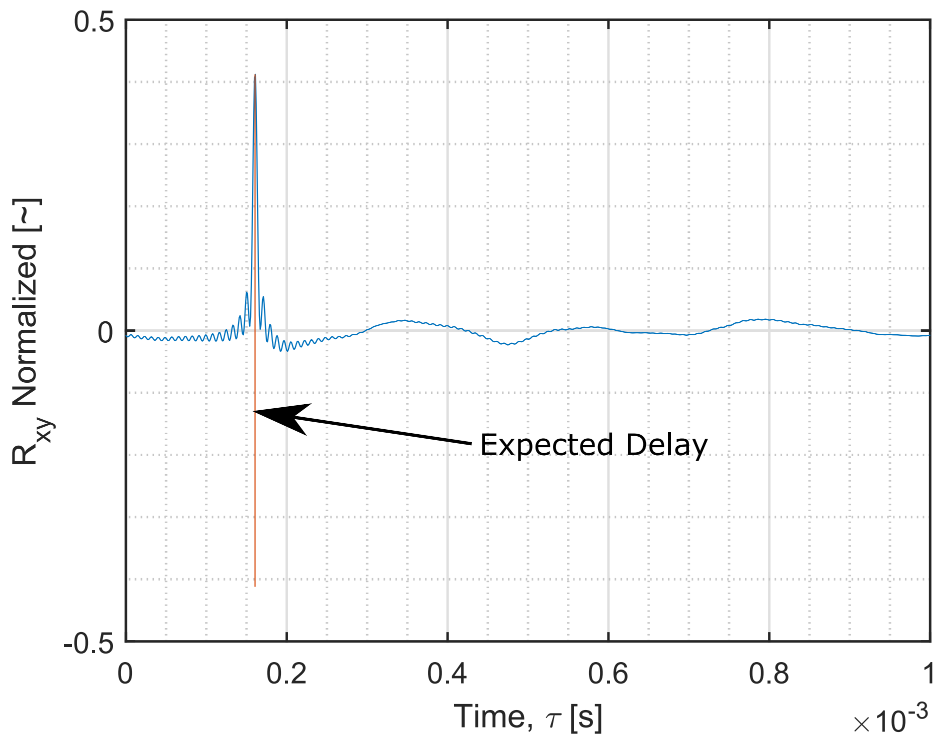

Figure 4.4: Cross-correlation of 40 kHz signal displaying the periodic nature in the result for a tone increasing the difficulty of selecting the correct time delay

As seen in the research and application of the cross-correlation method in open literature, the prediction of the change in time improves with an increase in the frequency content of the signal, but what may not necessarily be apparent is the fact that the cross-correlation peak improves with the sample size. Increasing the sample size effectively averages out the uncorrelated noise and returns a detectable peak even at very low SNR values. What happens here is that there are more points for the cross-correlation to compare, making the signal more detectable in through the noise. For a small sample size, the uncorrelated noise is not sufficiently averaged out, and has a significant impact on the results of the cross-correlation. This produces the cross-correlation of mostly uncorrelated noise, which produces no decipherable peak for the time delay. This limits the lowest SNR that is required in order for the acoustic data sensor to function properly for a given sample size. The SNR is given as a function of the acoustic pressure of the signal, P_{signal} and the acoustic pressure of the noise, P_{Noise}, by:

$$SNR = \frac{P_{signal}}{P_{Noise}} \tag{4.4}$$

In decibels, this is:

$$SNR_{dB} = 10 \log_{10} \left(\frac{P_{signal}}{P_{Noise}} \right) \tag{4.5}$$

Since cross-correlation first was used, it has been known that a reduction in the SNR reduces the normalized cross-correlation peak magnitude, which could increase the error of the cross-correlation method. There has even been an increasing amount of research into developing more accurate methods of increasing the SNR to acceptable levels for an accurate correlation. Hassab and Boucher [60, 61] attempted to apply an optimal time delay estimate based on the generalized cross-correlation of Knapp and Carter [62] in the presence of noise. Zhang and Abdulla [63] investigated the limits of SNR for accurate correlation, and made the argument that the reduction in sample time is analogous to decreasing SNR. As the sample time is reduced, the uncorrelated noise is no longer averaged out, and it is more difficult to discern the signal from the noise. Li et al. [64] also investigated other techniques for applying cross-correlation to low SNR environments. Even the work done by Otero et al.[34] required the SNR to be high enough to be able to precondition the signal before sending it through the cross-correlation analysis. Otero zeroed out everything between the bursts that were sent by the transceivers and was able to increase the SNR by minimizing the hydrodynamic noise and placing the receivers outside of the flow. This option is not available to the sonic sensor.

Figure 4.5 shows the impact of SNR on the cross-correlation of a burst signal over 0.05 second sample time with Figure 4.5a showing the cross-correlation with a SNR of

1.76 dB and Figure 4.5b showing the cross-correlation with a SNR of -18.25 dB. Both figures show the cross-correlation on the same normalized correlation coefficient on the y-axis to show the reduction in normalized correlation coefficient as the SNR is reduced. Figure 4.5b still shows a peak at the correct time delay, but the magnitude is significantly reduced. If the SNR is reduced further, the signal will be totally masked by the noise and no discernible peak will be in the correlation. It will be the trivial solution of the correlation of uncorrelated noise.

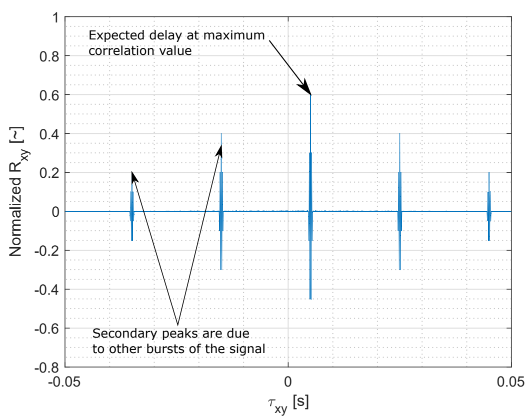

(a) SNR = +1.76 dB

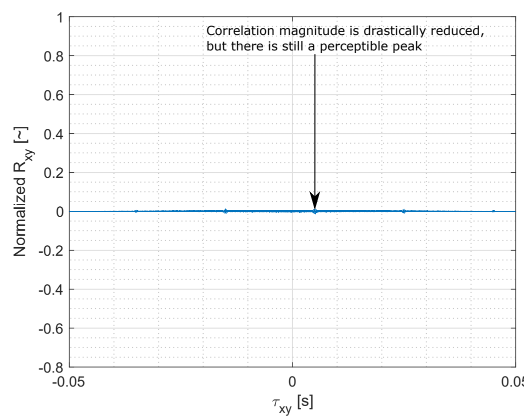

(b) SNR = -18.25 dB

Figure 4.5: SNR effects on magnitude of normalized cross-correlation coefficient for a burst signal

The next section takes the cross-correlation technique and applies it to the sonic sensor problem using a computational model.

4.3 Concept Validation via Simulation

A computational model is developed to model the problem with a simplified set of assumptions to test feasibility and limitations of the system. For this analytical model, a Matlab [65] script is developed to try and capture all the effects that would be in the physical system. A clean signal (broadband, tone, burst, and chirp) is generated electronically at a rate of $5e^8$ samples per second for one second. The high sample rate is used to accurately shift the signal by the desired time. In the real world, the time shift is not subject to sampling rates or how often data is recorded for the signal. Ideally, the sampling rate would be infinite for the generated signal, but that is not practical because the computer systems would run out of memory. A sample rate of $5e^8$ samples per second is chosen such that it is sufficiently high to simulate the signal traveling through air and allow for a study on the impacts of lower sampling rates on the calculated velocity. The lower sampling rates simulate the sampling rate of the data acquisition system collecting the receiver data. The clean signal is then shifted by a time delay, t, which is a function of the specified angle of attack, α, and a flow velocity, U as given in Equation 4.6 and Equation 4.7 for standard sea level conditions.

$$t = \frac{L_i}{V_{signal}} \tag{4.6}$$

Where L, is the length to the ith receiver and V_{signal} is the signal velocity given by:

$$V_{signal} = c\frac{\sin\left(\pi - \sin^{-1}\left(\frac{U}{c}\sin\left(\theta_i - \alpha\right)\right) - \left(\theta_i - \alpha\right)\right)}{\sin\left(\theta_i - \alpha\right)} \tag{4.7}$$

All terms in the above equation are defined in Chapter 3, Figure 3.2. The receiver geometric parameters for the analytic model are given in Table 4.1.

Table 4.1: Receiver geometry used in computational model

Reciever	L [in]	θ [deg]
R1	11.54	-37
R2	10.71	21
R3	8.98	50

The shifted signal is then decimated to the desired sample rate to simulate the collection of the data by a data acquisition system. Hydrodynamic noise is added to the signal to simulate the impact of the flow over the receivers. The hydrodynamic noise is measured in GTRI's small open-jet facility at the maximum Mach achievable, and is assumed to be representative of the noise environment present in the physical system. The delayed signal with noise is cross-correlated with the clean signal to determine the estimated time delay using the Matlab cross-correlation function. A second order polynomial fit is implemented at the peak of the cross-correlation to reduce the error in the exact time of flight due to the sampling rate. For example, if the exact time delay was 11.75 seconds, and the data is recorded every two seconds, there would be an error introduced by the sampling rate and there would be a peak in the cross-correlation at 12 seconds. This example brings up another point. The time discritization of the signal (i.e. the time step of the sampling rate) must be orders of magnitude less than the delay being measured. In the above example, a sampling rate of at least 100 samples/sec could capture the time delay accurately. The addition of the polynomial fit in the region of the peak in the cross-correlation improves the accuracy of the estimated time delay and allows for a small reduction in the sampling rate with minimal impact. To verify the theoretical formulation, a broadband signal is used so there is no ambiguity in the estimated time delay.

With the sampling rate discussion in mind, the impact of the sampling rate on the calculated velocity of the sonic sensor is studied. For this study, the SNR is kept at +28 dB to minimize the impact on the calculated velocity. This is an assumed condition, and it is noted that the hydrodynamic noise will increase as the flow speed is increased, but this is not the focus of the sampling rate study. The angle of attack is set to zero, and the sample time is set to 0.05 seconds. The sampling rate is varied to determine the minimum sampling rate to produce accurate results. Figure 4.6 shows the calculated velocity by the sonic sensor method in terms of the input velocity for various sampling rates. For the modeled geometry, the minimum sampling rate is around $1e^6$ samples per second. Sampling rates less than $1e^6$ samples per second introduce large errors in the calculated parameters due to the time discretization step of the sample rate being a greater than what could be overcome by the polynomial fit. The smaller sampling rates also display the sensitivity of the sonic sensor methodology for accurate time delay measurements. The estimated time delay could be slightly off and produce extreme errors when it comes to the final calculation of the velocity. Since all of the flow parameters are linked to the velocity, and time delay by extension, there are similar errors in the other calculated parameters at the lower sampling rates. For sampling rates at, or above $1e^6$ samples per second, the calculated velocity has small errors when compared to the input velocity. This result is shown by the data collapsing to a single line and all the symbols falling on top of each other which look like a solid triangle in the following figure.

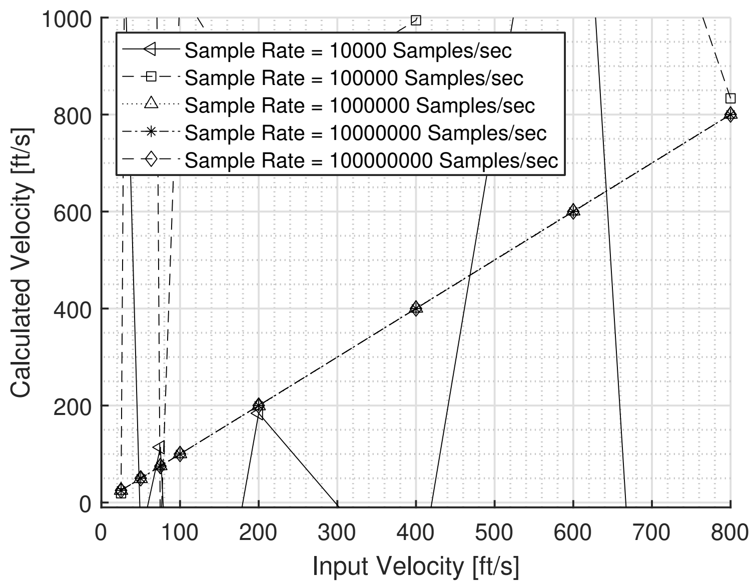

Figure 4.6: Sample rate comparison for the velocity calculation using a broadband source signal

The previous study shows that the minimum sampling rate for accurate velocity calculation is one million samples per second for the current geometry. Increasing the distance between source and receiver may allow a lower sampling rate due to the increase in time delay between the source and receiver. For example, if the source and receiver were separated such that a signal sent from the source takes 100 seconds to reach the receiver the sampling rate would not have to be extremely high to capture the time delay accurately. In other words, the estimated time delay would not have to be accurate to 0.00001 seconds to capture the behavior. This is dependent on the desired smallest change in time delay to be measured by the system. For the subsequent studies, one million samples per second is used as the sampling rate to isolate the angle of attack and SNR effects.

Since there is a small error in the velocity, meaning the time delay is accurately estimated, it is expected that there is a small error in the calculated angle of attack through the sonic sensor methodology. This is shown in Figure 4.7, where the calculated angle of attack is presented as a function of prescribed velocity at various prescribed angles of attack, denoted in the legend as Alpha. The calculated angle of attack matches the input angle of attack quite well for input velocities over 100 ft/s. There is a slight variation at the lower speeds (below 100 ft/s), this is due to the sampling rate error showing up in the angle of attack calculation. The reason for the slight variation in calculated angle of attack goes back to the time discritization discussion. At the low speeds, the changes in the time delay are small compared to the no-flow case. This means that the changes due to angle of attack variation are smaller still. The polynomial fit at the peak of the cross-correlation does a good job of capturing the correct time delay, but at the lower speeds the fit can only do so much. The accuracy of the calculated angle of attack could be improved with a higher sampling rate, but this verifies that the methodology can recover the velocity and angle of attack to an acceptable degree of accuracy subject to the SNR and sampling rate limits.

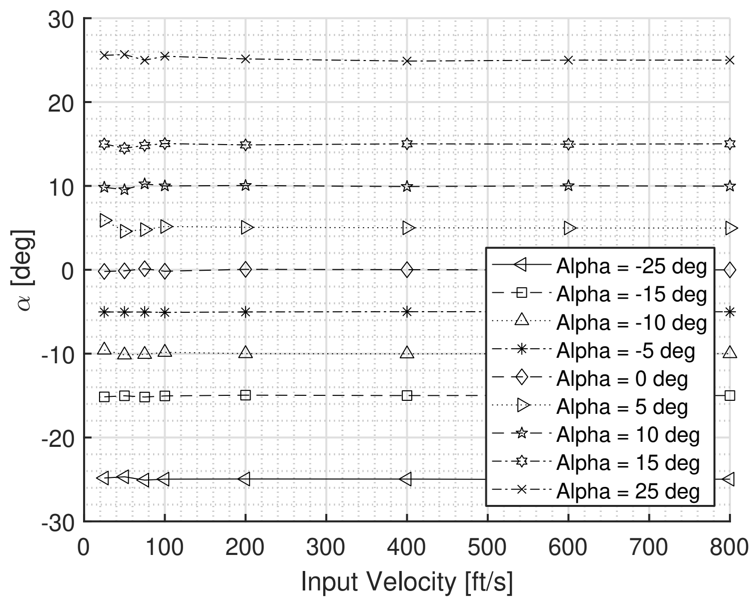

Figure 4.7: Calculated angle of attack as a function of input velocity for a sampling rate of one million samples per second utilizing a broadband source signal

The SNR will also impact the ability of the cross-correlation to detect an accurate time delay. If the background noise masks the signal, it may be difficult for the cross-correlation to extract the reference signal from the noise and produce a definitive peak for the time delay estimation. For most cases, the SNR is not an issue for the cross-correlation because the sample time can be increased, effectively averaging out the uncorrelated background noise. For aircraft applications, this option is not always available, especially for flight critical measurements. For this study, the SNR is varied in the computational model from +25 dB and -60 dB. The sample rate is kept at one million samples per second and the angle of attack is set to zero. Figure 4.8 shows the effects on the velocity calculation as the SNR is reduced while holding the sample time constant at 0.05 seconds. The calculated velocity matches the input velocity for SNRs greater than -22 dB, which shows the cross-correlation is resilient to low SNR but only up to a point.

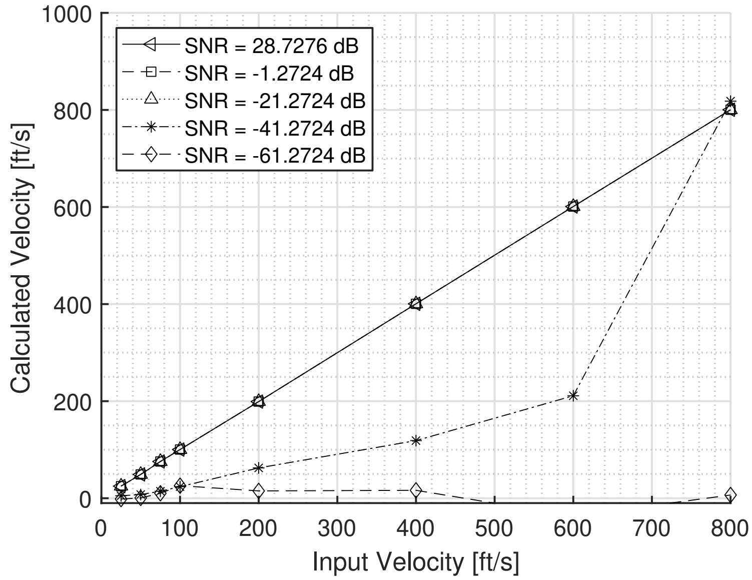

Figure 4.8: Comparison of calculated velocity and input velocity for various SNRs with a sampling rate of one million samples per second

From this analysis, it leads to the conclusion that the SNR must be greater than -22 dB for the cross-correlation to be effective for a sample time of 0.05 seconds. This result can be a little misleading, the Matlab generated broadband noise is for the entire spectrum of frequencies, while the flow noise is limited to the frequency response of the microphones used in collecting the data. The frequency response of the microphones drops off at higher frequencies allowing for a higher SNR at those higher frequencies. The cross-correlation of the simulated signal is not bound by the microphone frequency response and takes advantage of the higher SNR at the higher frequencies to produce a strong correlation peak. Therefore, the minimum SNR of -22 dB maybe optimistic and higher SNR may be necessary for an actual system. Simulation of behavior can only go so far to validate the concept, the next section discusses experimental validation of the sonic sensor concept in a low-speed wind tunnel.

4.4 Concept Validation via Experiments

The computational model is verified by placing the receivers and source into the Model Test Facility (MTF) at Georgia Tech Research Institute (GTRI). The source signal is generated by an Agilent function generator and passed to a BMS compression driver through a Carvin 1500 amplifier. The receiver geometry is detailed in Table 4.2. The receivers are PCB 130B40 Electret surface microphones, and the data from the microphones is collected by two Measurement Computing USB – 2020 Data Acquisition system linked together, both with a sampling rate of 10 million samples per second.

Table 4.2: Receiver geometry used in experiments

Reciever	L [in]	θ [deg]
R1	5.966	45.32
R2	5.813	-29.45
R3	6.064	-62.13

A pitot-static tube is placed in the test section as a truth source for the speed of the airflow. The pitot-static tube is also equipped with a thermo-couple on the end to measure the total temperature in the test section. A picture of the test setup is repeated in Figure 4.9 for reference. A humidity sensor is also placed in the test section to measure the amount of moisture in the air, which will have an impact on the calculated temperature as will be discuss later. For the interested reader, an uncertainty analysis for the measured test section parameters is included in the Appendix of this work.

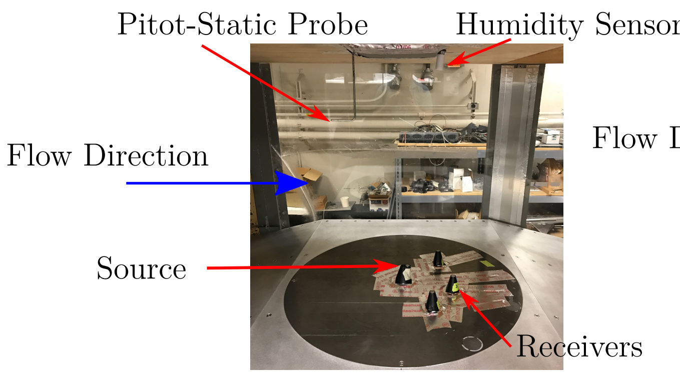

(a) Test section

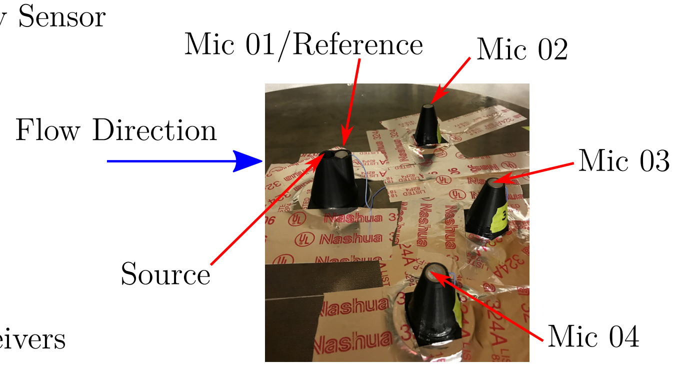

(b) Model Setup

Figure 4.9: MTF test setup

For these tests, a chirp is used as the source signal. Each chirp is sent over one millisecond every 0.02 seconds. A BMS high-frequency compression driver is used in the generation of the chirp to maintain adequate frequency content for the higher frequencies. A second Agilent frequency generator is used to trigger the chirp every 0.02 seconds.

Due to physical limitations and initial assumptions, there are a few correction factors that must be applied to improve accuracy of the sonic sensor and will be discussed in the next sections.

4.4.1 Distance Correction

In the development of the theory of the sonic sensor, it is assumed that the source and reference for the cross-correlation are measured at the same point. This assumes that the mechanism that generates the acoustic signal (typically a diaphragm) is on the same plane as the receivers. The size of the compression drivers made this assumption impractical during the experimental work, and the acoustic signal required an inverse conical horn to produce a point source in the plane of the receiver diaphragms as shown in Figure 4.10. For more information on an inverse conical horn, see Ahuja's work in [66] where it was shown that the inverse conical horn used in the present study produced a monopole source.

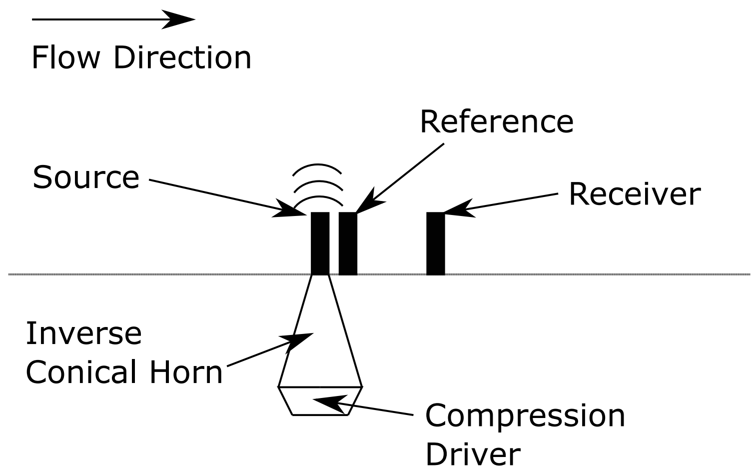

Figure 4.10: Test setup with inverse conical horn

The source and reference will have some offset due to physical limitations. The electronic reference could not be used for these tests, because the diaphragm of the speaker is not directly in the flow field and there would be an additional delay in the cross-correlation for the signal to go from the diaphragm to the exit of the inverse conical horn. As the sound produced at the acoustic driver passes through the inverse conical horn its intensity increases and the sound propagation becomes non-linear. This effect is further augmented as the sound passes through a narrow tube. Thus the sound exiting from the point source may have little resemblance to the a electronic reference signal. The reader is asked to refer to Salikuddin and Ahuja's work in [57] for more information on this effect of the inverse conical horn and high amplitude acoustic signals. Therefore, a microphone is placed as close as possible to the exit of the inverse conical horn and acts as a reference for cross-correlation. For the determination of the acoustic centers of the source and receivers, the static conditions are used to calculate the distance between the acoustic centers via cross-correlation technique. With the temperature known for static conditions, the speed of sound can be determined. This calculated value is then coupled with the estimated time delay from the cross-correlation, the actual distance between the acoustic centers are determined. The spherical nature of the sound propagating means that the distance measured by this method is shown in Figure 4.11 as the distance between the receiver and the dashed circle that represents the psuedo-location of the reference under static conditions. Technically, the reference could be on the other side of the source at the same distance, and the estimated time delay would be the same value because the acoustic signal propagates in all directions at the speed of sound.

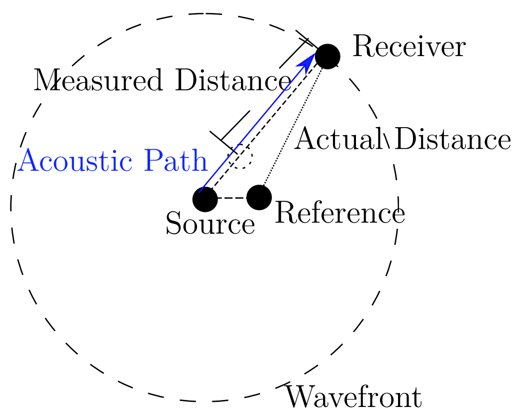

Figure 4.11: Distance correction definition

As the flow is increased, the estimated time delay and distance no longer match to determine the correct flow velocity. The correction on time delay is a function of the flow velocity and the angle of attack of the flow. The uncorrected data is used as a starting point for an iterative solution to determine exact correction factor. Convergence is fairly rapid for this, and the computational cost would be minimal. A correction for humidity effects is discussed in the next section.

4.4.2 Humidity Correction

Before the flow parameters can be accurately calculated from the estimated time delay, the humidity in the air has to be accounted for. Typically, the assumption for the ratio of specific heats, γ, of 1.4 holds for most engineering applications at relatively low temperatures ($<$ 1400 deg R), but this assumes that the air is dry, i.e., Relative Humidity (RH) of 0%. Humidity adds in vaporized water into air and must be accounted for in the speed of sound calculation. The speed of sound in water is faster than in air, so the presence of water vapor increases the speed of sound for the same temperature. When determining the exact distance between the source and receiver, the time delay was used along with the temperature and data is collected under no flow conditions. With the temperature and time of flight known, the speed of sound can be determined as well as the distance between the acoustic centers of the source and receivers. The speed of sound is determined from:

$$c = \sqrt{\gamma R T} \tag{4.8}$$

Initially, the ratio of specific heats for air is assumed to be 1.4 for air as is the case for most flow conditions, but this is not necessarily true for the test conditions of that day. The tests were performed indoors with a RH value of around 50%. Increasing the amount of water vapor in air, increases the speed at which a sound wave propagates through that medium (mixture of air and water vapor). Incorporating the relative humidity, the speed of sound can be determined by Equation 4.9 [67].

$$c = \sqrt{\frac{7+h}{5+h}\frac{R}{29-11h}T} \tag{4.9}$$

Where the water vapor factor, h, as a function of the relative humidity, RH, the

Temperature, T, and the reference pressure, p_{ref} is given by:

$$h = \frac{0.1RHe\left(T\right)}{p_{ref}} \tag{4.10}$$

The Buck equation for the vapor pressure of water, $e(T)$, is shown in Equation 4.11.

$$e\left(T\right) = 0.61121 \exp\left(\left(18.678 - \frac{T}{234.5}\right)\frac{T}{257.15 + T}\right) \tag{4.11}$$

Figure 4.12, taken from [67], shows the increase in speed of sound due to humidity and temperature effects according to the above equations.

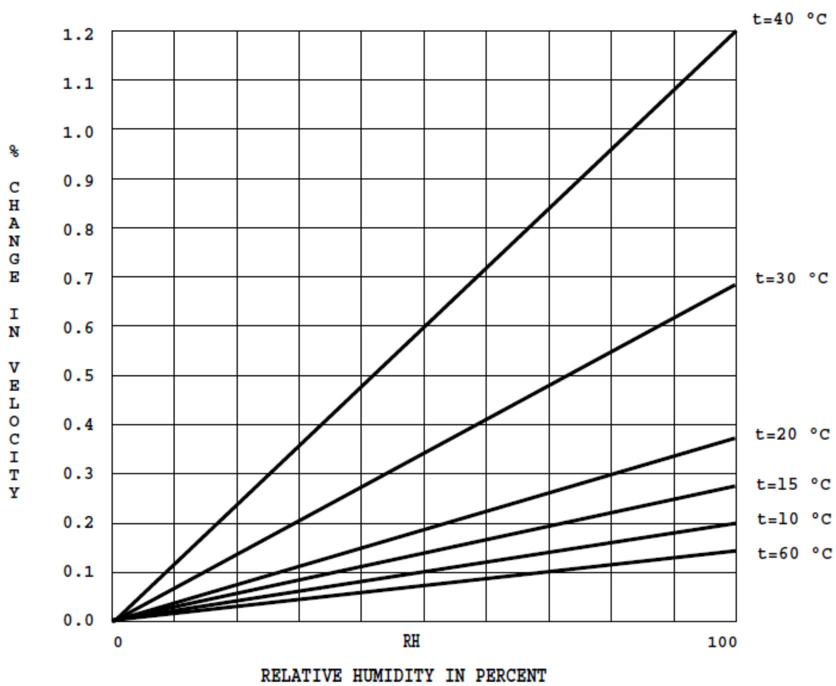

Figure 4.12: Effect of humidity on the speed of sound in air [67]

This is an important result. This shows that at 50% RH at 20 deg C (527.67 deg R), the speed of sound can increase by about 0.2% or about 2.2 ft/s. This does not seem like a lot, but an error of 1 ft/s in the speed of sound corresponds to an error of approximately 1 deg R in the calculated temperature when using Equation 4.8. This coupled with the constant γ assumption to determine the distance between the acoustic centers of the source and receivers would compound the error and would produce the errors seen in the initial results. The humidity and distance corrections are applied to experimental data in the next section.

4.4.3 Flow Parameter Comparison

The methodology is experimentally validated in GTRI's MTF wind tunnel. With the model insert and microphones placed in GTRI's MTF test section, the velocity in the test section is varied up to 150 ft/s. The angle of attack of the model is zero for the velocity comparison tests. A high pass filter is used with the low cutoff frequency at 6 kHz to remove most of the hydrodynamic noise in the tunnel and focus on the region where the flow noise is lowest. The cross-correlation is performed over 0.05 sec intervals of the filtered data, and the humidity and distance corrections are applied. Figure 4.13 shows the comparison between the sonic sensor calculated velocity and the pitot-static measured velocity (labeled as Test Section in the figure). The errors in the pitot-static tube are given in the plot to show how close the measurements are. There are a few conditions where the test section velocity does not match the sonic sensor velocity, but these could be slight variations in the flow that are detected in the cross-correlation, and not the pressure transducers. The figure shows that the distance correction has more of an effect on the calculated velocity than the humidity effect does, but overall the pitot-static measurement and the sonic sensor align well with the velocity.

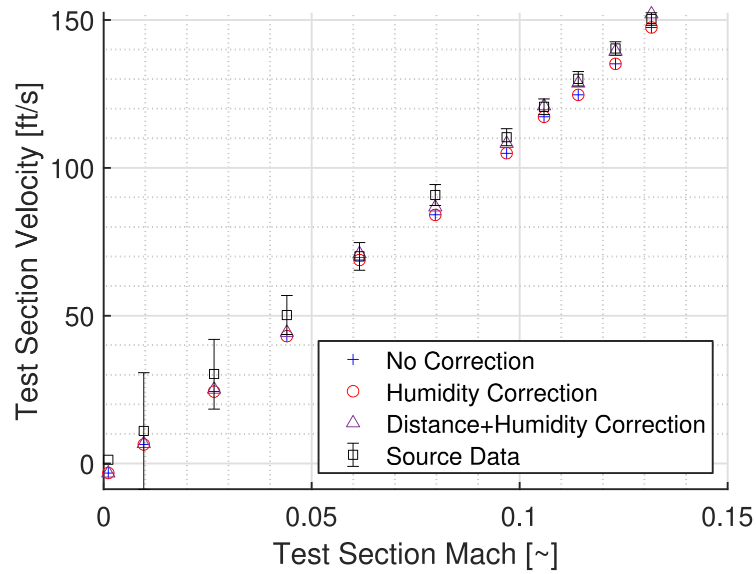

Figure 4.13: Comparison of calculated velocity with test section velocity while incorporating distance and humidity corrections

Having verified the flow velocity, the temperature is now considered. The static temperature is determined from the speed of sound, and then converted into the total temperature via the isentropic relationships of air. The results of the total temperature analysis are given in Figure 4.14, where the total temperature, T_t, is given as a function of the test section Mach number. There is quite a large error at the lower speeds, which maybe due to the time discretization of the sampling rate and trying to capture the small changes in the estimated time delay. It is important to note that a small change in the speed of sound, 1 ft/s, is equivalent to 1 deg R change in the static temperature. That is roughly a 1% change in the speed of sound would cause a change in temperature of about 10 deg R. At the higher speeds tested here, both the sonic sensor and the test section temperature probe are quite close. The humidity correction makes a large difference in reducing the difference between the sonic sensor data and the temperature probe.

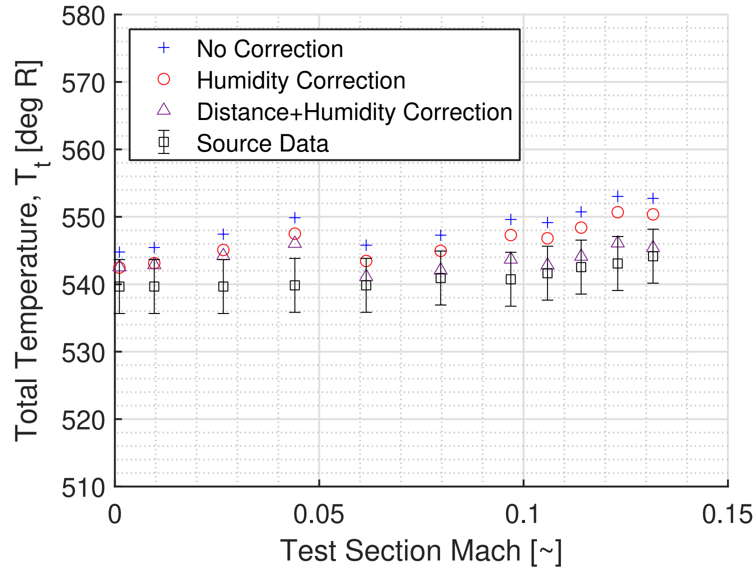

Figure 4.14: Comparison of calculated total temperature with measured total temperature while incorporating distance and humidity corrections

The validation of the temperature and velocity shows the methodology works well for low speed and zero angle of attack. The angle of attack calculation is addressed next to further verify the sonic sensor methodology. The angle of attack is set by the model turntable, which can be rotated in five degree increments. A burst is used as the source signal for these tests to show the ability to handle multiple types of source signals and still perform well. Two cycles of a 4 kHz tone is sent through the compression driver at a frequency of 50 Hz. As discussed earlier, the non-linearities at the exit of the inverse conical horn allow multiple higher frequencies to be present in the source signal. Figure 4.15 shows the experimental validation of the angle of attack measurements. As expected the angle of attack is harder for the sonic sensor to determine. This is based on the small changes in the estimated time of flight being within the noise for the sampling rate and subsequent polynomial approximation of the peak of the cross-correlation. As the velocity is increased, the angle of attack is easier to measure because the time discretization from the sampling rate is less of a percentage of the actual time delay.

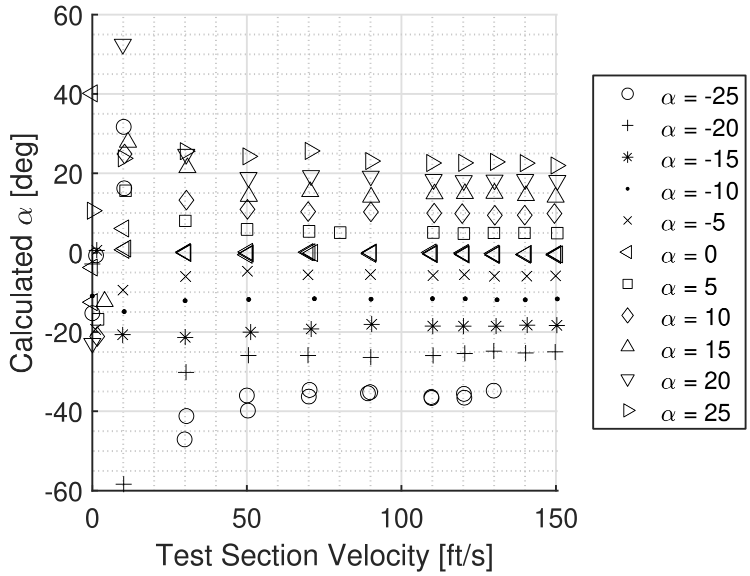

Figure 4.15: Comparison of calculated angle of attack as a function of speed

It should be noted that at high angles of attack and speeds below 30 ft/s, the method seems to break down and produce significant errors. The breakdown at speeds below 30 ft/s are due to the time discretization induced error as discussed earlier. The breakdown at high angles of attack is due to the flow separation off of the source support structure, and its influence on the downstream flow. The cylindrical nature of the vortex shed off a cylinder of finite distance is known, and has been analyzed by [68] and [69]. This wake spreads out as the vortex structure propagates down stream. The sonic sensor error in calculated angle of attack increases below -10 deg and above +20 deg. The reason for this becomes apparent when the geometry of the setup is considered and the vortex structure shed from the source support structure. From Adaramola et al. [68], the turbulent vortex structure shed from a finite cylinder expands ± 20 deg downstream was determined from CFD results as seen in Figure 4.16. The wake behind the cylinder is a region of reduced flow speed when compared to the free stream flow velocity, which produced non-uniformity in the flow field. As mentioned previously, the non-uniformity in the measurement volume effectively measures an average velocity and not the free-stream velocity. If two acoustic paths are not affected by the support structure wake and the third acoustic path is affected by the support structure wake, the derivation assumptions breakdown and will lead to erroneous results.

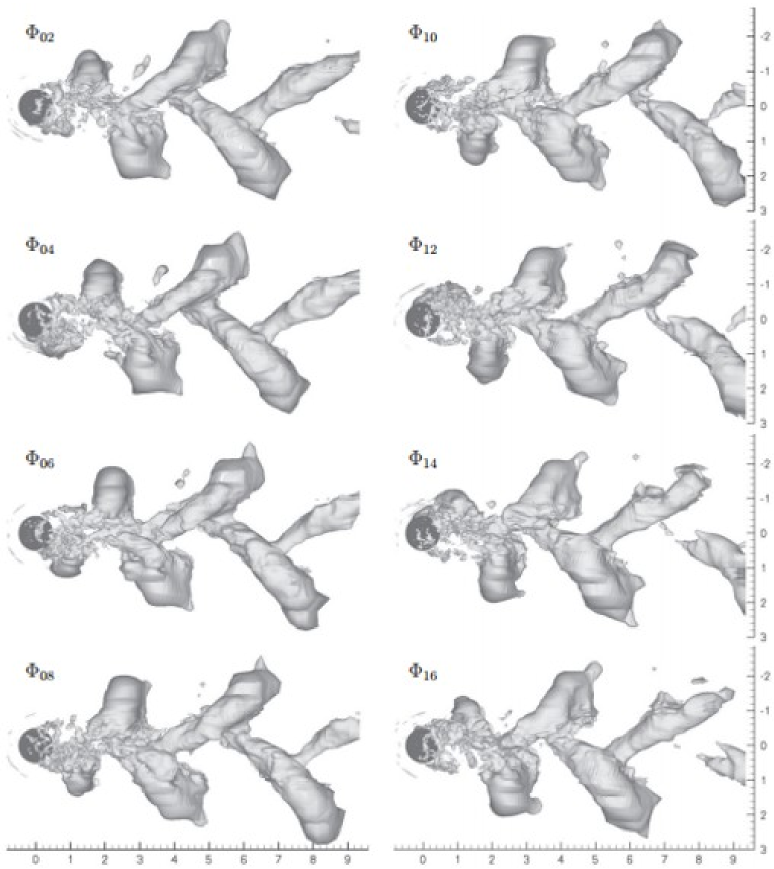

Figure 4.16: CFD results for a wake behind a finite cylinder [69]

With this in mind, and that Mic 3 is only 29 deg offset from the source structure, the vortex structure should start impacting the calculated angle of attack at around -10 deg as seen by the experimental result. This is based on the wake expansion in the CFD results and the receiver geometry. On the positive angle of attack side, the angular spacing is 45 deg to Mic 1, so the impact on the angle of attack calculation would be more apparent at angles of attack of approximately 25 deg. This is also shown in the experimental results.

4.5 Summary Remarks

From the above results, this method for measuring the flow properties based on the acoustic propagation of a known signal works well. This is provided that the SNR is high enough to maintain an accurate determination of the signal time delay between receivers. The incorporation of a humidity correction is necessary for the accurate determination of the flow temperatures. Most of the time, the ratio of specific heats for air is assumed to be 1.4, and this is normally a very good assumption which introduces minimal error in the final result. The same can be said here, but, depending on the final desired accuracy of the calculated parameters, this may not be a valid assumption. The distance correction applied is also an important result. The calibration process for these acoustic based sensors can happen in no-flow conditions as the calibration process is just determining the acoustic centers of the receivers, accounting for variations due to the manufacturing process. The angle of attack measurements match well with the expected results up to a certain point. At this point separation effects over the upstream supports is significantly impacting the flow between the source and the receiver, and the time delay is no longer in the free-stream flow. This will have an effect on the estimated time delay by the cross-correlation, which introduces errors in the calculated angle of attack. These errors can be minimized through aerodynamic shaping of the support structure and having an accurate angle of attack range on this sensor, similar to that on current angle of attack sensors on the market. As the flow speed was increased, the SNR decreased to a point where the source signal was no longer detectable over the hydrodynamic noise of the flow. This, coupled with short sample times introduced large errors in the calculated parameters. As stated earlier, low SNR is not typically an issue as the sample time is increased because the uncorrelated hydrodynamic noise is averaged out leaving only the signal. In the next chapter, an investigation into utilizing phased arrays to increase the SNR while maintaining a 50 ms sampling rate is discussed.

CHAPTER 5
SONIC SENSOR FOR HIGH-SPEED AIRCRAFT UTILIZING PHASED ARRAY TECHNOLOGY

5.1 Introduction

As shown in the previous chapter, the sonic sensor utilizing cross-correlation methodology is highly dependent on the SNR and sampling rate or the rate at which changes are read by the receivers. The sampling rate can only be increased to a certain level due to hardware limitations and computational resources. Once the sampling rate limit is reached, the distance between source and receiver must be increased to get the level of fidelity required. Increasing this distance will reduce the SNR due to some of the acoustic signal being damped out by atmospheric effects. At some point, a stronger signal must be used. This chapter will outline a method of increasing the acoustic power of the source to achieve an adequate SNR to produce consistent time delay estimation using cross-correlation and show that the SNR is adequate to produce consistent time delays down to 50 ms sample times. The static testing is discussed in the next section, which is followed by a presentation of the testing in a flow field, and then some flow field comparisons obtained using Computational Fluid Dynamics (CFD) methods.

5.2 Phased Array

Increasing the signal amplitude will clearly increase the SNR, holding all else constant, although the maximum output of the speaker is a limitation on how loud the signal can get with a single acoustic driver. This is where the concept of employing phased arrays are useful. Phased arrays have been used extensively in radar, sonar, and ultrasonic imaging. Phased arrays are a collection of transmitters that utilize the constructive and destructive interference of waves to increase the amplitude of the signal and direct the angle of the equi-phase front, θ_B, as shown in Figure 5.1.

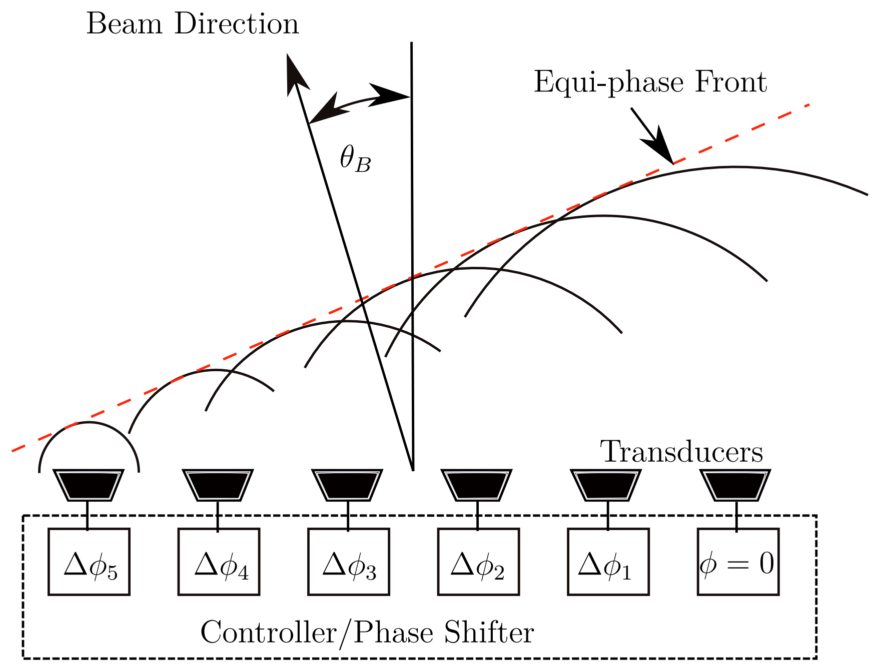

Figure 5.1: Phased array operation

Recently, Marzo et al.[58] outlined a simplified phased array system to allow for acoustic levitation of particles and haptic feedback using ultrasonics. The author of the present work is very much indebted to Marzo et al. for laying the ground work for this application of the ultrasonic phased array. Marzo provides a real-time representation of the acoustic field produced by the phased array complete with amplitude and phase contours which are based on a single frequency, far-field model of each transducer given by O'Neil [70]. The complex pressure ($P(\mathbf{r})$) given at a point $\mathbf{r}$ from the transducer orifice is given by:

$$P(\mathbf{r}) = P_0 A \frac{D_f(\theta_r)}{d} e^{i(\phi + kd)} \tag{5.1}$$

Where:

$$D_f(\theta_r) = \frac{2J_1(ka \sin\theta_r)}{ka \sin\theta_r} \tag{5.2}$$

The complex pressure incorporates a Bessel function of the first kind, J_1, and the angle between the vector perpendicular to the transducer diaphragm and point $\mathbf{r}$, given by θ_r, the reference pressure, P_0, the normalized distance between the transmitter and the point, d, the phase angle, ϕ, the aperture diameter of the transmitter, a, and the wave number, k. This simplified theory works quite well for the static cases as shown in Figure 5.2 from [58]. In [58], Marzo focused the phased array on a single point in 3D space shown as the white dot in Figure 5.2. The intent of the acoustic field was to maximize the force at the focus point and hold a particle in mid-air (acoustic levitation). The inset figures a and e show 2D slices of the 3D acoustic pressure field generated by an 8 x 8 (64 transducers total) ultrasonic phased array. These slices are calculated by Equation 5.1. Next to figures a and e are the experimental results of the actual measured acoustic field at the same slices, shown in inset figures b and f. The differences between the experimental and calculated fields is most likely due to slight variations in transducer manufacturing and variations in the phase sent by the Arduino microcontroller, which may change the constructive and destructive interference slightly and affect the measured field parameters. The right side of the Figure 5.2 shows the same slices, but the calculated (left) and measured (right) phase field.

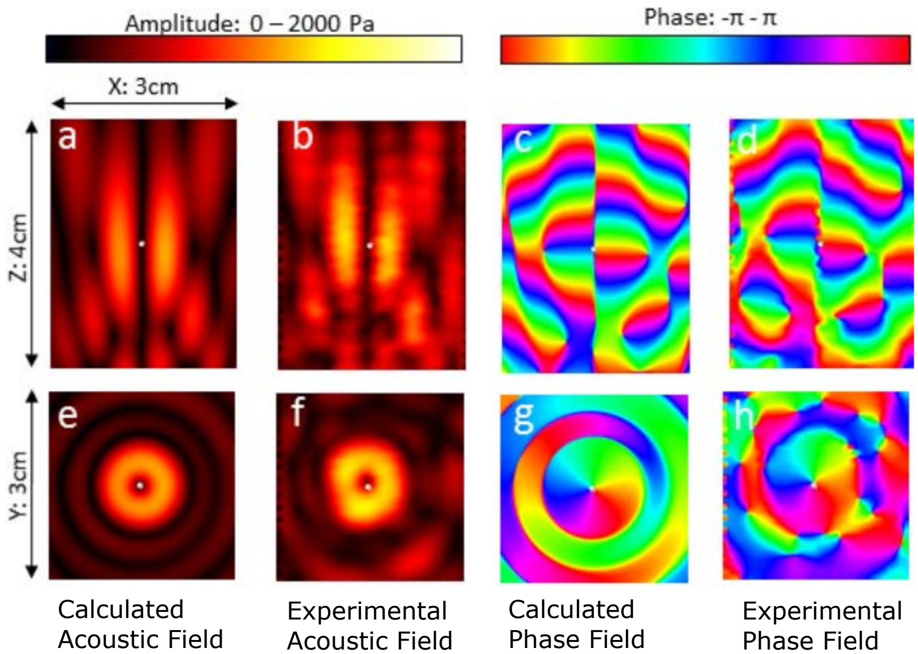

Figure 5.2: Acoustic field approximation (Left) compared with experimental results (Right) for the acoustic pressure field and phase contours [58]

The above method is used to set the phases of the array to set the maximum amplitude toward a focal point. The next section shows the verification of the impact of the phased array under static conditions.

5.3 Phased Array Performance for Sonic Sensor

To apply this technology to the sonic sensor problem, a phased array is constructed using six Murata ultrasonic transducers arranged linearly. These ultrasonic transducers are optimized to produce a 40 kHz tone and the frequency response falls off rapidly both above and below 40 kHz. The transducers are connected to a amplifier, which is connected to an Arduino Mega microcontroller. The specifications for the amplifier, controller, and software are freely available and can be found in [58]. Once the system is assembled, measurements at a representative microphone with a single source and the phased array source are compared to quantify the acoustic power increase due to the phased array. A single PCB 130B40 microphone is placed facing the phased array three inches from the face of the linear array, as shown in Figure 5.3.

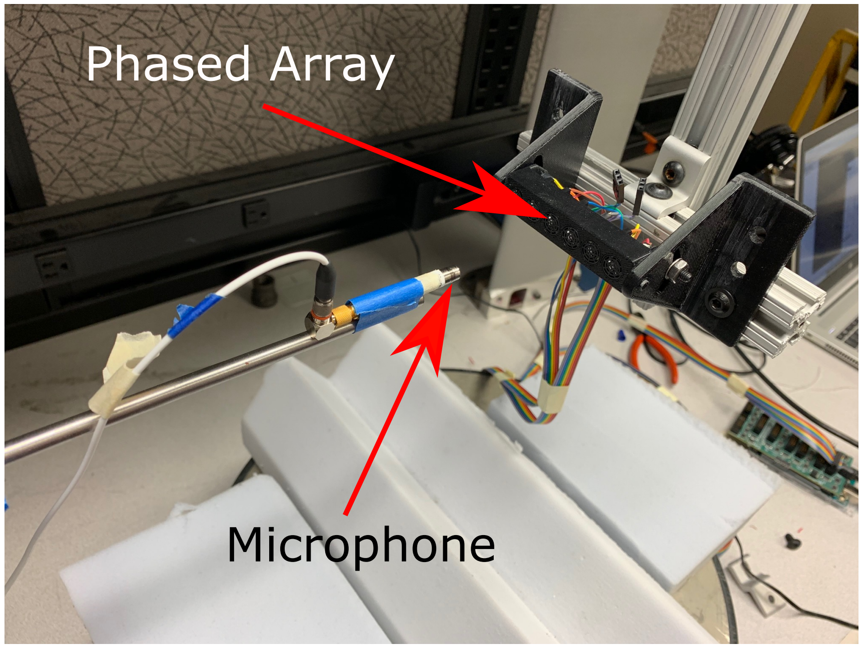

Figure 5.3: Static phased array test set up with six transducers linearly arranged three inches from the receiving microphone

The phases are then changed at 10 ms, 100 ms, 200 ms, and 500 ms intervals to allow for the ultrasonic beam (region of high SPL) to pass over the microphone. This means that the phases are held constant for the designated time, and then switched to the next phase arrangement to allow for the sweeping of the acoustic beam over the microphone. Using the software developed from [58] the acoustic field is simulated and the phases of the transducers are calculated to direct the beam such that the maximum amplitude is on the focal point. Figure 5.4 shows four views of the acoustic field as the focal point is moved across the phased array on a three inch radius centered at the middle of the phased array. It should be noted that these are just a few of the acoustic fields of the swept signal, and more are included in the test to have a smoother transition as the beam is swept over the the microphone. During the test, the focal point is moved in 5 degree increments over the phased array. As the progression in Figure 5.4 shows, the region of high SPL (shown in red) passes across the domain displaying the acoustic boost and beam steering capability of the phased array. It should be noted that at $\theta_B = \pm 20$ deg the side lobes of the phased array become more pronounced.

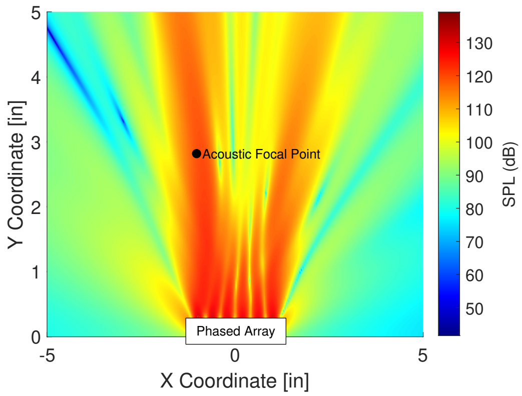

(a) θ_B = -20 deg

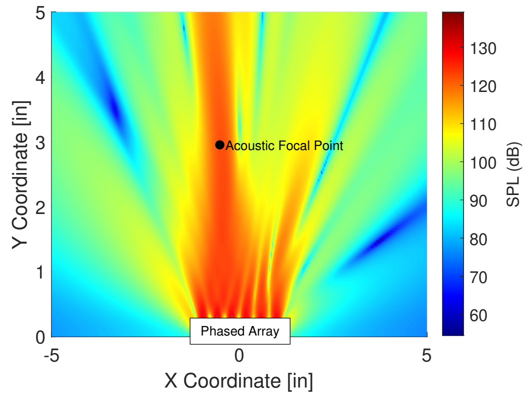

(b) θ_B = -10 deg

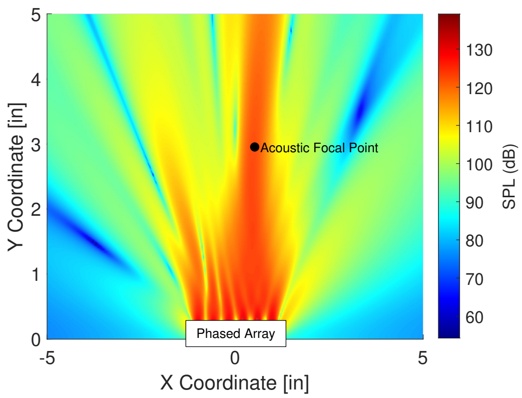

(c) θ_B = 10 deg

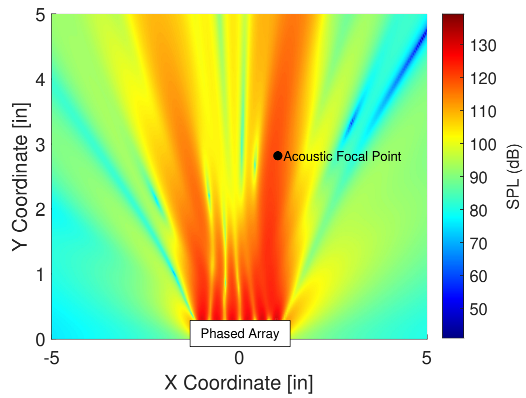

(d) θ_B = 20 deg

Figure 5.4: Calculated acoustic field for a sweeping phased array

The SPL at the microphone during this test is shown in Figure 5.5. The single transducer is shown as the dashed black line at around 122 dB. The impact of the phased array is immediately apparent with an increase in SPL to 132 dB. This verifies the phased array is performing as expected, and looking back at Figure 5.4, the magnitude of the acoustic power matches well with the computed acoustic field. The phased array increases the acoustic power approximately 10 dB which is a significant improvement over the single transducer. The stair stepping effect is the ultrasonic beam sweeping closer to the microphone position and can be easily seen in the 500 ms phase hold plot of Figure 5.5. The maximum SPL is reached for each of the phase hold times with the exception of the 10 ms phase hold. The SPL is increased from the single transducer, but the reduction in SPL is due to the time it takes for the transducer to reach an equilibrium state after a signal is sent through the transducer. The ideal phase hold time is around 100 ms for the current setup which allows for the maximum SPL, and during the sweep of the acoustic beam.

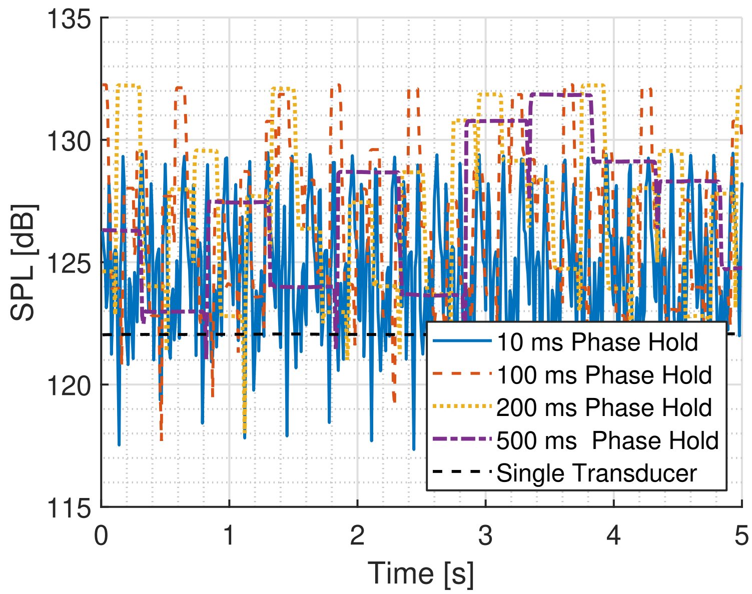

Figure 5.5: Static phased array performance compared to a single ultrasonic transducer located at a distance of 3 in. from the phased array

It should be noted that the minimum phase hold time (100 ms) for maximum SPL is larger than the desired refresh rate of 50 ms for the sonic sensor, and would essentially be a tone read by the receivers. Therefore, a tone is used for the experimental testing since the settling time of the transducer reduces the benefit of the phased array. As noted earlier, the tone produces some issues when it comes to determining the correct time delay using the cross-correlation and will be addressed in the following sections. Next, the phased array will be placed in a flow field and tested up to a Mach number of 0.48 (Maximum for the facility available).

5.4 High-Speed Testing with Phased Array Technology

The previous section showed the power of the phased array to produce an SPL higher than that which can be obtained with a single transducer under static conditions. Flow field effects are introduced by placing the phased array in a small open-jet facility at GTRI. The test model is shown in Figure 5.6.

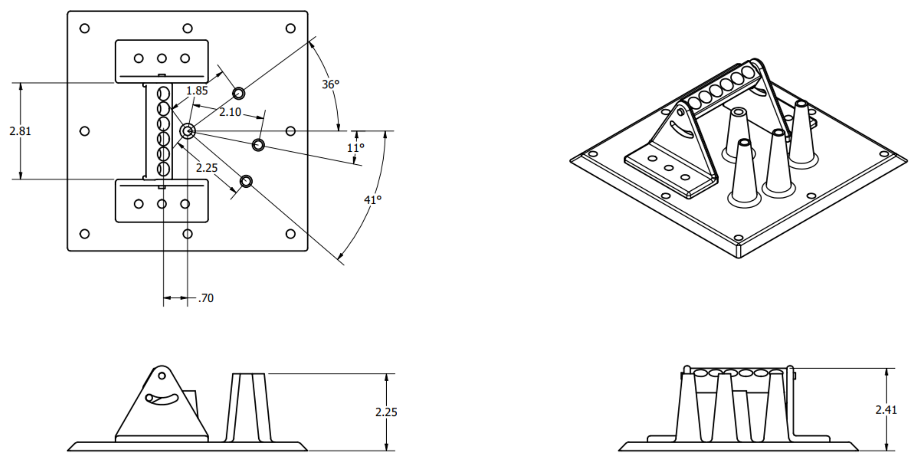

Figure 5.6: Model geometry dimensions in inches

The geometry of the test setup is given in Table 5.1.

Table 5.1: Receiver geometry used in phased array experiments

Receiver	L [in]	θ [deg]
R1	1.85	36.0
R2	2.10	11.0
R3	2.25	41.0

Three receiving microphones are positioned downstream of the phased array as shown in Figure 5.7. The diaphragms of the microphones are not placed on the same plane as the phased array to reduce the impact of any wakes on the estimated time delay. This will be discussed more later in this Chapter.

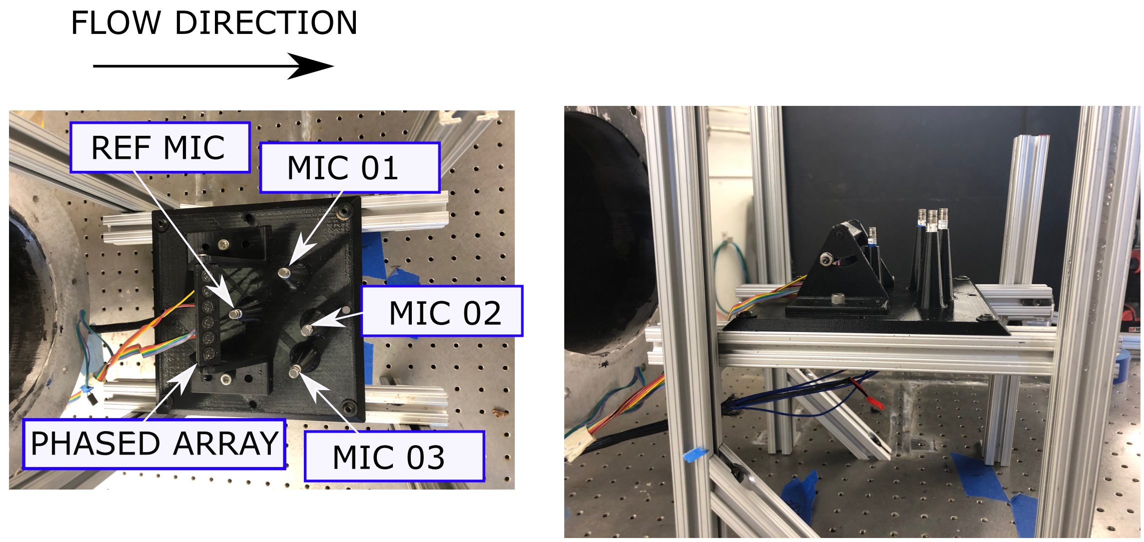

(a) Model top view

(b) Model side view

Figure 5.7: High-speed test setup

The phased array is tilted 15 degrees, about the spanwise axis, toward the receivers to increase the SPL at the receivers. The whole sonic sensor test model is placed directly in the jet and the flow speed is increased to Mach 0.5 in 0.1 increments. Throughout these tests, the microphone data is recorded for 10 seconds at each Mach number. The velocity is measured by a set of static rings upstream of the exit of the nozzle. The electronic signal sent to the middle two ultrasonic transducers in the phased array is recorded as well as a reference microphone near the source to serve as the reference signal of the cross-correlation. The location of the microphones are overlaid with the acoustic field calculated by Equation 5.1 to show their placement in the region of high SPL. Since a tone is used at the source for this test, the phase of the tone at the microphone may affect the cross-correlation, therefore a phase field is included in Figure 5.8. There is a slight phase mismatch, and must be accounted for accurate time delay estimation. The phase mismatch between the receivers can be accounted for in the determination of the acoustic centers. There will be a slight change in the distance between the source and receiver, but at the frequency tested

(40 kHz), the error is minimal.

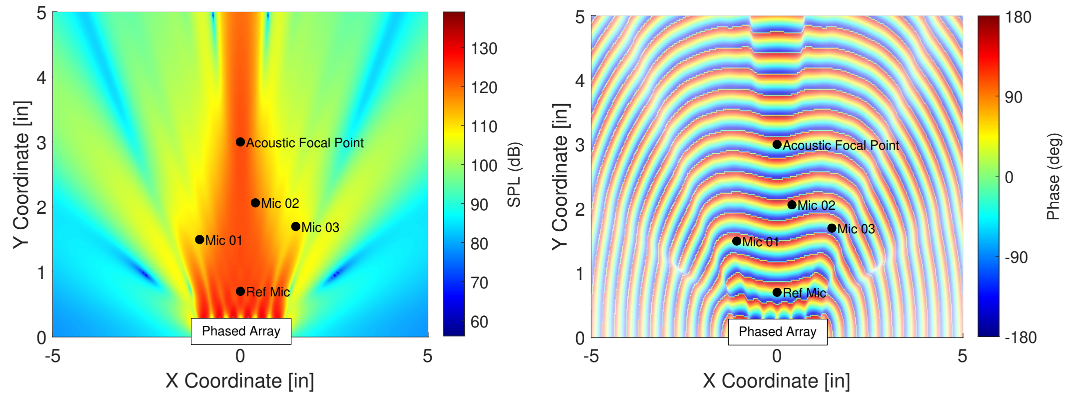

(a) Focused beam acoustic field

(b) Focused beam phased field

Figure 5.8: (a) Acoustic field for focused beam on point three inches downstream of the center of the phased array (b) Phase field for focused beam on a focal point three inches downstream of the center of the phased array

As discussed in the previous section, using a phased array increases the SPL received for static conditions. The increase in SPL is expected to be achieved in the presence of flow, but it is necessary to ensure the SNR is strong enough for cross-correlation purposes, even at 0.05 second sample times. To accomplish the comparison between the single transducer and the phased array, the open-jet facility is ramped up to Mach 0.5 with the sonic sensor in the test section. A single transducer in the center of the linear array is activated and the data is measured over 10 seconds. Then the full phased array is activated and another measurement is obtained over 10 seconds. Mach 0.5 was the highest speed tested, and would have the highest hydrodynamic noise so this is a worst-case scenario for the facility. Figure 5.9 shows comparison of the single transducer(a) and the activated phased array(b). Both frequency spectra exhibit a peak at 40 kHz, which is the design frequency of the transducers. The tone of the single transducer is nearly masked by the flow noise at these speeds even at the higher frequencies. It should be noted that the frequency spectrum for each condition was averaged 200 times to help define the spectrum better. Comparing this to the phased array data, the same 10 dB increase in SPL is seen in the spectrum and comes with a boost in SNR.

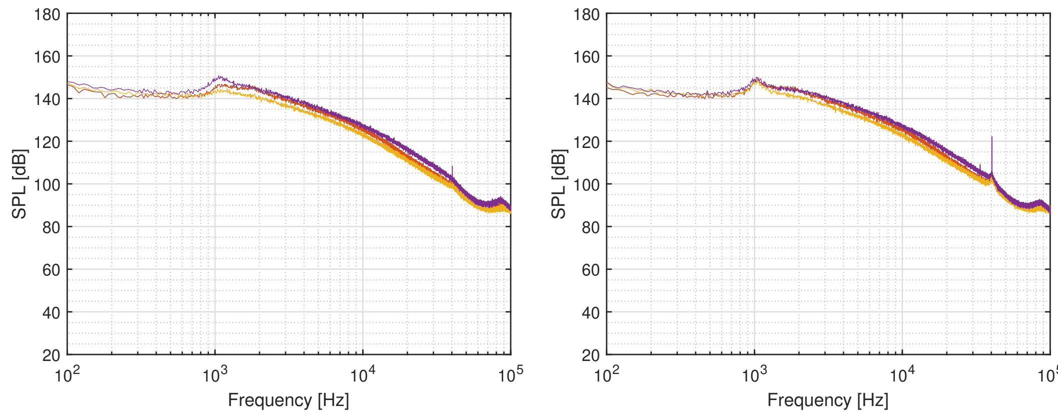

(a) Single Transducer

(b) Full Phased Array

Figure 5.9: (a) Spectra for a single transducer activated at $M_\infty = 0.5$ (b) Spectra for full linear phased array activated at $M_\infty = 0.5$ and $\Delta f = 1$ Hz for both spectra

From the spectra it is clear that the phased array has a strong SNR at the highest speed when compared to the single transducer. This will allow the phased array to produce a better correlation at the higher speeds where the background flow noise is significantly higher. This spectra changes significantly with the time measurement scale. As stated earlier, the sensor must have the ability to tie into air data systems and external DAq systems and measure the flow properties every 0.05 seconds or faster. To increase the SNR further, a band-pass filter is applied to the microphone data with cutoff frequencies of 39 kHz on the low end and 41 kHz on the high end. The spectra of the filtered signal, shown in Figure 5.10 for four separate sampling times, clearly shows the 40 kHz signal topping the background noise even down to sampling times of 0.05 seconds.

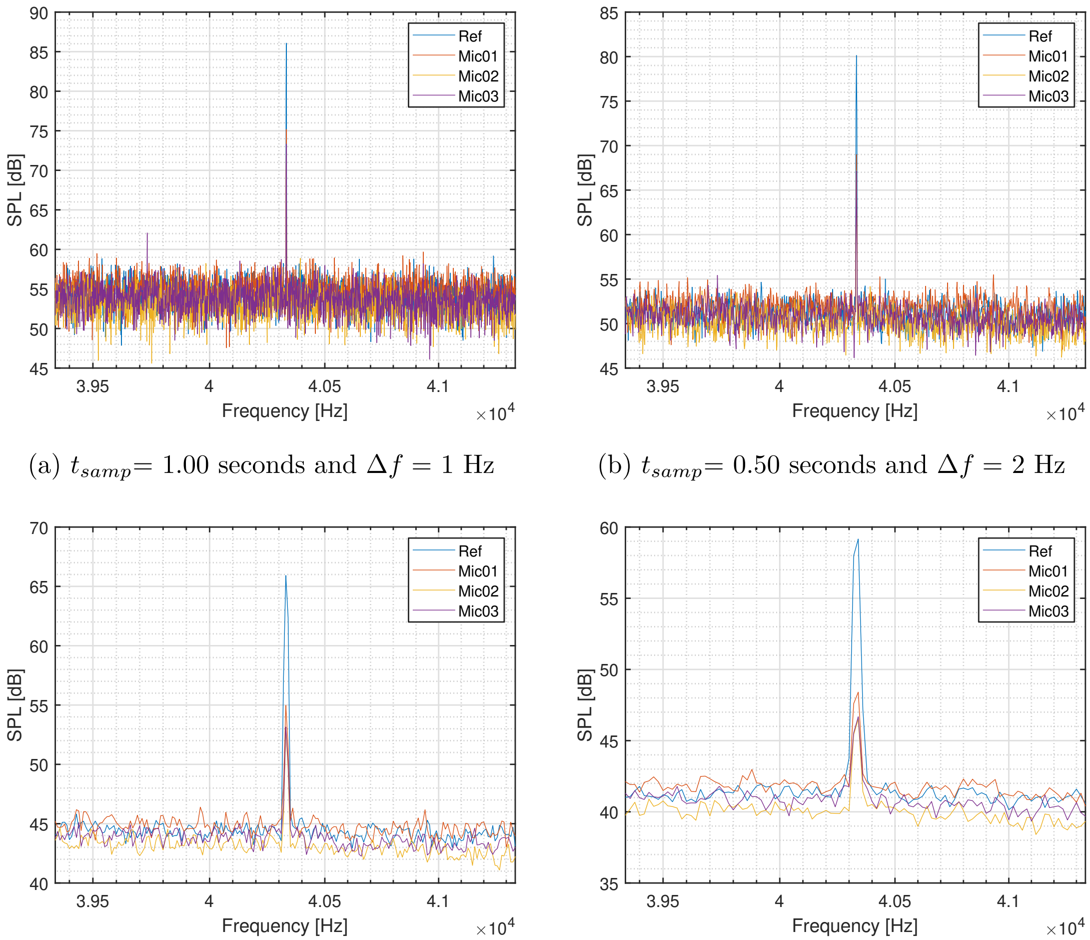

(a) t_{samp}= 1.00 seconds and Δf = 1 Hz

(b) t_{samp}= 0.50 seconds and Δf = 2 Hz

(c) t_{samp}= 0.10 seconds and Δf = 10 Hz

(d) t_{samp}= 0.05 seconds and Δf = 20 Hz

Figure 5.10: Filtered spectra at M_∞ = 0.489 for various sample times

As discussed in Chapter four, the cross-correlation of a sine wave returns a shifted sine wave. Using this knowledge, the result of the cross-correlation can be up-sampled to increase the accuracy of the estimated time delay without incurring a unreasonable sampling rate for the DAq. The sampling rate for this test is 500 kHz, which is well above the Nyquist frequency for a 40 kHz signal, and the up-sampling will not result in any loss in the signal definition. The cross-correlation is re-sampled to 800 times the original rate, or 400 MHz. This does come with added computational time, but it is expected that there can be a balance between the sampling rate and the up-sampling of the signal to achieve the desired computational performance. The electronic signal sent to the transducers is used as the reference in the cross-correlation to get the estimated time delay.

Signal frequency content or signal uniqueness is sacrificed for SNR and reduction in sample time by using a tone signal and phased array for these tests. For maximum SPL for the phased array, the burst must occur over 100 ms or greater burst times. This ensures that the transducer has adequate time to reach an equilibrium state from the applied electronic signal. 100 ms is too long for the desired refresh rate of 50 ms, therefore a tone is used as the source signal to achieve the desired sampling time. This signal selection results in an added difficulty in selecting the correct time delay peak in the cross-correlation due to the oscillatory nature of the cross-correlation of a tone. If the tone frequency is lowered such that the wavelength is of the same order of magnitude as the distance between the source and receiver, this would partially alleviate the peak selection issue for the cross-correlation of a tone. When the wavelength is of the same order as the distance between the source and receiver, the ambiguity in the peak selection is removed. The correct peak would always be the first peak of the cross-correlation provided the change in velocity does not shift the signal by more than one cycle. While lowering the tone frequency would work, this method is not necessarily available due to the flow noise. Looking back at the spectra in Figure 5.9, the low frequency range has more flow noise to compete with and potentially reduce the SNR further.

Another option is to move the microphones closer to the source for the same tone frequency to achieve the same effect. This would require a higher sampling rate to achieve the desired accuracy, and may come at a larger computational cost to electronically up-sample the cross-correlation and improve accuracy. Since the geometry is fixed, another method must be used. This method requires some knowledge of the correct peak location for the previous condition to inform the selection of the peak under the current conditions. For example, the peak location under static conditions is known, and this will vary with the air temperature, but the speed of sound should remain relatively consistent under static conditions even in the presence of humidity. Since the operation of the sonic sensor will most likely start at static conditions, this time delay can be used to select the peak within a certain error, which is typically about half of a wavelength of the tone source signal. As the flow around the sensor is sped up (meaning the aircraft is accelerating), it is assumed that there are no discontinuities, or large jumps, in the measured velocity, so the previous measurement for the time delay can be used to determine the current approximate time delay. Since the microphone geometry is known, the number of cycles it would take to reach the specified distance is given by Equation 5.3.

$$N_{cycles} = ceil(\frac{Lf}{V_{propagation}}) \tag{5.3}$$

The signal velocity can be approximated through a simplified Equation 4.6 by assuming a zero angle of attack given by Equation 5.4.

$$V_{propagation} = U\cos(\theta_i) + \sqrt{c^2 - U^2\sin(\theta_i)} \tag{5.4}$$

The test data is measured at discrete test points and not continuously measured throughout the test so these equations are used to determine the number of cycles for the specified test Mach number. If the data was read continuously, the data from the previous sample could be used going all the way back to static conditions. Table 5.2 shows the results based on the speed of sound at standard atmosphere. This will correspond with the number of peaks from zero time delay in the cross-correlation and provides a method for selecting the correct peak for the time delay. For example, if the flow is at Mach 0.3, the correct time delay for the signal at Mic 1 would be the seventh peak over from the zero delay reference.

Table 5.2: Number of cycles to reach receivers at selected Mach numbers

Mach Number	N_{cycle_1}	N_{cycle_2}	N_{cycle_3}
0.0	8	9	9
0.1	8	8	8
0.2	7	7	7
0.3	7	7	7
0.4	7	6	6
0.48	6	6	6

The values in Table 5.2 are used in the current analysis to determine the estimated time delay at the tested Mach numbers. The sonic sensor measurement hinges on an accurate prediction of the time delay of the sent signal from the acoustic source. Under steady flow conditions, the estimated time delay should have minimal variation. This idea can be seen in the static test results shown in Figure 5.11a for a sample time of 0.05 seconds. The estimated time delay has a little variation, but this is mainly due to the open-jet facility at GTRI not being fully enclosed, and any airflow or wind could impact the time delay determined by the cross-correlation. For the most part, it is constant and can be used to find the acoustic centers of the receivers. Determining the distance from the source to the acoustic centers also allows for a verification of the above methodology for the peak selection under static conditions. Allowing the static conditions to define the acoustic centers will also help account for any variation in phase in the signal as shown in Figure 5.8. The static conditions are sort of a trivial results as the speed of sound under static conditions is known and well documented. The challenging aspects do not occur until the airflow is increased. Figure 5.11b through Figure 5.11f show the progression of the estimated time delay for all test conditions with flow up to Mach 0.489. Each figure represents the data at a given Mach number shown in the figure caption and shows the calculated time for the signal to arrive at each of the three microphones used. With the exeption of the results at Mach 0.305, shown in Figure 5.11d, the estimated time delay is consistent. There is a increased variation over the static case, but the estimated time delay over the entire sample is fairly steady. Turbulent flow in the wake of the phased array support structure is the cause of the variation in the time delay estimation, and will be discussed later in this Chapter. For the Mach 0.305 flow conditions, Figure 5.11d, a large transient effect is shown that is impacting the estimated time delay at Mic 03. The reasons for this are discussed in subsequent sections. Most importantly, Figure 5.11f shows that the SNR is high enough to produce a cross-correlation with a consistent peak at the approximate time delay even at sample times of 0.05 seconds using a phased array.

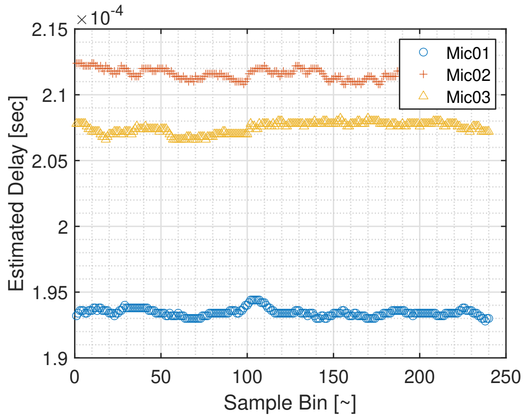

(a) $M_\infty = 0.0$

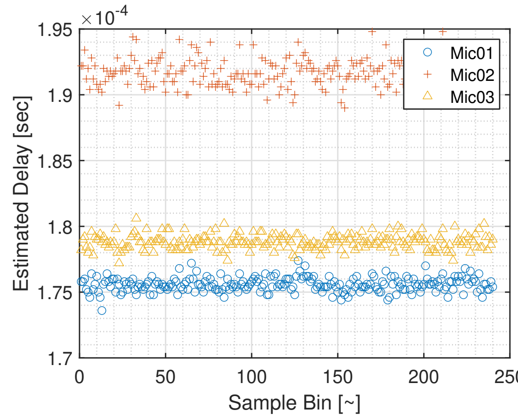

(b) $M_\infty = 0.105$

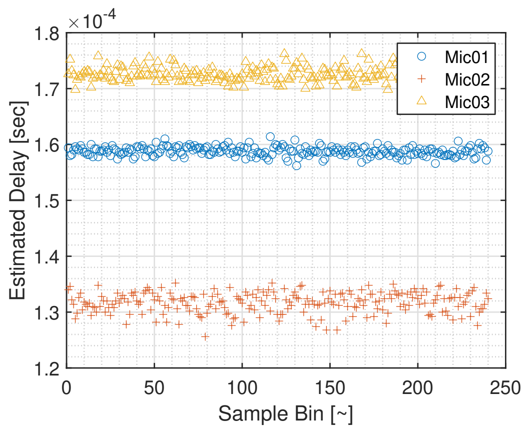

(c) $M_\infty = 0.203$

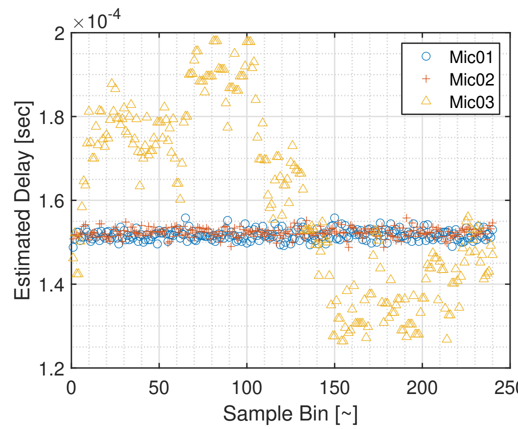

(d) $M_\infty = 0.305$

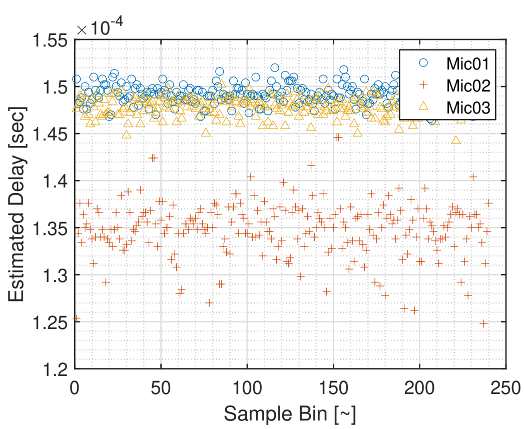

(e) $M_\infty = 0.405$

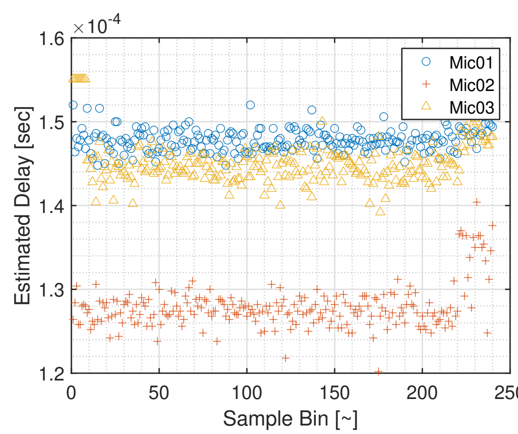

(f) $M_\infty = 0.489$

Figure 5.11: Estimated time delay with focused phased array signal for a 0.05 second sample time

Increasing the sample time to 0.1 seconds allows for less variation in the estimated time delay as shown in Figure 5.12. The transient effect is still seen in the results at Mach 0.305 for Mic 03 as seen in Figure 5.12d. The minimization of the variation in the estimated time delay is due to effectively taking an average time delay over 0.1 seconds, double the time of Figure 5.11. Increasing the sample time further will reduce the variation in the estimated time delay further, but it would get an average time delay over the sample time. With the transient effects in the wake of the phased array support structure, this would impact the estimated time delay and may result in an estimated time delay that is more than what would occur if the acoustic signal transmitted through a steady flow field. The acoustic signal traveling through a lower speed region of the flow, i.e., a wake, would increase the time delay of the signal because it would take longer for the signal to reach the receiver than it would in a uniform flow field.

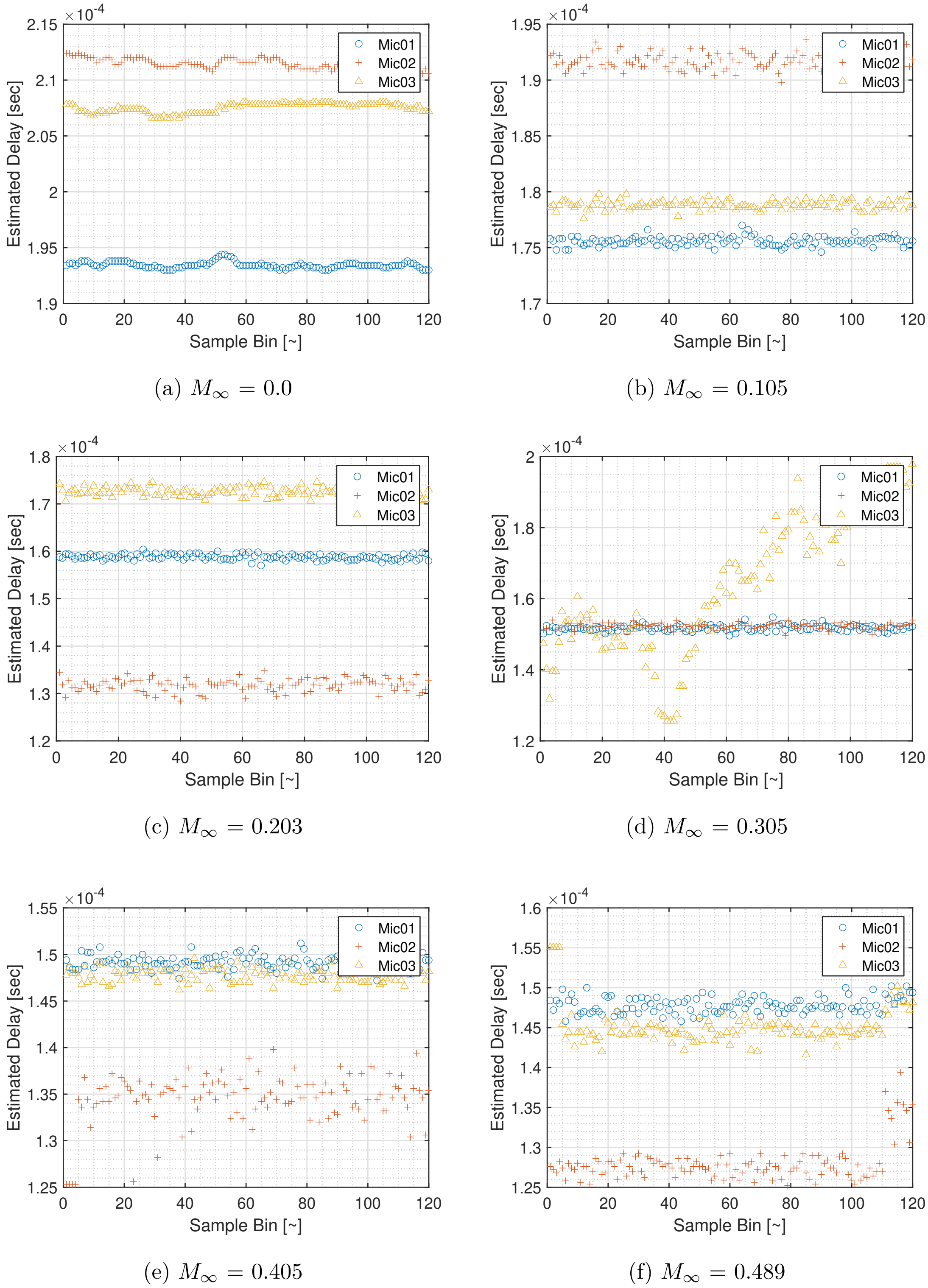

(a) $M_\infty = 0.0$

(b) $M_\infty = 0.105$

(c) $M_\infty = 0.203$

(d) $M_\infty = 0.305$

(e) $M_\infty = 0.405$

(f) $M_\infty = 0.489$

Figure 5.12: Estimated time delay with focused phased array signal for a 0.1 second sample time

The transient effect around Mach 0.3 is most likely due to a vortex being shed by the phased array support structure. Figure 5.13 shows one of the support arms of the phased array directly upstream of Mic 03. The frequency of the shed vortex seems to be very low (0.1 Hz), and most likely filtered out of the spectrum and it is outside of the frequency response of the microphones. The leading edge of the support arm acts sort of as a vortex generator around Mach 0.3 and any vortex shed off the top and trailing edge would impact the time the signal takes to get from the source to the receiver. The opposite support arm is outside the region of influence of the shed vortex, which is why Mic 01 does not have the same oscillatory behavior in the estimated time delay. A slight rotation of the sonic sensor test article could also increase the probability of a shed vortex.

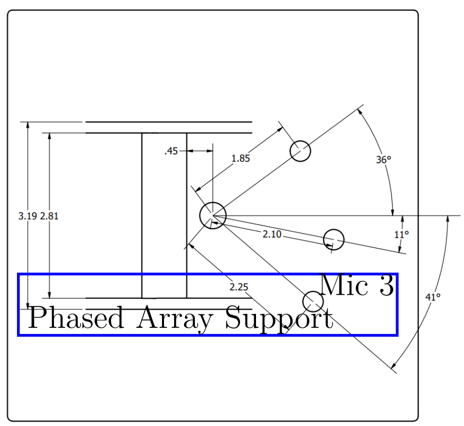

Figure 5.13: Probable source of Mic 3 transient effects

The estimated time delay was consistent for all speeds tested down to 0.05 second sample times, and probably less since the SNR is still fairly high. This means that the system can be operated at the sample speeds necessary to be integrated into air data systems. The estimated time delay is not quite as consistent as it could be, but this is due to turbulent effects in the wake of the phased array support structure. This is similar to the distortion effects of ground based ultrasonic anemometers described in

Chapter two. The next section looks at the flow field through a Computational Fluid Dynamics approach to confirm the wake of the phased array structure could be the source of the problems outlined above.

5.5 Flow Verification

As shown by the cross-correlation results, as the sample time is reduced, the variation of the estimated time delay increases. This means that the small perturbations in flow velocity due to wake effects are being captured by the cross-correlation because of the small sample times. The larger sample times allow these fluctuations to be averaged out and the estimated time delay becomes more consistent. The wake produced by the phased array structure will cause the flow downstream of that to be lower than the free-stream and will impact the results of the calculated flow parameters, especially if the reference signal is in the wake as well as how much of the measurement volume is immersed in the wake of the phased array. A Computational Fluid Dynamics (CFD) model is used to analyze the flow field behind the phased array. CFD is used to determine the effects of the wake of the phased array support structure and see if corrections can be applied to assist in the calculation of the flow properties. The CFD simulation is performed using Ansys Fluent 17.1 [71]. The CFD model is shown in Figure 5.14b with the characteristics outlined in Table 5.3. Mach numbers simulated are 0.2 to 0.5 in 0.1 increments. The flow angle is not varied in this study.

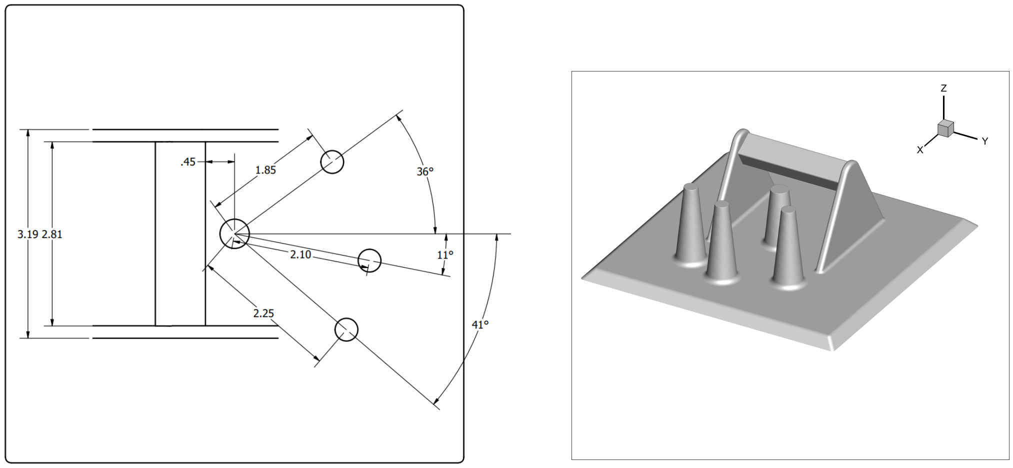

(a) CFD model dimensions (b) Isometric view of the CFD geometry

Figure 5.14: CFD model geometry

Table 5.3: CFD mesh and computation characteristics

Number of Cells	10 Million
Mesh Type	Unstructured
Compressible Viscosity	Sutherland
Turbulence Model	k-ω

When interrogating a 3D flow field, it is useful to look at a 2D slice of the data to better see the details of the flow. The slice of data is the approximate acoustic path plane to the receivers as shown in Figure 5.15a. It should be noted that the acoustic signal is not restricted to this plane, but the plane is representative of the flow field that the signal may travel through. The measurement volume is approximated by the following plane in the flow field. A side view of the test article is shown in Figure 5.15b for reference.

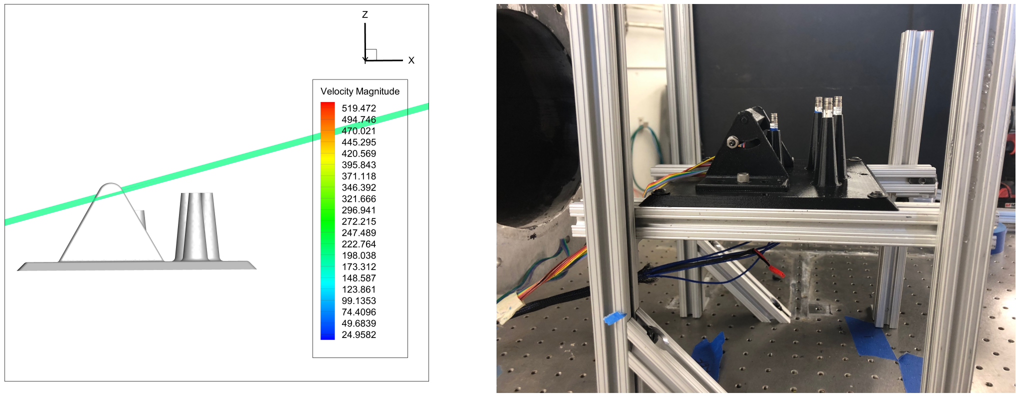

(a) (b)

Figure 5.15: (a) Plane in which the flow field velocity is evaluated to compare with experimental results (b) Side view of test setup showing microphone locations

The peak in the test spectra shows that the SNR should be adequate to extract the signal from the noise for the cross-correlation purposes. The reduction in the estimated time delay requires a look into the flow conditions that could be the cause. The test setup features a forward and backward facing step that could cause some flow separation issues and increase the size of the wake behind the phased array support structure. The height of the microphone diaphragms were offset from the support structure to alleviate any wake interference, but the impact of the combination of forward and backward facing steps are the source of significant errors. Forward and backward facing steps have been an area of research for CFD for the past decade ([72, 73]). The flow around such steps is well documented, and the increase in the size of the wake may be impacting the time of flight of the signal, which would account for the decrease in the calculated velocity when compared to the reference. Figure 5.16a shows the calculated flow of the forward- and backward-facing step over the phased array support structure on the flow field downstream of the phased array. The large wake is characteristic of the forward- and backward-facing step and presents a large region of non-uniform flow for the acoustic signal to pass through to the receivers. The flow field shown in Figure 5.16a and Figure 5.16b are just representative. The figures below are for Mach 0.3, but the flow at all speeds show a similar wake behind the phased array structure.

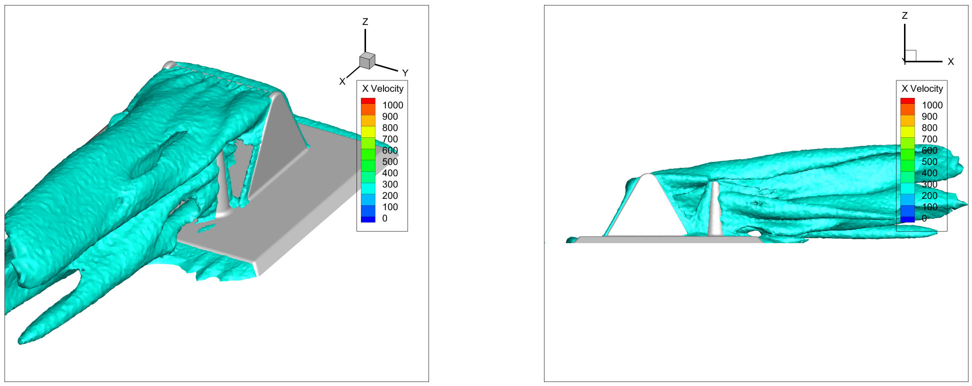

(a) (b)

Figure 5.16: (a) Isometric view of a 260 ft/s iso-surface contour for $M_\infty = 0.3$ (b) Side view of a 260 ft/s iso-surface contour for $M_\infty = 0.3$.

Raising the microphones higher than the phased array did not quite get them out of the wake and cause the method developed for the calculation of the flow velocity and angle of attack to break down and produce erroneous results which is why the flow velocity calculation is not included in this work. Using the measurement plane defined in Figure 5.15a, contours of velocity magnitude are shown in Figure 5.17 for Mach 0.2 to Mach 0.5. As the figure shows, there is a significant wake structure behind the phased array support structure. The measurement volume is not consistent and each microphone will measure a different flow velocity component, which causes a breakdown in the initial assumptions when developing the sonic sensor methodology. The initial assumption was that the flow velocity and speed of sound are constant in the formulation of the equations for calculating the flow speeds with the sonic sensor. This is obviously not the case as can be seen by inspecting the contours in the measurement plane.

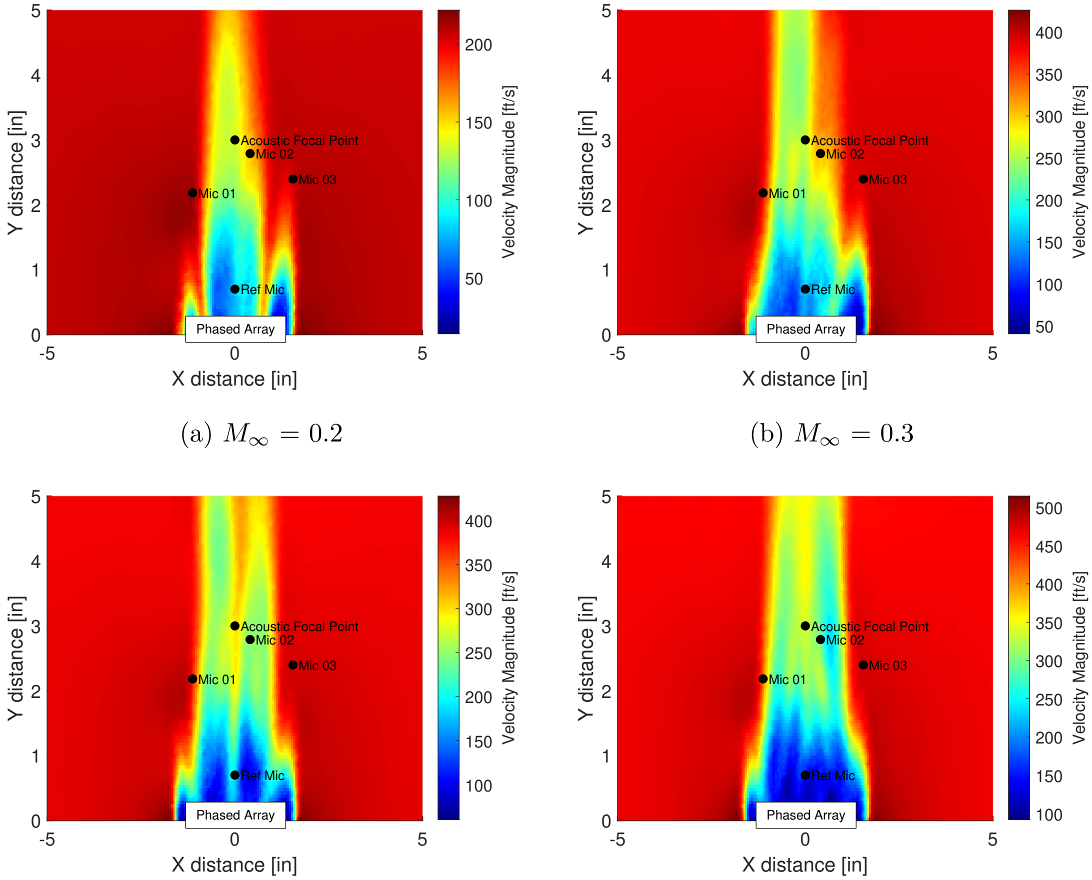

(a) $M_\infty = 0.2$

(b) $M_\infty = 0.3$

(c) $M_\infty = 0.4$

(d) $M_\infty = 0.5$

Figure 5.17: CFD acoustic path plane velocity magnitude contours

The average velocity over a straight line path from the middle of the phased array to the receiver is given in Table 5.4. The velocity magnitude is different for each path, which will present difficulties when trying to calculate the flow parameters. Now, this presents a bit of an issue with the way that the sonic sensor operates and calculates the flow speed, speed of sound, and angle of attack. The initial assumption is that the flow speed, U, is the same for all paths. With the introduction of flow separation and turbulent wakes, this is not necessarily the case. Depending on the acoustic path to the receiver, the signal could have a longer time getting to the receiver whether it passes through the wake, or travels outside of the wake, thus increasing the distance traveled and the delay of the signal getting to the receiver. With much of the measurement volume impacted by a turbulent wake, it is difficult to ascertain any correction factors that could correct the collected data. From Chapter 3, the assumption to get the flow properties was a uniform velocity in the measurement volume, and is not held for the current geometry-flow field combination. Any results/conclusions from the calculated flow values are limited to determining a consistent time delay estimation for all speeds tested and down to 0.05 second sample time.

Table 5.4: Average velocity (in ft/s) over a straight line path from the origin to the receiver

Mach Number	V_{avg_1}	V_{avg_2}	V_{avg_3}
0.2	79.68	114.36	130.32
0.3	148.37	191.78	227.13
0.4	141.38	200.34	223.93
0.5	153.99	223.85	235.33

The CFD is a steady state solution, and will not show transient effects like the shedding of vortices. Vortices are most likely the cause of the oscillations in the estimated time delay around Mach 0.3 in the test data. The oscillations seem to occur at a very low frequencies.

5.6 Summary Remarks

This chapter showed that the utilization of the phased array produced signals with SNRs that are high enough to use in cross-correlation techniques and determine the propagation time of a signal up to the maximum speed tested (Mach 0.489) and down to 0.05 second sample times. The cross-correlation produced consistent time delays accounting for flow variations due to turbulent effects. Unfortunately, the flow structure behind the phased array support did not yield an environment conducive to flow measurements. The initial assumption that the flow velocity is uniform in the measurement volume does not hold in the wake of the phased array support, and each receiver may be measuring a different average velocity in the wake over the acoustic path traveled. This causes the calculated flow parameters to have significant errors and no conclusions on the flow speed and angle of attack can be determined. The velocity calculation has been proven for low speed as shown above, and it seems to be robust if at least two of the receivers have an acoustic path traveling in a flow field that is close to free-stream. This is shown in the angle of attack results for the low-speed tests. The calculated velocity is still fairly accurate, but the angle of attack deviates when one of the receivers is impacted by the wake of the support structure.

The cross-correlation yields a consistent estimated time delay for Mics 1 and 2 for all speeds tested. Mic 3 appears to be impacted by a non-uniform flow feature, such as a shed vortex, around Mach 0.3. This transient effect is most likely caused by the phased array support arm directly upstream of Mic 3. At speeds above $M_\infty = 0.3$, the estimated time delay settles down and is no longer affected by any flow features showing the transient effect is no longer present. The flow distortion due to the support structure is still a major issue and hindrance to accurately calculating the flow parameters. A test article with more of an eye to controlling the flow in the measurement volume would go a long way to improve the flow parameter measurements. Since the assumptions for calculating the flow properties broke down due to flow distortion by the wake, an uncertainty analysis does not have a significant meaning and therefore is not included in this work.

CHAPTER 6
CONCLUSIONS

The objective of this work was to lay the ground work to extend sonic anemometry to high speed flows including practical sampling rates to keep up with current state-of-the-art air data systems. The sonic sensor theory has been developed, computationally verified, and experimentally tested at low speeds with a high degree of accuracy. The flow velocity and temperature measurements were within the error bands of the conventional measurement techniques, and the angle of attack measurement were accurate until the point at which the support structure wake began impacting the measurement volume. The source signal was being masked as the flow velocity was increased and introducing errors in the measurement technique. It is shown that a phased array can be used as a source for the signal at high speeds with ample SNR to reduce the sampling rate down to 50 ms and still produce consistent time delay estimation over the whole data set up to a free stream Mach number of 0.489. This is the first use of phased array technology in a sonic anemometry application. The SNR at the highest speed tested was high enough to allow the method to be used at higher speeds. Application of the current work is limited to the capability of the test facility. The work is plagued by support structure wake impacting the measurement volume and causing the fundamental assumptions in the development of the sonic sensor methodology to break down as shown in the CFD results. A summary of contributions of the author is provided in Chapter 1 and is repeated below as part of the conclusions of this work. Recommendations for follow-on research are discussed in the following sections.

6.1 Summary of the Contributions of the Current Work

This work furthers the state-of-the-art in a number of ways.

1. This work derives and verifies a methodology to calculate the flow speed, angle of attack, and air temperature for aircraft applications. There have been many methodologies for sonic anemometry, but this configuration considers the sound source upstream of the receivers, and in a small package so as not to cause more drag and increased weight that the currently commercially available systems suffer from. The methodology has been successfully flight tested by Georgia Tech Research Institute (GTRI) and is currently being considered by Aerosonic for integration into a production prototype package.

2. It is the first application of phased arrays to the ultrasonic anemometer problem. It holds potential for application of the methodology developed here to high flow speeds where a single speaker/source may not provide the necessary Signal-to-Noise Ratio (SNR). The application of acoustic phased arrays allows for both an increase in Sound Pressure Level (SPL) as well as the capability to direct the sound beam within a certain angular sweep. The beam can then be adjusted in such a way as to direct the point of strongest SPL to the receivers. Although still additional work is needed, this is the first time this technology has been tested for determining the speed of the free-stream air as well as other flow parameters and is a building block for extending the current work to high flow speeds, including supersonic and hypersonic flows.

3. This work shows the required SNR to achieve consistent cross-correlation down to a 0.05 second sampling time to integrate into flight data systems. One of the main drawbacks of cross-correlation is the sample time required to achieve a discernible peak in the cross-correlation. Many systems use times on the order of one second to accurately determine the time delay from cross-correlation.

This work shows that sample times on the order of 0.05 seconds are achievable if the SNR if high enough for the cross-correlation to pick out the signal from the uncorrelated noise.

6.2 Recommendations and Future Work

From the work shown, it is clear that the phased array provides a method of increasing the SNR of the sonic sensor in an effort to measure the flow properties at higher and higher velocities. The following sections present some other areas of research to further the state of the art of sonic sensors to higher speeds.

6.2.1 Refined Testing

The main struggles for this method is having a clean measurement volume such that the sent signal is propagating in free-stream conditions. This can be done better by having a more aerodynamic design of the phased array support structure. The forward and backward facing step of the phased array support induced too much flow fluctuation to get an accurate measurement of the flow properties. A redesigned test structure with a focus on a measurement volume that is more representative of the free-stream conditions would go a long way in improving the accuracy of the desired flow parameters. Incorporating smaller microphones (MEMS type) will also decrease the support structure required to ensure the receivers are outside of the boundary layer.

The open-jet nature of the test facilities may have introduced some error as can be seen in the minute changes in the acoustic signal propagation time for 'static' conditions. The slightest breeze could have an influence on the signal propagation time under static conditions, and since the facility was open to the outside air to allow the Mach 0.5 speed air to exhaust, the measured acoustic distances could be influenced by this effect. The meteorological uses of ultrasonic anemometers include measuring turbulent intensities. These minor changes in the time delay could make it difficult to accurately determine the acoustic centers of the receivers and change the propagation velocity of the signal in the flow.

Another possible area of research with the current methodology is to study the impact of the choice of the reference signal and how that impacts the estimated time delay. Since the phased array is made up of many transducers, the phase field does not match the point source distribution, which could be causing an introduction of error in the estimated time delay of the signal.

6.2.2 Other Source Considerations

The selection of the source signal dictates how the signal is processed. A pure tone was used in this work to get a consistent estimation of the time delay between the source and the receiver. This is due to the fact that a phased array was being used to increase the sound power and overcome the flow noise. The utilization of other transducers can increase the frequency content of the signal and add more points of comparison to draw out the peak from the cross-correlation. Other combination of transducers that have differing operating frequencies could be used to boost the source signal, and generate a more unique signal for the cross-correlation and make the estimation of the time delay simpler.

The amplitude of the signal could be modulated as well as was done by [34]. There should be some caution when applying this signal type as the amplitude modulation may get lost in the hydrodynamic noise of the flow. While the modulation seemed to work well, Otero et. al. [34] had to increase the SNR by zeroing out the signal between the pulses. Also, Otero et. al.[34] reduced the impact of the hydrodynamic noise by having the receivers outside of the flow field. This technique is not available to the sonic sensor.

6.2.3 Machine Learning for Sonic Sensor

The increase in computing power has opened up a large range of applications for Machine Learning for analytical model development. Most recently this method has been applied to time series analysis and estimated time delay with exceptional results. Houegnigan, et al. [74] built off the work done by Shaltaf[75], and presented some interesting results when comparing the machine learning analysis to the traditional time delay estimation (generalized cross-correlation and regular cross-correlation). Figure 6.1 shows the comparison of between the methods. Machine learning algorithms may have a leg up on the cross-correlation in consistency of results and could produce a fairly accurate estimated time delay.

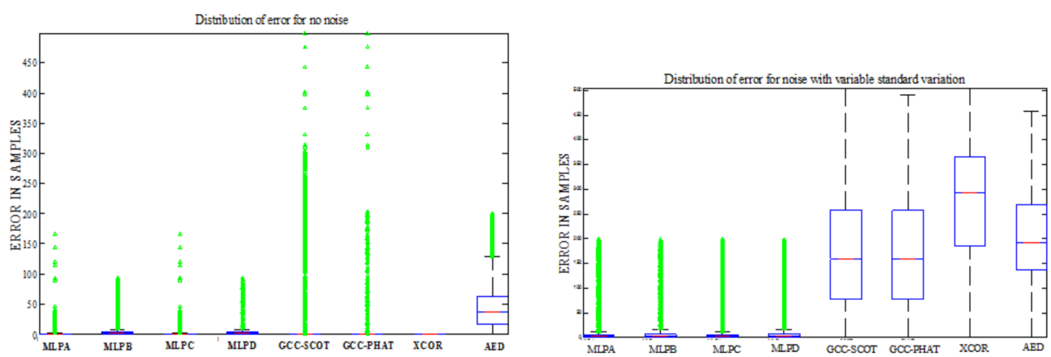

(a) (b)

Figure 6.1: (a) Error of traditional time delay estimation as compared with machine learning algorithms under no noise conditions (b) Error of traditional time delay estimation as compared with machine learning algorithms under random SNR conditions [74]

As can be seen in the results of the error estimation, a significant improvement is made over the traditional delay estimation methods even for random noise characteristics. These Machine Learning techniques would be a powerful tool to incorporate into the sonic sensor.

Not only has machine learning been used to estimate the time delay, it has also been used to de-noise audio signals. The combination of audio denoising and estimation of time delay will alleviate the issues that were encountered in this work and provide a path to develop a consistent and powerful means of measuring flow properties based on acoustic propagation. More research and certification of machine learning will have to be done before it makes its way onto aircraft, but the techniques developed present a promising path for integration on the sonic sensor platforms.

6.2.4 High Speed and Supersonic Testing

The current methodology is applicable to supersonic flow fields as long as the SNR is high enough for the sent signal to be accurately determined in the cross-correlation or the cross-spectra, and if the acoustic receivers are in the zone of influence as defined by the Mach angles. The current formulation does not take into account any dissociation or high temperature effects that become non-negligible in the hypersonic flow regime(Mach$>\sim$5). At these speeds the temperature and chemical composition are changing rapidly. This will lead to errors assuming a constant γ, even with the correction for humidity effects. If an isentropic assumption still holds as well as assuming the flow reaches an equilibrium state before reaching the source and receivers, the equilibrium speed of sound is given by:

$$a_e = \gamma RT \frac{\left[1 + \left(\frac{1}{\rho}\right)\left(\frac{\partial e}{\partial v}\right)_T\right]}{\left[1 - \rho\left(\frac{\partial h}{\partial p}\right)_T\right]} \tag{6.1}$$

Where, γ is the ratio of specific heats, ρ is the density of the air, R is the specific gas constant, T is the temperature, $\left(\frac{\partial e}{\partial v}\right)_T$ is the change in energy due to a change in volume at constant temperature, and $\left(\frac{\partial h}{\partial p}\right)_T$ is the change in enthalpy due to the change in pressure at constant temperature. The above equation still has a γ term, which is the ratio of specific heats at a certain temperature. The ratio of specific heats variation with temperature can be seen in Figure 6.2.

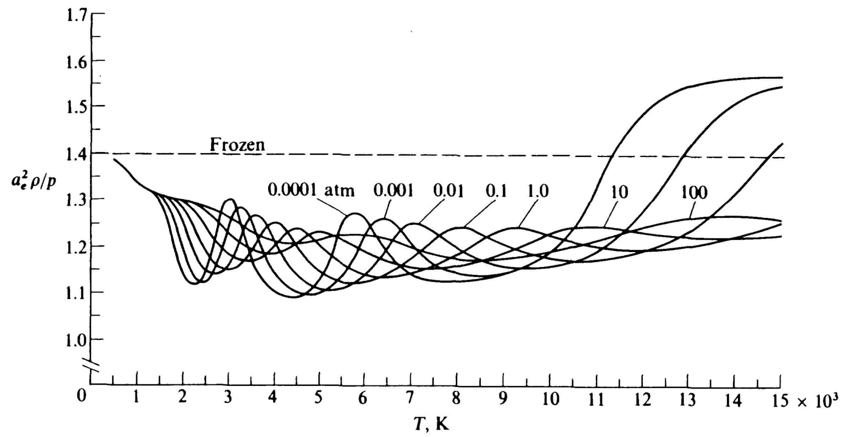

Figure 6.2: Variation of γ with temperature in air[76]

The value on the y-axis of Figure 6.2 is the ratio of specific heats, just written in a different form. Since there is such variation in γ with increasing temperature, it is unclear, at this point, how to take into account the knowledge of the temperature a priori. Some iterative solution may be necessary, but the iterative scheme must converge rapidly to allow the sensor to be incorporated into the flight data system.

Another area of research to be considered would be the effects of shocks on the acoustic propagation. As the flow approaches transonic speeds, shocks will start to form and they may be in the measurement volume. The impact of these shocks is not known, but correct placement of the sensor on the aircraft as well as carefully design aerodynamic supports for the source and receivers can minimize these effects. Still, the characterization of the shock effects on the performance of the sonic sensor is necessary for further application into supersonic flows.

Appendices

APPENDIX A
UNCERTAINTY ANALYSIS

The total uncertainty is a combination of bias uncertainty, uncertainty in the methodology and/or setup, and precision uncertainty, which can be thought of as uncertainty in the measurement source. The total uncertainty of a variable, F, is given by Equation A.1

$$U_F = \sqrt{P_F^2 + B_F^2} \tag{A.1}$$

If the bias uncertainty, B_F, is assumed to be zero, the uncertainty left is the precision uncertainty, P_F. The precision uncertainty for dependent variable, F which is a function of j independent variables, the precision uncertainty is given by Equation A.2.

$$U_F = \sqrt{\sum_{i=1}^{j} \left(\frac{\partial F}{\partial x_i} P_i \right)^2} \tag{A.2}$$

A.1 Test Section Velocity Measurement

The truth source for the velocity in the test section is measured by a pitot-static tube. This is connected to a differential pressure sensor with a range of 10 in of water in gauge pressure (3.6 psig). The differential pressure sensor has an accuracy of 0.05% of the entire range of the sensor, which corresponds to ± 0.00018 psig. To determine the uncertainty in the velocity measurement and assuming the biasing uncertainty is zero, the following equation is used.

$$U_{V_{TS}} = \sqrt{\left(\frac{\partial V}{\partial \Delta p} P_{\Delta p} \right)^2} \tag{A.3}$$

The velocity in the MTF is calculated using Bernoulli's equation:

$$P_t = P + \frac{1}{2}\rho V^2 \tag{A.4}$$

Applying the uncertainty in the differential pressure transducer produces the uncertainty in the velocity measurement at various velocities are given in Table A.1.

Table A.1: Test section velocity uncertainty under standard sea level conditions

V_{TS} [ft/s]	$U_{V_{TS}}$ [ft/s]
20	± 15.86
40	± 7.93
60	± 5.29
80	± 3.96
100	± 3.17
120	± 2.64
140	± 2.27
160	± 1.98

From the tabulated values, the uncertainty in the velocity at the higher speeds results in about 2% error. The error is much greater at the lower speeds, and should be considered when looking at how well the velocity measured by the sonic sensor compares with the velocity measured by more conventional methods.

A.2 Monte Carlo Analysis of Sonic Sensor

To determine the sensitivity of the sonic sensor to the geometric parameters, a Monte Carlo simulation is performed with the analytic model described in Chapter 3 of this work. For the Monte Carlo simulation, the geometric parameters are varied randomly with a normal distribution between the assumed manufacturing tolerances outlined in Table A.2.

Table A.2: Monte Carlo Geometric Uncertainty Parameters

Parameter	Uncertainty
R [in]	± 0.001
θ [deg]	± 0.1

This analysis assumes a broadband signal and the sampling rate is 2 Million samples per second. This will minimize the impact of the sampling rate on the estimated time delay of the signal and the broadband signal allows for no ambiguity in the peak of the cross-correlation. The SNR is assumed to be high enough for a good correlation at all speeds to minimize the effect of the decreasing SNR with speed. The geometric uncertainty is determined at 50 ft/s, 100 ft/s, 300 ft/s, 500 ft/s, and 800 ft/s through the Monte Carlo analysis for 1000 simulated cases, each. Figure A.1 shows the results of the Monte Carlo analysis for a simulated velocity of 300 ft/s. These results are representative for all cases, the results of which are outlined in Table A.3 for velocity and speed of sound, and Table A.4 for temperature and angle of attack for reference and comparison.

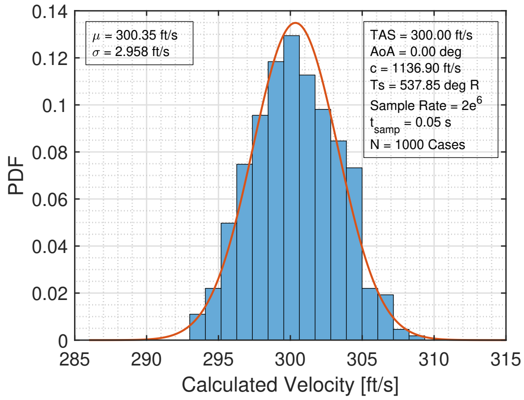

(a) Velocity PDF

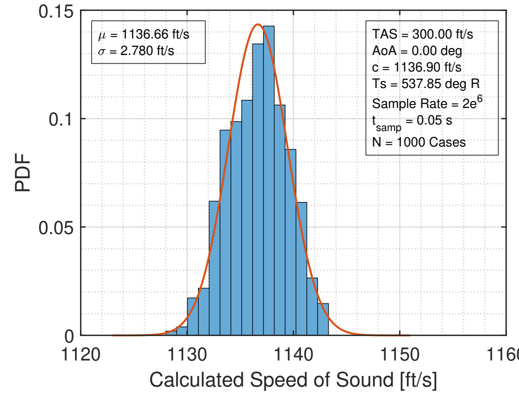

(b) Speed of Sound PDF

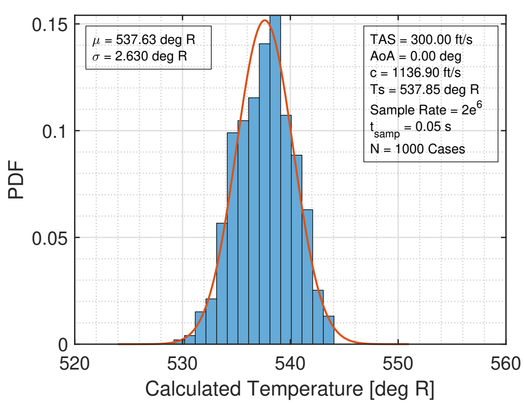

(c) Static Temperature PDF

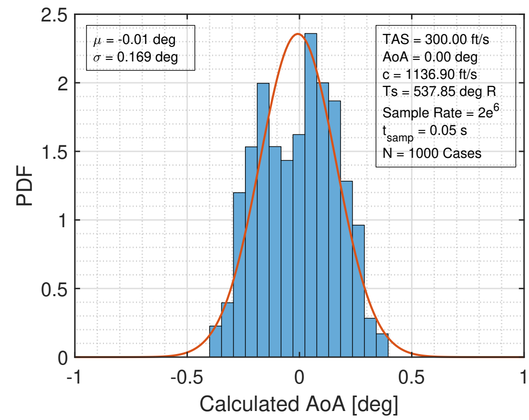

(d) Angle of Attack PDF

Figure A.1: Probability distribution functions for (a) Velocity (b) Speed of sound (c) Static temperature and (d) Angle of attack for 1000 Monte Carlo simulations of a 300 ft/s flow field sampled at two million samples per second with a 0.05 s sample bin for the cross correlation and an angle of attack of zero degrees

The results of the Monte Carlo runs show the trends match well the probability density function for all cases except for the angle of attack. The velocity has a mean value of 300.35 ft/s with a 95% confidence interval of ±5.92 ft/s. Similarly, the mean speed of sound for this analysis was 1,136.66 ft/s with a 95% confidence interval of ±5.56 ft/s. The velocity measurements are expected to have similar confidence intervals as they are dependent on one another. The confidence interval is a little on the high side because this assumes that the acoustic centers of the receivers are not calibrated to begin with and the geometric tolerances are purely from manufacturing.

The temperature has a mean value of 538.18 deg R and a 95% confidence interval of ±5.84 deg R. The angle of attack has a mean value of -0.01 deg with a 95% confidence interval of ±0.338 deg. The impact on changing the nominal angle of attack to five degrees is shown in Figure A.2.

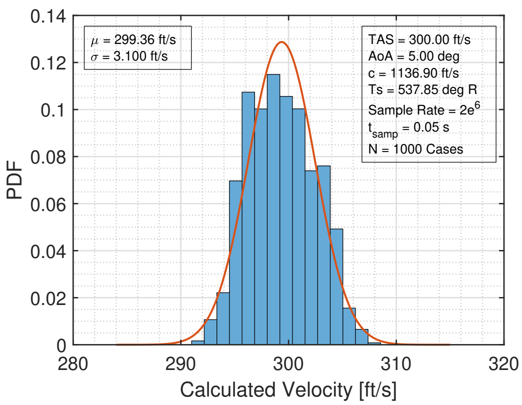

(a) Velocity PDF

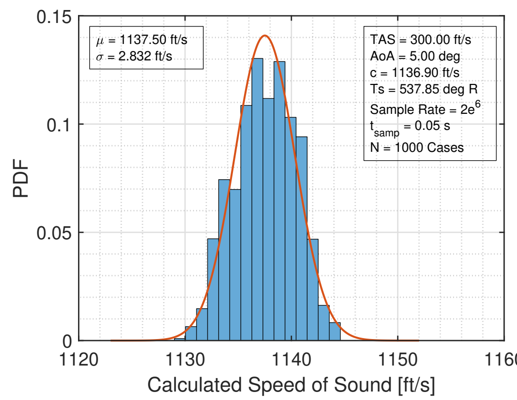

(b) Speed of Sound PDF

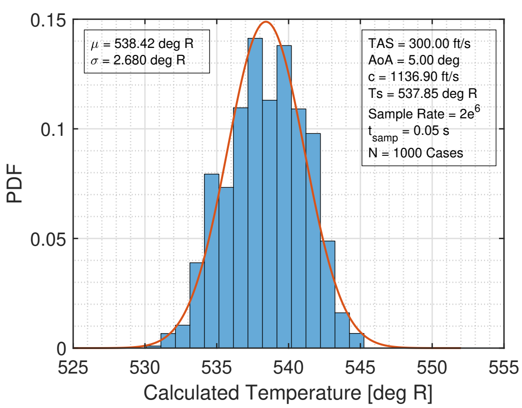

(c) Static Temperature PDF

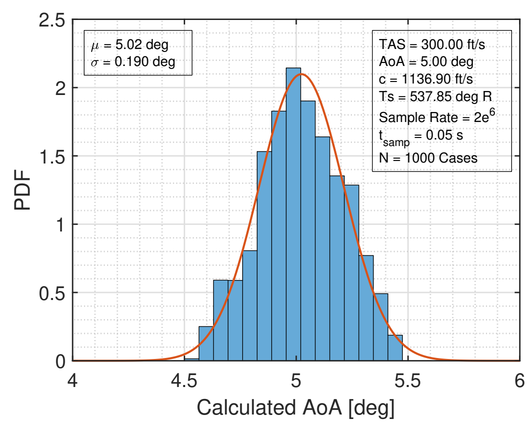

(d) Angle of Attack PDF

Figure A.2: Probability distribution functions for (a) Velocity (b) Speed of sound (c) Static temperature and (d) Angle of attack for 1000 Monte Carlo simulations of a 300 ft/s flow field sampled at two million samples per second with a 0.05 s sample bin for the cross correlation and an angle of attack of five degrees

The velocity has a mean value of 299.36 ft/s with a 95% confidence interval of ±5.35 ft/s. Similarly, the mean speed of sound for this analysis was 1,137.50 ft/s with a 95% confidence interval of ±5.66 ft/s. The temperature has a mean value of 538.42 deg R and a 95% confidence interval of ±5.36 deg R. The angle of attack has a mean value of 5.02 deg with a 95% confidence interval of ±0.380 deg. Increasing the angle of attack to ten degrees, the probability density functions are shown in Figure A.3.

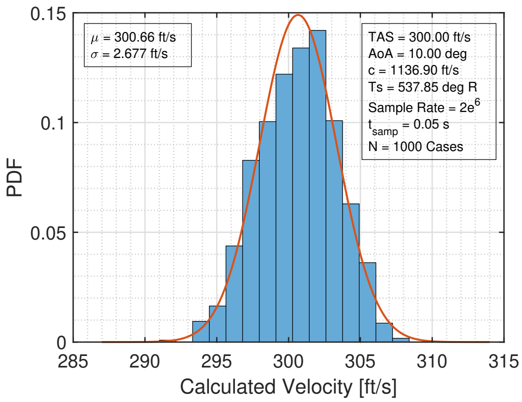

(a) Velocity PDF

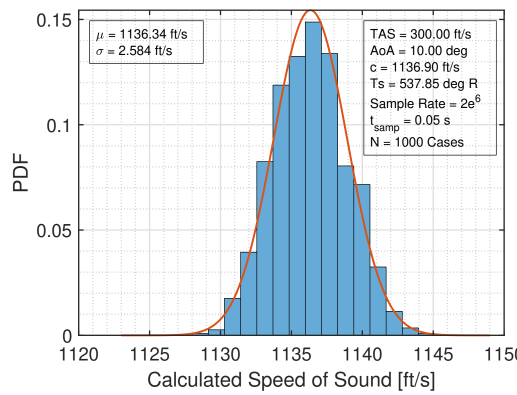

(b) Speed of Sound PDF

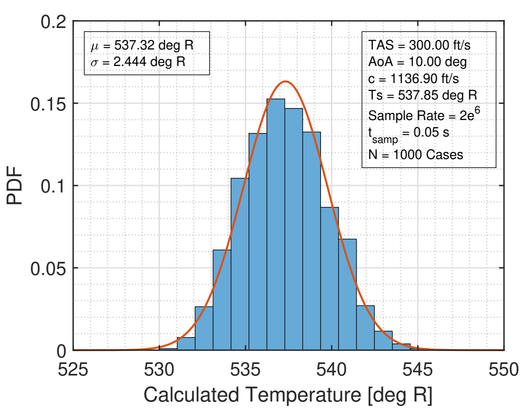

(c) Static Temperature PDF

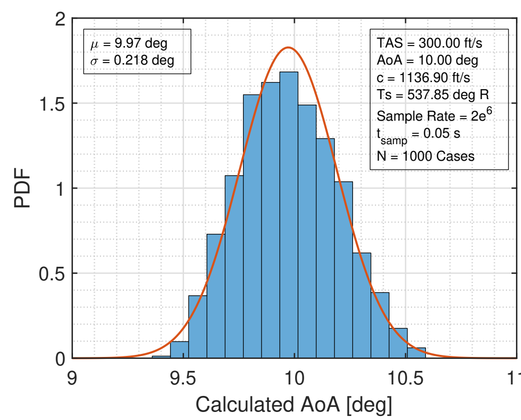

(d) Angle of Attack PDF

Figure A.3: Probability distribution functions for (a) Velocity (b) Speed of sound (c) Static temperature and (d) Angle of attack for 1000 Monte Carlo simulations of a 300 ft/s flow field sampled at two million samples per second with a 0.05 s sample bin for the cross correlation and an angle of attack of ten degrees

The velocity has a mean value of 300.66 ft/s with a 95% confidence interval of ±5.35 ft/s. Similarly, the mean speed of sound for this analysis was 1,136.34 ft/s with a 95% confidence interval of ±5.17 ft/s. The temperature has a mean value of 537.32 deg R and a 95% confidence interval of ±4.89 deg R. The angle of attack has a mean value of 9.97 deg with a 95% confidence interval of ±0.432 deg. As seen in Figure A.1 through Figure A.3, changing the angle of attack has a minimal impact on the 95%

confidence interval.

Table A.3: Mean and two-sigma parameters of the probability distribution functions for velocity and speed of sound

U [ft/s]	α [deg]	μ_U [ft/s]	$2\sigma_U$ [ft/s]	μ_c [ft/s]	$2\sigma_c$ [ft/s]
50	0.00	49.60	6.55	1,137.24	6.17
100	0.00	100.13	6.19	1,136.79	5.87
300	0.00	300.35	5.92	1,136.66	5.56
500	0.00	499.61	4.95	1,137.21	4.44
800	0.00	799.12	4.90	1,137.61	4.30
300	5.00	299.36	6.20	1,137.50	5.66
300	10.00	300.66	5.35	1,136.34	5.17

Table A.4: Mean and two-sigma parameters of the probability distribution functions for temperature and angle of attack

U [ft/s]	α [deg]	μ_{T_s} [deg R]	$2\sigma_{T_s}$ [deg R]	μ_α [deg]	$2\sigma_\alpha$ [deg]
50	0.00	538.18	5.84	0.03	1.550
100	0.00	537.75	5.56	-0.02	0.936
300	0.00	537.63	5.26	-0.01	0.338
500	0.00	538.14	4.21	0.02	0.164
800	0.00	538.52	4.08	0.01	0.116
300	5.00	538.42	5.36	5.02	0.380
300	10.00	537.32	4.89	9.97	0.432

Looking at the data in the tables, the 95% confidence interval reduces with speed, but it is a marginal effect. The mean value for the velocity and speed of sound are all within 0.5 ft/s of the nominal value, showing that the technique is fairly accurate with measuring the velocity and speed of sound provided there is ample SNR to extract the peak from the cross-correlation. The 95% confidence intervals are similar for speed of sound and velocity measurement as expected because they are derived from the same features and are linked in the derivation of the theory. The mean value of the angle of attack is at maximum 0.03 degrees away from the nominal value, and the confidence interval is less than a degree for most cases. All of the 95% confidence intervals decrease with speed showing that the sensor will increase in accuracy as the speed is increased. The 95% confidence intervals for the speed of sound and velocity are fairly high, but these are due to the tolerance of the geometric parameters. It was assumed that the tolerances are just based on manufacturing, and no calibration techniques to find the acoustic centers of the receivers. Incorporating a calibration procedure after the sensor is complete will reduce the 95% confidence intervals for the sensor and can be tailored to suit the needs of the end customer. The calibration process can be performed in static conditions, because all that needs to occur is that the manufacturing tolerances and the small changes in geometric positioning be accounted for in the calibration process. As a test case on the manufacturing tolerances, the uncertainty in the location of the receivers is defined in Table A.5.

Table A.5: Monte Carlo reduced geometric uncertainty tolerances

Parameter	Uncertainty
R [in]	± 0.0001
θ [deg]	± 0.01

The same Monte Carlo analysis is performed just for a 300 ft/s case at zero angle of attack to determine the changes in the uncertainty of the solution. The impact of the decrease in uncertainty shows the importance of knowing the geometry with a high degree of accuracy. Using the static conditions of the sonic sensor will increase the accuracy of the geometry definition, and effectively increase accuracy of the measured results. The uncertainty in the calculated characteristics reduces by 10 times with a reduction in the tolerance of the geometry.

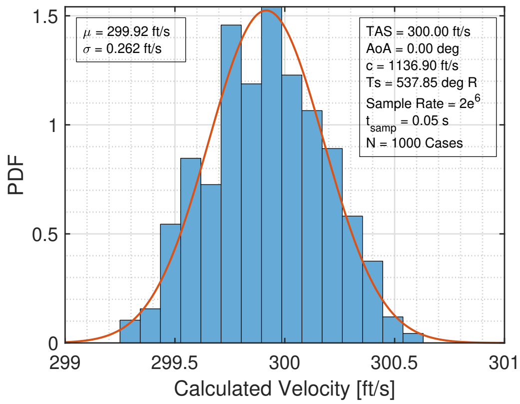

(a) Velocity PDF

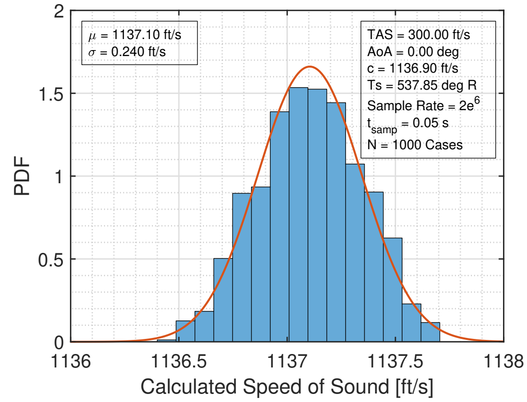

(b) Speed of Sound PDF

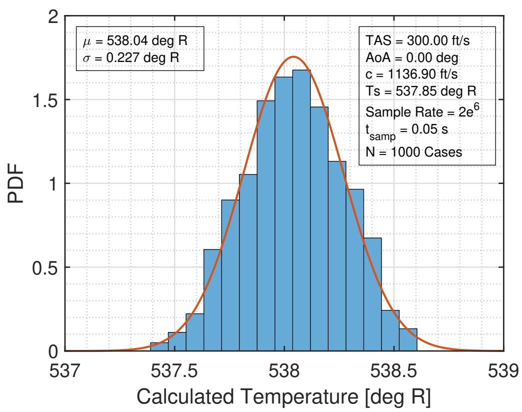

(c) Static Temperature PDF

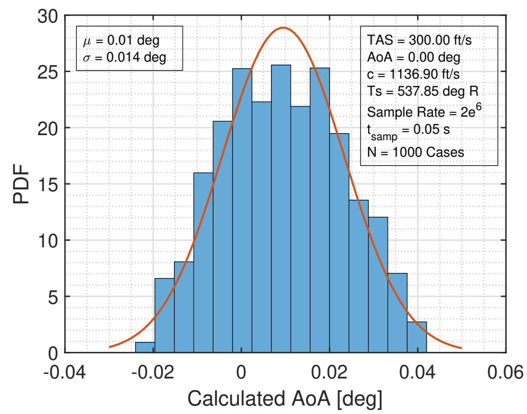

(d) Angle of Attack PDF

Figure A.4: Probability distribution functions for (a) Velocity (b) Speed of sound (c) Static temperature and (d) Angle of attack for 1000 Monte Carlo simulations of a 300 ft/s flow field sampled at two million samples per second with a 0.05 s sample bin for the cross correlation and an angle of attack of zero degrees and a reduced geometric uncertainty

The results of the Monte Carlo runs show the trends match well the probability density function for all cases except for the angle of attack. The velocity has a mean value of 299.92 ft/s with a 95% confidence interval of ±0.52 ft/s. Similarly, the mean speed of sound for this analysis was 1,137.1 ft/s with a 95% confidence interval of ±0.48 ft/s. The velocity measurements are expected to have similar confidence intervals as they are dependent on one another. The confidence interval is a little on the high side because this assumes that the acoustic centers of the receivers are not calibrated to begin with and the geometric tolerances are purely from manufacturing. The temperature has a mean value of 538.04 deg R and a 95% confidence interval of ± 0.45 deg R.

REFERENCES

[1] J. D. Anderson, *Introduction to Flight*. New York, New York: McGraw-Hill, 2005.

[2] P. Jarvinen, “Detection of pitot-static icing at high altitudes,” *51st AIAA Aerospace Sciences meeting including the New Horizons Forum and Aerospace Exposition*, 2013.

[3] M. Beck and A. Plaskowski, *Cross Correlation Flowmeters-Their Design and Application*. Bristol, England: Adam Hilger, 1987.

[4] G. Goglia and J. Shen, “Experimental and analytical studies of a true airspeed sensor,” National Aeronautics and Space Administration, Contractor Report CR-165704, 1983.

[5] Anon., “A general technical bulletin on total temperature sensors,” Rosemount Engineering Company, Bulletin 7637, 1963.

[6] A. Franz, “Pressure and temperature measurement in supercharger investigations,” NACA, Technical Memorandum 953, 1938.

[7] Anon., “Total temperature sensors,” Goodrich, Technical Report 5755, 1994.

[8] L. L. Vie, “Review of research on angle-of-attack indicator effectiveness,” National Aeronautics and Space Administration, Technical Memorandum TM-2014-218514, 2014.

[9] *Aerosonic corporation*, `https://www.aerosonic.com`, Accessed: 2017-01-04.

[10] D. Rogers, “Investigation of a general aviation differential pressure angle of attack probe,” *Journal of Aircraft*, vol. 50, no. 5, pp. 1668–1671, 2013.

[11] W. Gracey, “Summary of methods of measuring angle of attack on aircraft,” NACA, Technical Note TN-4351, 1958.

[12] M. Jost, F. Schwegmann, and T. Kohler, “Flush air data system - an advanced air data system for the aerospace industry,” *AIAA Guidance, Navigation, and Control Conference and Exhibit*, 2004.

[13] F. A. P. Lie and D. Grebre-Egziabher, “Synthetic air data system,” *Journal of Aircraft*, vol. 50, no. 4, 2013.

[14] A. Smart, "Velocity sensor for an airborne optical air data system," *Journal of Aircraft*, vol. 28, no. 3, 1991.

[15] A. Yalin and R. Miles, "Temperature measurements by ultraviolet filtered rayleigh scattering using a mercury filter," *Journal of Thermophysics and Heat Transfer*, vol. 14, no. 2, 2000.

[16] D. Pope, D. Lawrence, and B. Argrow, "Optical flow techniques for wind-velocity sensing on a small unmanned aircraft system," *AIAA SciTech Forum*, 2015.

[17] N. Matayoshi, K. Asaka, and Y. Okumo, "Flight-test evaluation of a helicopter airborne lidar," *Journal of Aircraft*, vol. 44, no. 5, 2007.

[18] V. Suomi and E. Barrett, "Preliminary report on temperature measurement by sonic means," *Journal of Meteorology*, vol. 6, 1949.

[19] J. Kaimal and J. Businger, "A continuous wave sonic anemometer-thermometer," *Journal of Applied Meteorology*, vol. 2, 1963.

[20] R. Schotland, "The measurement of wind velocity by sonic means," *Journal of Meteorology*, vol. 12, 1955.

[21] J. Wyngaard, "Cup, propeller, vane, and sonic anemometers in turbulence research," *Annual Review of Fluid Mechanics*, vol. 13, 1981.

[22] M. Mizuma, K. Sahashi, and Y. Mitsuta, "A comparitive observation of sonic anemometer and traditional methods of vertical velocity measurement," Special Contributions of the Geophysical Institute, Kyoto University, Tech. Rep., 1967.

[23] J. Stichman, "A sonic velometer," *IEEE Transactions on Instrumentation and Measurement*, vol. IM-23, no. 3, 1974.

[24] J. Kaimal, "Sonic anemometer measurements of atmospheric turbulence," *Proceedings of the Dynamic Flow Conference*, 1978.

[25] J. Kaimal and J. Wyngaard, "The Kansas and Minnesota experiments," *Boundary-Layer Meteorology*, vol. 50, 1989.

[26] P. Coppin and K. Taylor, "A three component sonic anemometer/thermometer system for general micrometeorological research," *Boundary-Layer Meteorology*, vol. 527, 1983.

[27] N. Matayoshi, H. Inokuchi, K. Yazawa, and Y. Okuno, "Development of ultrasonic velocimeter and its application to helicopters," *AIAA Atmospheric Flight Mechanics Conference and Exhibit*, 2005.

[28] Anon., *Ultrasonic Anemometer Model 8100 Instruction Manual*. Traverse City, Michigan: R.M. Young Company, 2010.

[29] *Ft technologies*, `http://www.fttechnologies.com/Wind-Sensors`, Accessed: 2017-01-04.

[30] J. Kaimal and K. Gaynor, "Another look at sonic thermometry," *Boundary-Layer Meteorology*, vol. 56, 1990.

[31] O. Tekelioglu, "Pressure and temperature measurement in supercharger investigations," *40th AIAA Aerospace Sciences Meeting and Exhibit*, 2002.

[32] D. Delamore-Sutcliffe and D. Greenwell, "Application of ultrasound in wind tunnel testing," *24th Applied Aerodynamics Conference, San Francisco, CA*, 2006.

[33] R. Rodenhiser, W. Durgin, and H. Johari, "Ultrasonic method for aircraft wake vortex detection," *44th AIAA Aerospace Sciences Meeting and Exhibit, Reno, NV*, 2006.

[34] R. Otero, K. Lowe, and W. Ng, "Extension of sonic anemometry to high subsonic Mach number flows," *Measurement Science and Technology*, no. 28, 2017.

[35] K. Ahuja, H. Tanna, and B. Tester, "An experimental study of transmission, reflection, and scattering of sound in a free jet flight simulation facility and comparison with theory," *Journal of Sound and Vibration*, vol. 75, no. 1, 1981.

[36] K. Ahuja, B. Tester, and H. Tanna, "The free jet as a simulator of forward velocity effects on jet noise," National Aeronautic and Space Administration, Contractor Report CR-3056, 1978.

[37] J. Wyngaard and S. Zhang, "Transducer shadow effects on turbulence spectra measured by sonic anemometers," *Journal of Atmospheric and Oceanic Technology*, 1985.

[38] J. Kaimal, K. Gaynor, H. Zimmermann, and G. Zimmermann, "Minimizing flow distortion errors in a sonic anemometer," *Boundary-Layer Meteorology*, vol. 53, 1990.

[39] A. Grelle and A. Lindroth, "Flow distortion by solent sonic anemometer: Wind tunnel calibration and its assessment for flux measurements over forest and field," *Journal of Atmospheric and Oceanic Technology*, 1994.

[40] M. van der Molen, J. Gash, and J. Elbers, “Sonic anemometer (co)sine response and flux measurement ii: The effect of introducing an angle of attack dependent calibration,” *Agricultural and Forest Meteorology*, vol. 122, 2004.

[41] T. Nakai, M. van der Molen, J. Gash, and Y. Kodama, “Correction of sonic anemometer angle of attack errors,” *Agricultural and Forest Meteorology*, vol. 136, 2006.

[42] T. Nakai and K. Shimoyama, “Ultrasonic anemometer angle of attack errors under turbulent conditions,” *Agricultural and Forest Meteorology*, vol. 162-163, 2012.

[43] T. Horst, S. Semmer, and G. Maclean, “Correction of a non-orthogonal, three-component sonic anemometer for flow distortion by transducer shadowing,” *Boundary-Layer Meteorology*, vol. 155, 2015.

[44] X. Cheng, Z. Peng, F. Hu, Q. Zeng, W. Luo, Y. Zhao, and Z. Hong, “Measurement errors and correction of the UAT-2 ultrasonic anemometer,” *Science China Technological Sciences*, vol. 58, 2015.

[45] H. Siebert and A. Muschinski, “Relevance of a tuning fork effect for temperature measurements with the gill solent hs ultrasonic anemometer-thermometer,” *Journal of Atmospheric and Oceanic Technology*, 2001.

[46] C. Espinoza, J. Villanueva, and S. Catunda, “Wind speed measurement and uncertainty analysis using ultrasonic sensors with Kalman filtering,” Institute of Electrical and Electronics Engineers, Tech. Rep., 2010.

[47] N. Ingaroca, J. Villanueva, R. Freire, and S. Catunda, “Wind speed measurement method using ultrasonic sensors with stationary wavelet transform,” Institute of Electrical and Electronics Engineers, Tech. Rep., 2012.

[48] J. Villanueva, S. Catunda, and R. Tanschiet, “Data fusion methods based on fuzzy theory for wind speed measurement using ultrasonic transducers,” *IEEE International Instrumentation and Measurement Technology Conference*, 2008.

[49] C. Friehe, “Effects of sound speed fluctuations on sonic anemometer measurements,” Journal of Applied Meteorology, Tech. Rep., 1976.

[50] D. Cruette, A. Marillier, J. Dufrense, and J. Grandpeix, “Fast temperature and true airspeed measurements with the airborne ultrasonic anemometer-thermometer (AUSAT),” *Journal of Atmospheric and Oceanic Technology*, 2000.

[51] H. Maeda and Y. Umeda, “An ultrasonic altitude-velocity sensor for airplanes in the vicinity of the ground,” *Journal of Aircraft*, vol. 9, no. 4, 1972.

[52] R. Loschke, J. Revell, F. Balena, and F. Hickmon, “Air data system for measuring fluid flow and direction,” pat. 5 585 557, 1996.

[53] J. Sly and J. Boelman, “Determining aircraft flying conditions based on acoustic signals caused by airflow,” pat. 11 016 114, 2021.

[54] K. Yazawa, T. Tamaru, and H. Hashiguchi, “Development of ultrasonic anemometer for environmental observation by aircraft,” *1st AIAA Aircraft, Technology, Integration, and Operations Forum*, 2001.

[55] O. Castillo and E. Londner, “UAV flight testing with an airborne sonic anemometer, IMU, and GPS,” *28th AIAA Applied Aerodynamics Conference*, 2010.

[56] P. Hart, *Aviation Electronics Europe - Munich 26th March 2015 Situational Awareness – latest and future challenges Low Air Speed Data*. Curtiss-Wright Defense Solutions Division, 2015.

[57] M. Salikuddin and K. Ahuja, “A device to generate high frequency noise from commercially available low frequency acoustic drivers,” *Journal of Sound and Vibration*, vol. 123, no. 2, 1988.

[58] A. Marco, T. Corkett, and B. W. Drinkwater, “Ultraino: An open phased-array system for narrowband airborne ultrasound transmission,” *IEEE Transactions on Ultrasonics, Ferroelectrics, and Frequency Control*, vol. 65, no. 1, 2018.

[59] J. Bendat and A. Piersol, *Random Data Analysis and Measurement Procedures*, 4th. Hoboken, New Jersey: John Wiley and Sons, Inc., 2010.

[60] J. Hassab and R. Boucher, “Optimum estimation of time delay by a generalized correlator,” *IEEE Transactions on Acoustics, Speech, and Signal Processing*, vol. ASSP-27, no. 4, 1979.

[61] J. Hassab and R. Boucher, “An experimental comparison of optimum and sub-optimum filters’ effectiveness in the generalized correlator,” *Journal of Sound and Vibration*, vol. 76, no. 1, 1981.

[62] C. Knap and C. Carter, “The generalized correlation method of estimation of time delay,” *IEEE Transactions on Acoustics, Speech, and Signal Processing*, vol. ASSP-24, no. 4, 1976.

[63] Y. Zhang and W. Abdulla, “A comparitive study of time-delay estimation techniques using microphone arrays,” The University of Auckland, School of Engineering Report 619, 2005.

[64] J. Li, W. Liu, N. Chen, and G. Fan, "A robust and higher precision time delay estimation method facing low signal to noise ration conditions," *International Journal of Intelligent Information Systems*, vol. 7, no. 3, 2018.

[65] MATLAB, *version 9.0.0.341360 (R2016a)*. Natick, Massachusetts: The MathWorks Inc., 2016.

[66] K. K. Ahuja, "Laboratory simulation of point monopole and point dipole sound sources," *2nd International Congress on Recent Developments in Air- and Structure-Borne Sound and Vibration*, 1992.

[67] D. Bohn, "Environmental impacts on the speed of sound," *Journal of Audio Engineering Society*, vol. 36, no. 4, 1988.

[68] M. Adaramola, O. Akinlade, D. Sumner, D. Bergstrom, and A. Schenstead, "Turbulent wake of a finite circular cylinder of small aspect ratio," *Journal of Fluids and Structures*, vol. 22, 2006.

[69] O. Frederich, J. Scouten, D. Luchtenburg, and F. Theile, "Large-scale dynamics in the flow around a finite cylinder with a ground plate," *Fluid Dynamics Research*, vol. 43, 2010.

[70] H. O'Neil, "Theory of focusing radiators," *The Journal of the Acoustical Society of America*, vol. 21, no. 516, 1949.

[71] ANSYS FLUENT, Help System, version 17.1.

[72] Singh, "Investigation of reattachment length for a turbulent flow over a backward facing step for different step angle," *International Journal of Engineering, Science and Technology*, vol. 3, no. 2, 2011.

[73] Schelt, "Direct numerical simulation of the flow over a forward facing step - flow structure adn aeroacoustic source regions," *International Journal of Heat and Fluid Flow*, vol. 43, 2013.

[74] L. Houegnigan, P. Safari, C. Nadeu, M. van der Schaar, M. Sole, and M. Andre, "Neural networks for high performance time-delay estimation and acoustic source localization," *Computer Science and Information Technology*, vol. 7, no. 1, 2017.

[75] S. Shaltaf, "Neural-network-based time-delay estimation," *Journal on Applied Signal Processing*, vol. 3, 2004.

[76] J. D. Anderson, *High Temperature Gas Dynamics*, 2nd. Reston, Virginia: American Institute of Aeronautics and Astronautics, 2006.

VITA

Jonathan D. Carroll

PhD Student in Aerospace Engineering

School of Aerospace Engineering

Georgia Institute of Technology

Atlanta, Georgia, The United States of America

Education

Georgia Institute of Technology, Atlanta, Georgia

Ph.D. Student, Aerospace Engineering, 2016 to 2021 (expc.)

University of Kansas, Lawrence, Kansas

M.S., Aerospace Engineering, 2015

B.S., Aerospace Engineering, 2010

Academic Employment

Georgia Institute of Technology, Atlanta, GA

Graduate Research Assistant, 2015 - 2019

University of Kansas, Lawrence, KS

Lab Assistant, 2008 - 2010

Publications

D.M. van Dommelen, J.D. Carroll, W.A. Anemaat, ”Semi-Empirical Propeller Power Effects in Airplane Preliminary Design”, presented at the 7th Asia-Pacific International Symposium on Aerospace Technology (APISAT), Queensland, Australia, November 26, 2015.

A. Rizzi, P. Meng, Royal Institute of Technology, Sweden; B. Nagel, D. Boehnke, German Aerospace Center (DLR), Germany; W.A.J. Anemaat, J. Carroll, Design, Analysis and Research Corporation (DARcorporation), USA, ”Collaborative Aircraft Design using AAA and CEASIOM linked by CPACS Namespace”, presented at CAES European Air & Space Conference 2013, Linkoping, Sweden, September 16-19, 2013.

W.A. Anemaat, B. Kaushik, J. Carroll, J. Jeffery, ”Software Tool Development to Improve the Airplane Preliminary Design Process”, ISPE paper 33.00, presented at the 20th ISPE International Conference on Concurrent Engineering at RMIT, Melbourne, Australia, September 2-6, 2013.

R. Oliver, W.A. Anemaat, B. Kaushik, J. Carroll, B. McCormick, ”The Hexplane: A scalable Air Vehicle Concept for Breakthrough Performance in Speed and VTOL”, AIAA-2013-1089, presented at the 51st AIAA Aerospace Sciences Meeting, January 7-10, 2013, Grapevine, Texas.